Title	Development of Control and Operational Strategies for Wind Power Based Microgrid with Integrated Energy Storage(Dissertation_全文)
Author(s)	Netra Prasad Gyawali
Citation	Kyoto University (京都大学)
Issue Date	2011-03-23
URL	http://dx.doi.org/10.14989/doctor.k16087
Right	
Type	Thesis or Dissertation
Textversion	author

Development of Control and Operational Strategies for Wind Power Based Microgrid with Integrated Energy Storage

Netra Prasad Gyawali

2011

Development of Control and Operational Strategies for Wind Power Based Microgrid with Integrated Energy Storage

A Dissertation Submitted to the
Graduate School of Engineering, Kyoto University
in Candidacy for the Degree of Doctor of Philosophy

Netra Prasad Gyawali

2011

Abstract

Wind power has emerged as the most dynamically growing energy source all over the world. There is significant advancement in its technologies with increase in size and power capture capacity, enabling it cost competitive to conventional power plants. With increased penetration of wind power into the grid, the industries and the utilities are confronting with many challenges, such as frequency regulation, power fluctuation, voltage/reactive power control and sporadic tripping of the upstream power network. Wind power is further insufficient in islanded operation, where the frequency and voltage regulations are the main issues beside the load-following problem. Scrutiny of these challenges reveals that their root cause is the intermittent power output, owing to its dependability on varying wind speed. In order to cope with the unpredictability of the generation, the best solution, despite its high cost, is to deploy electrical energy storage units. Such storage units can be employed to many applications, such as long-term storage for energy management, mid-term storage for frequency regulation and peak shaving, and short-term/buffer applications for instantaneous power balance.

Choice of the particular storage type is guided by a number of factors and specific to the application. In the case of power system where the penetration level of renewable sources is considerable or when the renewable based power system needs to be operated in an islanded mode, a combination of short and long-term storage is desired for reliable operation. These storage units can be configured in diverse ways, often requiring power electronic converters to connect with the regulated dc or ac bus. In the case of variable speed wind turbine generator systems, there is indispensable use of ac-dc-ac converters, so the storage devices can be connected to the intermediate dc bus via dc-dc converters. This dissertation proposes a dedicated storage mix embedded at the intermediate dc bus of a doubly-fed induction generator, which provides the functionalities of short-term power management and long-term energy management. The storage mix consists of a fuel cell/electrolyzer (FC/ELZ) pair and an ultracapacitor (UC) as the primary power source and the secondary power source, respectively; in which the FC/ELZ pair is accommodated as a single unit by a common dc-dc converter. To accomplish the objective of transient and long-term power management, the control schemes associated with different converters are proposed. The control scheme applied to the line-side converter enables the wind power and storage system (WPSS) to operate in the islanded mode or the dispatchable grid-connected mode, by drawing compensating quota of power from the storage system. The controller associated with energy storage system employs the UC to balance the transient part by consuming the transient fluctuation, while the steady-state imbalance is compensated by operating in the FC or ELZ mode. The salient point of the scheme is that a unified control scheme is used with each controller to operate in one's respective modes in a smooth manner. Further, an improved power sharing scheme is also introduced in the case when there are more than one controllable power sources.

In order to investigate the performance, the system configuration is investigated and the control scheme has been designed with linearized models of various subsystems. Based on the dynamic component models, a simulation model for the proposed hybrid power system has been developed in MATLAB/Simulink environment. The overall operation strategy for coordinating the power flows among the different energy sources has been presented in detail. Simulation studies have been carried out to verify the system performance under different operating scenarios. The results show that the overall power management strategy is effective and the power flow among the different energy sources and the load demand are balanced successfully.

Contents

List of Figures

Acknowledgements

This thesis is dedicated to my parent whose constant support, encouragement, and love, are always with me in whatever I pursue.

First and foremost, I would like to express profound gratitude to my supervisor, prof. Ohsawa, for his invaluable support, supervision and useful suggestions throughout this research work. His encouragement and continuous guidance, not limited only to the research, but also enabled me to complete my work successfully. As my teacher and mentor, he has taught me more than I could ever give him credit for here. I am very thankful with Dr. Yamamoto for his continuous support, comment and any kind of assistance in the time whenever I needed.

My sincere gratitude goes to prof. Hikihara and prof. Hagiwara for their invaluable comments and suggestions on my research work as the co-supervisors. Special thank goes to Dr. Zhou for his supportive and helping hand in all areas since the day I came in Japan. He was always ready to answer all kinds of questions, and provided meaningful advices in spite of his busy time schedule.

I am thankful to all the members in the Ohsawa lab and my friends, who provided immense help directly and indirectly all the time.

Last but not the least, I wish to thank my loving and supportive wife who provided the endless support and care which are too numerous to mention. The acknowledgement will, perhaps, be incomplete without remembering my wonderful children, Sambodhi and Snidh, whose smiling faces always inspire me to dedicate at my work in all situations.

Chapter 1 Introduction

1.1 Background

Rising environmental concerns, increasing fossil fuel depleting rates, and the recent advent of power electronics technologies, are favoring the deployment of renewable type modular generators, also called distributed generation (DG) units, around the world. In rural and remote areas, the DG sources have drawn further attention for the stand-alone operation due to the high cost and complexity of the transmission network [1]. Among the renewable energy resources, wind power has emerged as the most dynamically growing energy source. There is significant advancement in its technologies with increase in size and power capture capacity, making the wind power cost competitive to conventional power plants. Worldwide nameplate capacity of wind powered generators was 157.9 GW at the end of 2009, with 90% installation between 2000 and 2009 only [2]. Most of the countries have put great emphasis on wind power installation and it is likely that this trend will continue in coming decades.

Generating electricity from wind takes place in two steps. Firstly, the aerodynamic energy in the wind passes over the blades exerting a turning force. The rotating blades, then, turn a shaft inside the nacelle, which goes into a gearbox. The gearbox increases the rotation speed for the generator. Consequently, the generator converts the rotational energy into the electrical energy with the help of applied magnetic fields. The blades on the wind turbines may be rotated in two axes – horizontal or vertical axis. Horizontal axis wind turbines are the more familiar windmill type where the blades (normally three) are bolted into a hub on its tower and rotated in a vertical plane about a horizontal axis facing to the wind. In contrast, vertical axis turbines rotate around the respective vertical axis and do not need a particular orientation toward the wind. An advantage of vertical axis turbines is that the generator and the gearbox can be placed on the ground, so a high tower is not required to mount the machine. Further, a yaw mechanism is not needed to turn the rotor against the wind. However, at the ground level, the wind speed is low and it contains high turbulence, so it is desired to install wind blades at a height to get better wind capture. This is achieved by using the horizontal axis turbine with its more efficient propellers. Therefore, most of the modern wind turbines are designed as the horizontal axis type.

Wind power is seldom operated in an islanded or a stand-alone mode, because the wind power output is uncontrolled, unlike the conventional power generator systems. So, it makes impossible to supply power to the unpredictable load from the uncontrolled source. The conventional approach is, therefore, to connect wind power generators with the utility grid and supply power as a "negative load". Direct connection of wind turbines (WTs) to the external ac point of common coupling, so called fixed speed wind turbine, is simple. The simplicity is, however, in the expense of efficient and flexible operation. Usually, there are mismatches in frequency and voltage between the wind turbine generator system (WTGS) and the common coupling point, which necessitates some sorts of power electronic converters for flexible functionalities. Consequently, the WTGS can be operated in a wide range of rotor speed as their name, variable-speed wind turbines. Compared to the fixed-speed operation, the variable-speed wind turbine provides 20–30% higher energy output, lower mechanical stress, and reduction in acoustic noise. Further, it also provides flexibility to control active and reactive power by utilizing full or partial rated power electronic conversion technology [3, 4]. Most of the major wind turbine manufactures are developing larger wind turbines in the range of 3 to 5 MW range, based on the variable-speed operation and the pitch control using a direct driven synchronous generator (without gearbox) or a doubly-fed induction generator (DFIG) [5]. The use of power electronic converters in the variable-speed wind turbine not only provides the flexible functionality and efficient operation, but also avails the intermediate dc bus for embedding energy storage devices. This, in turn, helps improving the power quality, system stability, better low voltage ride through capability, among the others [3, 6].

1.2 Wind Power Issues and Energy Storage

The transition from fossil fuel based power generation to power generation based on renewable energy resources (such as wind power) introduces challenging demands on the operation of electricity systems. At low penetration, wind turbines are not expected to take part in voltage and frequency control. If a disturbance occurs, the wind turbines are disconnected, and reconnected when normal operation has been resumed. With the high penetration into the power system, the wind power is, no longer, assumed as the "negative load"; meaning that uncontrollable power is injected to the system, unlike the "load" that consumes uncontrollable power from the system [7]. The wind energy source must interact with the rest of the power generation units in a system to make it possible for the system to secure a balance between supply and demand. With increased penetration of wind power into the grid, the industries and the utilities are confronting with many challenges, such as frequency regulation, power fluctuation, voltage/reactive power control and sporadic tripping of the upstream power network. Wind power is further insufficient in the islanded operation, where the frequency and voltage regulation are the main issues beside the load-following [8]. Scrutiny of these challenges reveals that their root cause is the intermittent power output, owing to its dependability on varying wind speed. In order to cope with the unpredictability of the generation, the best solution, despite its high cost, is to deploy electrical energy storage units. Such storage units can be employed to many applications: long-term storage for energy management, mid-term storage for frequency regulation and peak shaving, and short-term/buffer applications for instantaneous power balance [6].

Table A.1 in the appendix illustrates a comparative analysis of the different energy storage systems applicable to the wind power system. For the short-term energy storage, viable technologies include the flywheel energy storage, battery energy storage systems, ultracapacitors (UC), and the superconducting magnetic energy storage (SMES). For long-term energy management, the high capacity technologies include hydrogen storage [9], the redox flow batteries and the compressed air technology [10]. These storage units are either configured as one aggregated unit that serves for the whole wind farm, or the distributed one connected to each wind turbine generator system. Since no single energy storage is perfect, the choice among the different types is an open issue guided by the cost and technical trade off among the others. Irrespective of the type of storage systems, it is advisable to integrate local distributed generators, load and storage devices, making an autonomous local power network (LPN) to exploit most effective functionalities of hybrid power system.

1.3 Microgrid

One way of the efficient control, operation and management of hybrid distributed energy resources is to form an autonomous power network or a microgrid. The microgrid may be defined as a cluster of small generating sources, energy storage units and loads (heat and electricity), which can be operated in parallel with the utility grid or in an intentional island mode to provide a customized level of high reliability and resilience to grid disturbances [1]. An essential element of a microgrid is the capability to control the balance of the generating capacity and demand within the confines of the microgrid itself. Regardless the microgrid being connected to the utility grid or operating independently in a islanded mode, this control is essential to ensure the stable supply of energy to the consumers. With proper operation and management scheme, the microgrid appears as a dispatchable load or a generator from the utility side, so it behaves as a "good citizen" [11]. From the consumer perspective, it not only provides the improved reliability of electricity supply (as it can also supply electricity during the failure of the upstream network), but also opens the opportunity to sell the energy back to the utility from their generators in more flexible manner. By combining the renewable power sources with storage devices, consumers can respond to the price of electricity by participating in demand response. Further, the consumers can also integrate the functionality of heat and electricity, thereby enabling to use the combined heat and power with the onsite generators, like fuel cells and micro-turbines.

To achieve desired objectives from a hybrid local power network, the individual components should be configured properly with clearly defined control and operational laws. Unfortunately, there is no predefined topology and control scheme due to diverse nature of distributed energy resources (DERs). The renewable based local power network or microgrid has, thus two open issues; how to design the suitable topology for interconnecting the individual components? What sort of control strategies (e.g. hierarchical, coordinated or both) are necessary for the system, so that the subsystems would fit to fulfill the overall operational objective? In the view point of future "smarter" power network, where the contribution of wind power will be significant, the energy storage system is emerging as an indispensable unit for a microgrid. Being an important subset of the advanced future power network, research work on the microgrid has great potential to investigate the components' behaviors and fit them into a system [12].

1.4 Literature Review

Research on wind energy conversion is fairly mature and can be found in various studies. Conceptual design of a wind energy conversion system is presented in [3, 13]. Modeling, control and simulation of the wind turbine generator system are illustrated in [14-16]. These studies have detailed discussion on overall wind turbine generator system with their embedded power electronic conversion configurations. Due to the varying nature of wind power input, a backup storage unit is needed to reduce the wind power fluctuations and ensure the power balance. The topology of such hybrid power systems, in which the wind power is assisted by secondary backup systems, has been reported in many studies. Wind and diesel combination has been used in stand-alone network since the long time [17]. However, every diesel generator has several major disadvantages, such as low flexibility to respond the demand changes, high pollution and noise, and low efficiency, thereby making them less attractive for integrating with clean power generation systems. In the variable-speed wind turbine, there is indispensable use of ac-dc-ac type power electronic converters. The ac-dc-ac converters can be used for multipurpose, in which the intermediate dc-link bus helps augmenting various types of storage devices that require dc interconnection. Owing to its mature and cost effective solution, the battery system has been extensively used with wind power for various purposes, such as battery charging [18], suppressing the power fluctuation [19], and power management [20]. However, its size, limited charging/discharging cycles and the disposal issues are the constraints for wide scale application [21]. Other advance battery technologies like NiMH, NiCd and Li battery are superior in terms of efficiency, compactness and higher charging/discharging cycles, and mostly recommended for low voltage portable and vehicular applications [22].

Introduction of a short-term energy storage device in the intermediate dc-link bus is found in various studies. Embedding a flywheel energy system in [23], [24], SMES system in [25, 26] and ultracapacitor in [27], [28] are some examples to smooth the wind power fluctuation. For long-term energy balance, the pump hydro is a matured technology. However, its application is restricted by the geographical constraints and water availability. A fuel-cell (FC) and an electrolyzer (ELZ) pair is emerging as a candidate for the long-term power management utilizing pollution-free H_2 production and consumption technologies [29]. The multitude of studies has adopted the storage application either for the transient power fluctuation management, or the long-term energy management. There is very limited research exposure in the area of storage mix combining the short and long-term storage for the application of a wider time frame. When renewable resources become dominant in power generation, the short and long-term storage devices are complementary for a reliable operation in the islanded or dispatchable grid-connected mode. Integration of such mix unit into wind turbine generator system is relatively a new topic and the database of these studies is limited. In the distributed power system application, the ultracapacitor is a favorable candidate for the transient mitigation in terms of its speed, efficiency and cost [10], thus a combination of ultracapacitor and fuel cell/electrolyzer offers a promising technical solution for the short to long-term power management [30]. A few works are reported in this field [30, 31], however, they do not depict the clear picture on the power and energy balance among the energy resources having different time constants.

1.5 Proposed Study

The aim of this research work is to address short and long-term power management requirements of the wind power based microgrid by embedding an energy storage system. The storage system, termed as the dedicated energy storage system (DESS), consists of a fuel cell/ electrolyzer and an ultracapacitor as the primary and secondary power source, respectively. We propose a new configuration of DESS, in which the fuel cell and electrolyzer are accommodated as a single unit, by a common converter and control action. To accomplish the objective of transient and long-term power management, the control schemes associated with the line-side converter and DESS are developed. The control scheme applied to the line-side converter enables the wind power/storage system to operate in either an islanded or a dispatchable grid-connected mode, by drawing the compensating power from the DESS. The DESS employs the ultracapacitor to smooth the transient fluctuation, while the steady-state imbalance is compensated by operating in either the fuel cell or electrolyzer mode. The salient feature of the controllers is that a unified control scheme is used by each controller to operate in one's respective modes in a seamless manner. Further, an improved power sharing scheme among the multiple inverters is also proposed for the autonomous local power network having a high resistance-inductance ratio (*R*/*X*).

The rest of the thesis proceeds as follows. Beginning with the synoptic view of the wind power/storage and the related power electronic conversion system, chapter two presents the layout and unit sizing of the proposed system. Chapter three discusses on the dynamic modeling of system components. Chapter four presents the detailed design of the control and operational schemes of the overall wind power and the storage system followed by the discussion of simulation results in chapter five. In chapter six, the power sharing scheme among the inverters in an autonomous microgrid is investigated, and chapter seven gives the conclusion and prospective direction of the research work.

1.6 List of Publications

Some of the results presented in this thesis have been published in the following publications.

International Journal Papers

1. Netra Gyawali and Yasuharu Ohsawa, "Improved power sharing scheme for a microgrid with multiple distributed generators," *IEEJ Trans. EIS*, vol. 128(11), pp.1635-1640, 2008.
2. Netra Gyawali and Yasuharu Ohsawa, "Integrating fuel cell /electrolyzer/ultracapacitor system into a stand-alone micro-hydro plant," *IEEE Trans. on Energy Conversion System*, vol. 25(4), pp. 1092-1101, Dec. 2010.
3. Netra Gyawali, Osamu Yamamoto and Yasuharu Ohsawa, "Power dispatching from cage induction generator based wind power system with integrated smart energy storage," *IEEJ Trans. on Electrical and Electronics Engineering*, vol. 6(2), pp. 134–143, Mar. 2011.
4. Netra Gyawali, Osamu Yamamoto and Yasuharu Ohsawa, "Power management of DFIG based wind power system with integrated smart energy storage having SMES /fuel-cell/electrolyzer," *IET Journal of Renewable Energy* (under review).

International Conference Papers

1. Netra Gyawali and Yasuharu Ohsawa, "Power management schemes for a microgrid with inverter interfaced distributed generators," International conference of power system CPRI-IEEE/PES Bangalore, Dec. 2007.
2. Netra Gyawali and Yasuharu Ohsawa, "Effective voltage and frequency regulation strategy for a stand-alone system with induction generator/fuel cell /ultracapacitor," International conference on Integration of Wide-Scale Renewable Resources into the Power Delivery System, Cigre/IEEE Power Society, Calgary, Jul. 2009.
3. Netra Gyawali, Osamu Yamamoto and Yasuharu Ohsawa, "Dispatchable power from DFIG based wind-power system with integrated energy storage," IEEE/PES General Meeting Minnesota, Jul. 2010.

References

[1] Abu-Sharkh, S. , R. Yao, K. Steemers, J. Kohler, R. Arnold, A . Wilson, B. Li, T. Markvart, and N. Ross, "Microgrids: Distributed on-site generation," Tyndall research centre technical report, University of Southampton, 2005.

[2] World wind energy association, Annual report, March 2009, available online: http://www.wwindea.org/home/index.php.

[3] T. Ackermann, *Wind power in power systems*, John Wiley and Sons Ltd, 2006.

[4] T. Burton, D. Sharpe, N. Jenkins and E. Bossanyi, *Wind Energy Handbook,* John Wiley and Sons Ltd, 2004.

[5] T. Ackermann and L. Söder, "An overview of wind energy-status 2002," *Renewable and Sustainable Energy Reviews,* vol. 6(1-2), pp. 67-127, 2002.

[6] C. Abbey and G. Joos, "Energy storage and management in wind turbine generator systems," Proceeding of 12th international Power Electronics and Motion Control Conference, pp. 2051-2056, 2006.

[7] E. DeMeo, W. Grant, M. Milligan and M. Schuerger, "Wind plant integration," *Power and Energy Magazine, IEEE,* vol. 3, pp. 38-46, 2005.

[8] H. Holttinen, P. Meibom, A. Orths, F. Van Hulle, C. Ensslin, L. Hofmann, J. McCann, J. Pierik, J. O. Tande, A. Estanqueiro, L. Söder, G. Strbac, B. Parsons, J. C. Smith and B. Lemström, "Design and operation of power systems with large amounts of wind Power, first results of IEA collaboration," Global Wind Power Conference, Australia, Sep. 2006.

[9] J. Baker and A. Collinson, "Electrical energy storage at the turn of the Millennium," *Power Engineering Journal,* vol. 13(3), pp. 107-112, 2002.

[10] H. Ibrahim, A. Ilinca and J. Perron, "Energy storage systems-characteristics and comparisons," *Renewable and Sustainable Energy Reviews,* vol. 12(5), pp. 1221-1250, 2008.

[11] R. Lasseter and P. Paigi, "Microgrid: A conceptual solution," Proceeding on IEEE 35th Annual Power Electronics Specialists Conference , vol. 6, pp. 4285-4290, Jun. 2004.

[12] F. Katiraei, R. Iravani, N. Hatziargyriou and A. Dimeas, "Microgrids management," *IEEE Power and Energy Magazine,* vol. 6, pp. 54-65, 2008.

[13] R. C. Bansal, T. S. Bhatti and D. P. Kothari, "On some of the design aspects of wind energy conversion systems," *Energy conversion and management*, vol. 43(16), pp. 2175-2187, 2002.

[14] P. Delarue, A. Bouscayrol, A. Tounzi, X. Guillaud and G. Lancigu, "Modelling, control and simulation of an overall wind energy conversion system," *Renewable Energy,* vol. 28(8), pp. 1169-1185, 2003.

[15] T. Petru and T. Thiringer, "Modeling of wind turbines for power system studies," *IEEE Transactions on Power Systems,* vol. 17(4), pp. 1132-1139, 2002.

[16] A. Hansen, C. Jauch, P. Sørensen, F. Iov and F. Blaabjerg, " Dynamic wind turbine models in power system simulation tool DIgSILENT," Risø National Laboratory for Sustainable Energy, 2007.

[17] D. Das, S.K. Aditya and D.P. Kothari, "Dynamics of diesel and wind turbine generators on an isolated power system," *International Journal of Electrical Power & Energy Systems,* vol. 21(3), pp. 183-189, 1999.

[18] E. Muljadi, S. Drouilhet and R. Holz "Analysis of wind power for battery charging," Proceeding on Wind Energy Symposium, pp. 190-19728, United States, Jan.- Feb. 1996.

[19] K. Yoshimoto, T. Nanahara and G. Koshimizu, "New control method for regulating state-of-charge of a battery in hybrid wind power/battery energy storage system," Proceeding on IEEE PES Power Systems Conference and Exposition, pp. 1244-1251, Oct.-Nov. 2006.

[20] A. Yazdani, "Islanded operation of a doubly-fed induction generator (DFIG) wind power system with integrated energy storage," IEEE Electrical Power Conference, pp. 153-159, Canada, Oct. 2007.

[21] "Outlook of energy storage technologies, 2007," Europian parliament policy department, available online: http://www.storiesproject.eu/docs/study_energy_storage_final.pdf.

[22] A. Khaligh and Z. Li, "Battery, ultracapacitor, fuel cell, and hybrid energy storage systems for electric, hybrid electric, fuel cell, and plug-in hybrid electric vehicles: state of the art," *IEEE Transactions on Vehicular Technology,* vol. 59(6), pp. 2806-2814, 2010.

[23] R. Cardenas, R. Pena, G. Asher and J. Clare, " Power smoothing in wind generation systems using a sensorless vector controlled induction machine driving a flywheel," *IEEE Transactions on Energy Conversion,* vol. 19(1), pp. 206-216, 2004.

[24] R. Takahashi, Wu Li, T. Murata and J. Tamura, "An application of flywheel energy storage system for wind energy conversion," Proceeding International Conference on Power Electronics and Drives Systems, pp. 932-937, Kuala Lumpur, Apr. 2006.

[25] S. Nomura, *et al.*, "Wind farms linked by SMES systems," *IEEE Transactions on, Applied Superconductivity,* vol. 15(2), pp. 1951-1954, 2005.

[26] M. Sheikh, S. Muyeen, R. Takahashi and J. Tamura, " Smoothing control of wind generator output fluctuations by using superconducting Magnetic Energy Storage unit," Proceeding International Conference on Electrical Machines and Systems, pp. 1-6, Nov. 2009.

[27] C. Abbey and G. Joos, "Supercapacitor energy storage for wind energy applications," *IEEE Transactions on Industry Applications,* vol. 43(3), pp. 769-776, 2007.

[28] X. Li, C. Hu, C. Liu and D. Xu, "Modeling and control of aggregated super-capacitor energy storage system for wind power generation," Proceeding on 34th Annual Conference of IEEE Industrial Electronics, pp. 3370-3375, Nov. 2008.

[29] L. Ntziachristos, C. Kouridis, Z. Samaras and K. Pattas, "A wind-power fuel-cell hybrid system study on the non-interconnected Aegean islands grid," Renewable Energy, vol. 30(10), pp. 1471-1487, 2005.

[30] O.C. Onar, M. Uzunoglu and M.S. Alam, "Modeling, control and simulation of an autonomous wind turbine/photovoltaic/fuel cell/ultracapacitor," *Journal of Power Sources,* vol. 185(2), pp. 1273-1283, Dec. 2008.

[31] W. Caisheng and M. H. Nehrir, "Power management of a stand-alone wind/photovoltaic/Fuelcell energy system," *IEEE Transaction on Energy Conversion,* vol. 23(3), pp. 957-967, Sep. 2008.

Chapter 2 System Configuration and Sizing

2.1 Introduction

In this study, a multi sources hybrid distributed generation system–consisting of a wind turbine generator system (WTGS), a fuel cell (FC), an electrolyzer (ELZ) and an ultracapacitor (UC)–is proposed. Wind is the primary power source of the system to take the full advantage of renewable energy around us. Since a reliable storage system is necessary with wind power, an FC/ELZ/UC mix system is employed for the power and energy management. The FC/ELZ combination is used as a backup and long term storage system, whereas the UC unit is used for the fast transient and ripple power mitigation. In the following sections, a brief discussion of the hybrid distributed energy resources is presented first, followed by the detailed system configuration and unit sizing. The system components modeling and the system control schemes will be discussed in chapter three and chapter four respectively.

2.2 Wind Turbine Generator System

The wind turbine generator system (WTGS) is a structure that converts kinetic energy of wind into the electrical energy. The major components of a typical wind energy conversion system include a wind turbine, a generator, interconnection units, and control systems. The electromechanical conversion technologies adopted for wind turbines are synchronous and induction generators. For small to medium power wind turbines, permanent magnet synchronous generators or squirrel-cage induction generators are often used because of their reliability and cost effective technologies, whereas doubly-fed induction generators (DFIGs) or permanent magnet synchronous generators are currently used for the medium to high power wind turbines.

Modern wind turbines can be classified broadly as the fixed-speed and variable-speed wind turbines. The fixed-speed wind turbines are directly connected to the grid using squirrel-cage induction generators for electro-mechanical power conversion. The induction generator requires reactive power to operate, which can be either supplied from the utility grid or by capacitors connected at the machine terminals (see Fig. 2-1(a)). These generators cannot deliver any reactive power and generally require a soft-starter to reduce the inrush current during the start-up [1].

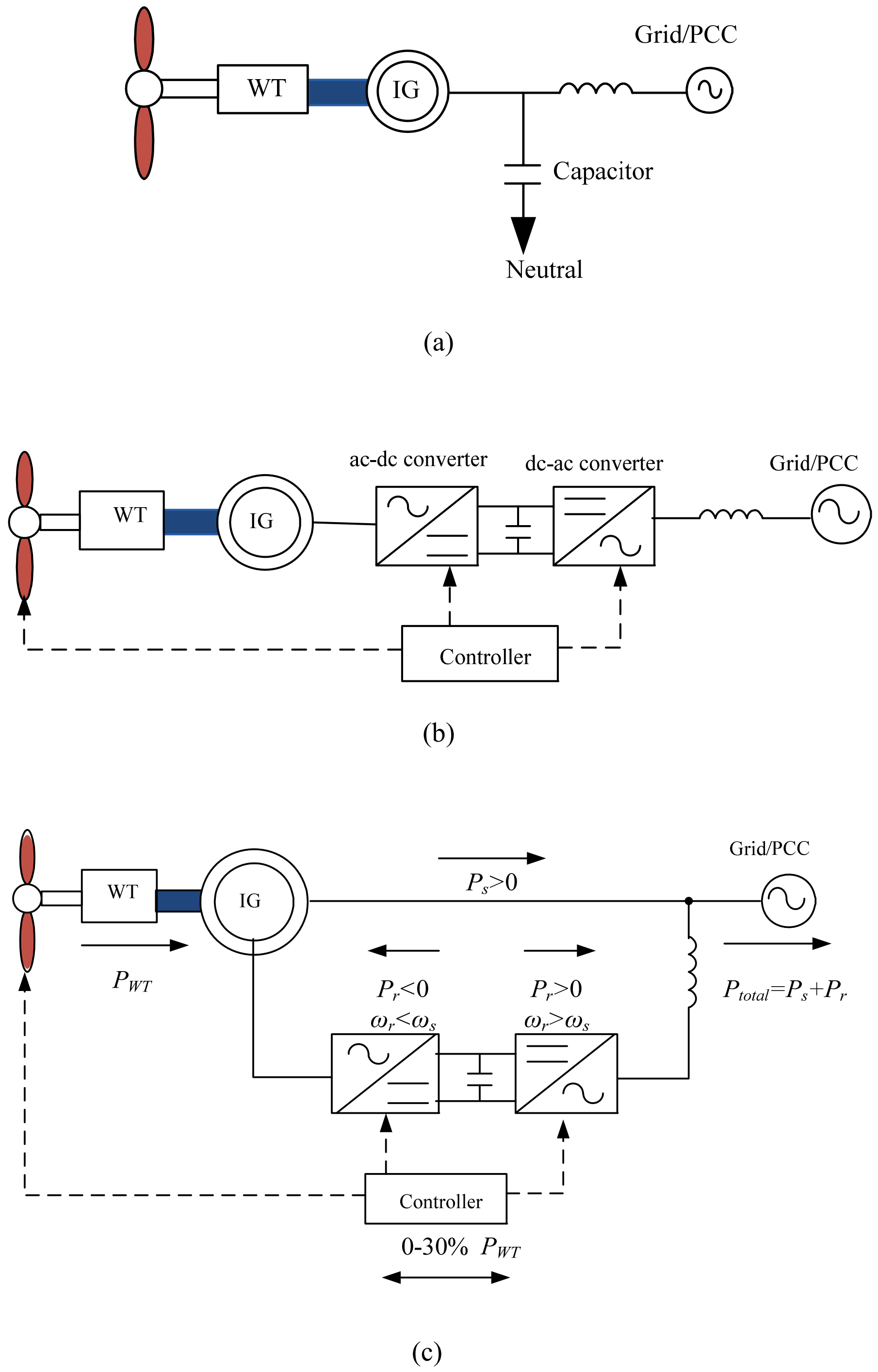

Fig. 2-1 Types of WTGSs. (a) Fixed-speed WTGS, (b) full-scale converter based WTGS, and (c) partial-scale converter based WTGS. Here, P_s, P_r, P_{WT}, ω_r and ω_s represent stator active power, rotor active power, power from wind turbine, rotor angular speed and synchronous speed of rotating flux, respectively.

The variable-speed wind turbines (WTs) use power electronic converters (PECs) that act as interfacing devices to achieve power control, soft start, and interconnection functions. These WTs are further classified into the turbines with full-scale and partial-scale rated PECs systems. With the full-scale rated converter system, the generators are usually conventional or permanent magnet type synchronous generators to convert the turbine power into the variable-frequency variable-voltage electric power that changes with the wind speed (see Fig. 2-1 (b)). A power electronic based rectifier and an inverter are then used to convert the generator output power to the power that is compatible with the utility system. This topology causes extra losses in the power conversion system, but it provides the additional power gain through the variable-speed operation by capturing more energy from the wind [1], [2].

In this study, partial-scale rated PECs system is used, which is a compromising solution between fixed-speed operation (in term of cost) and full-scale PEC based variable-speed operation (in term of operational flexibility). This configuration has been widely adopted commercially in medium to large scale WTGSs. With the partially-rated converter system, a DFIG is used as the electro-mechanical power conversion system, in which a voltage source converter (VSC) connected to the rotor through slip rings controls the rotor current (see Fig. 2-1 (c)). This configuration enables the WTGS to have some degree of variable-speed operation. If the generator is running super-synchronously, the electrical power (P_{total}) is delivered through both the rotor (P_r) and the stator (P_s). If the generator is running sub-synchronously, the electrical power is delivered into the grid through the stator terminal only. The advantage of this design is that it provides reactive power compensation and increased energy capture from the wind. This arrangement further allows the rectifier system to undersize about 30% of the full load value, which equals to the maximum power flow from the rotor circuits [2].

2.3 Fuel Cells

Fuel cells are the static electrochemical devices which convert chemical energy of H_2 fuel into electrical energy. They generate electricity inside a cell through reactions between a fuel (H_2) and an oxidant (O_2) in the presence of an electrolyte, in which the reactants flow into the cell and the products flow out of it. Unlike conventional electrochemical batteries, fuel cells are the thermodynamically open system, such that the reactant from the external source is consumed [3]. By contrast, the batteries store electrical energy chemically, and hence represent a thermodynamically closed system.

The difference between the fuel cell and a combustion engine depends on the manner by which energy is converted. In internal combustion engines, the heat generated from combustion needs to be converted into mechanical energy and then into electrical energy, causing losses at each level of transformation. In contrast, fuel cells directly produce electricity from the chemical reaction. Fuel cells offer numerous advantages over conventional power plants to help them achieve the goal and widespread adoption, such as [4]:

- high efficiency even at partial load,
- few moving parts resulting in quiet operation, higher reliability, lower maintenance and longer operating life,
- fuel diversity,
- zero or low emission of greenhouse gases,
- combined heat and power capability, without the need for additional systems (i.e., low temperature fuel cells can provide district heating, while high temperature fuel cells can provide high-quality industrial steam),
- flexible and modular structure, and
- increased energy security by reducing the reliance on large central power plants and oil imports.

In a typical fuel cell, fuel is fed continuously to the anode and oxidant is fed continuously to the cathode. The electrochemical reactions take place at the electrodes to convert chemical energy into electricity. The anode is the electrode from which electrons leave and cathode is the electrode to which the electrons are coming. The most commonly used fuel for fuel cells is hydrogen, while oxygen or air acts as the oxidant. Among the various types of fuel cells (FCs), the polymer electrolyte membrane fuel cell (PEMFC) and solid oxide fuel cell (SOFC) have good prospective for the distributed power generation [4-6]. In a PEMFC, H^+ flows across the electrolyte as a charge carrier producing H_2O at the cathode; whereas O^{2-} flows across the electrolyte as the charge carrier in an SOFC, producing H_2O at the anode. The respective electrochemical phenomena are also illustrated in Fig. 2-2.

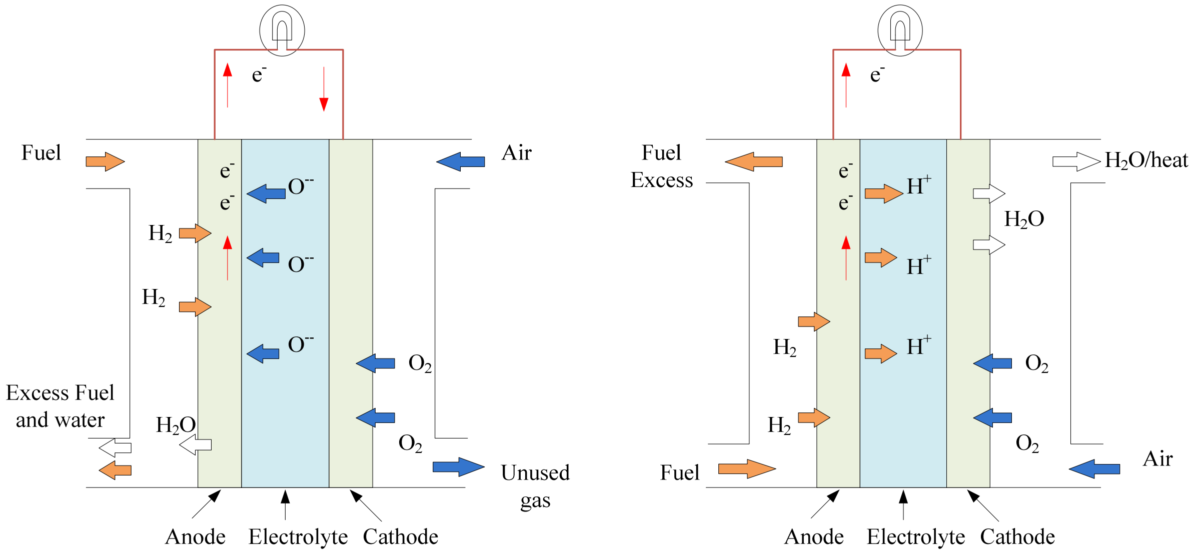

(a) (b)

Fig. 2-2 Schematic block diagram of FCs. (a) SOFC (b) PEMFC

In this dissertation, the SOFC has been utilized because of its notable merits: high efficiency, long-term stability, fuel flexibility, low emissions, and relatively low cost, despite of their few constraints related to the high operating temperature which results in longer start-up times and mechanical/chemical compatibility issues. The energy conversion efficiency of the SOFC stack can reach up to 65% and its overall efficiency with combined heat and power applications, can reach even above 80% [7], [8]. Further, due to the high operating temperature, the SOFC allows internal reforming of gaseous fuel inside the fuel cell, providing the multi-fuel applicability [4].

2.4 Ultracapacitor

Ultracapacitors (supercapacitors, double-layer capacitors or electrochemical capacitors) are energy storage devices which polarize an electrolytic solution to store energy electrostatically. Though it is an electrochemical device, no chemical reactions are involved in its energy storage mechanism. The storage mechanism is highly reversible that allows the UC to be charged and discharged hundreds of thousands of times. Consequently, it can store more energy than traditional capacitors and discharge this energy at higher rates than rechargeable batteries. Ultracapacitors are notable for their ability to store more energy per unit weight and volume than conventional capacitors. Therefore, UCs are attractive in power application for transient mitigation with renewable power generation systems and plug-in-hybrid-vehicles [9],[10].

Fig. 2-3 depicts the schematic diagram of an ultracapacitor cell, which can be viewed as two nonreactive porous plates, or collectors, suspended within an electrolyte. The main factors determining how much electrical energy a capacitor can store are: the surface area of the electrodes, their distance from each other, and the dielectric constant of the material separating them. Because of the presence of porous material having pore diameter in the nanometer range, the charge can be sponged into it, and the effective surface area will be more than 100000 times than the outer surface area. Consequently, the capacitance would be very high because more charge can be stored on larger surface area in compare with the conventional capacitor having the same size [10], [11].

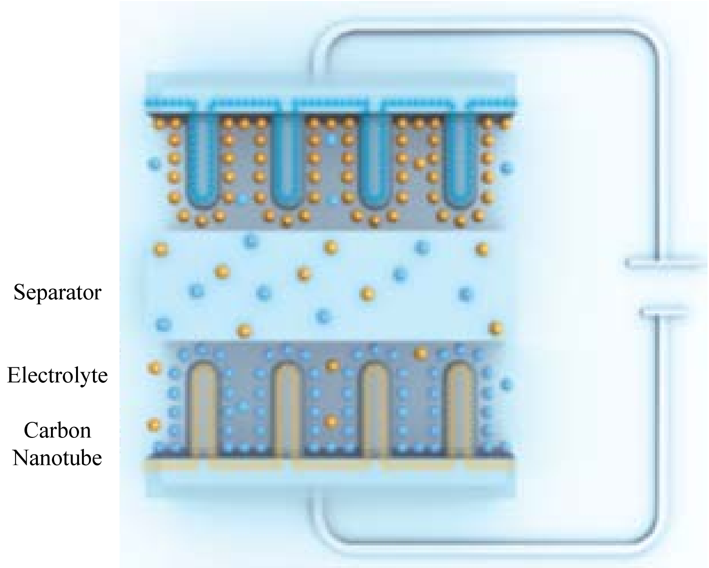

Fig. 2-3 Schematic diagram of a typical UC. With finer dimensions and more uniform distribution, carbon nanotubes enable greater energy storage in ultracapacitors than activated carbon does. The photograph is taken from [10].

The competitive technologies of UCs, in terms of the transient mitigation ability characterized by their high power density, are the flywheel, SMESs and battery systems (see Table A.1 in appendix). These technologies have own merits and demerits. Despite of the mature and cost effective solution, the application of lead acid battery is limited due to its limited charging and discharging cycle and the disposal problem. Although the flywheel demonstrates a high efficiency, it requires large space for the moving part. In case of the SMES, its wide scale application is limited due to its high cost per kWh, unless some breakthroughs are achieved in its technologies. Therefore, the UC is adopted in this study as a compromising candidate in terms of cost, compatibility, efficiency and operating life.

2.5 Electrolyzer

In the context of H_2 technology, electrolyzers (ELZs) are the devices to produce hydrogen and oxygen from the electrolysis of water, which can be widely distributed to meet the hydrogen and oxygen requirements of different users, such as renewable energy systems, fueling stations and industrial applications. Recently, there is a rising trend of utilizing ELZs as distributed energy resources with the renewable power systems like photovoltaic (PV), wind power and small hydro power generation systems [12], [13].

The electrolysis process can also be considered as the reverse process of hydrogen fueled fuel cell, in which H_2 and O_2 undergo electrochemical reaction to generate power. When an electrical power source is connected to two electrodes (typically made from some inert metal such as platinum or stainless steel) and placed in the water, hydrogen is produced at the cathode and oxygen is produced at the anode. The electrolysis cells are characterized by their electrolyte type. There are two types of low temperature electrolysis: alkaline and proton exchange membrane. Alkaline electrolysis utilizes a liquid electrolyte consisting of highly concentrated potassium hydroxide (KOH), whereas the proton exchange membrane electrolysis is based on the use of a solid conducting polymer that conducts ions when hydrated with water.

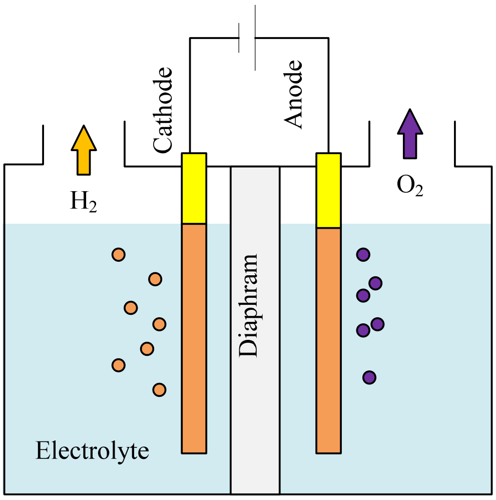

Fig. 2-4 Schemaic diagram of alkaline electrolyzer.

Among these electrolyzers, the alkaline electrolyzer (AE) is the well-established and the dominating technology today with its availability in a wide range of power ratings at a lower cost, therefore alkaline water electrolysis is adopted in this study. Fig. 2-4 depicts the operating principle of an AE which employs an alkali solution (usually potassium hydroxide of around 25-30% concentration at 80°C) as the electrolyte for providing the ion-transfer process. Typical current densities of the AE are 0.2-0.4 A/cm^2 and designed for either atmospheric or operation at up to 30 bar. The energy conversion efficiencies can range from 60 to 90%. Without auxiliary purification equipment, purities of 99.8% for H_2 can be achieved. The alkaline electrolysis technology can be implemented at a variety of scales from less than 1 kW to large industrial electrolyzer plant over 100 MW as long as there is availability of a proper dc electricity supply [14].

2.6 Power Electronic Converters

Due to uncertain and variable nature of energy input, the voltage and frequency from renewable power sources vary accordingly. Therefore, unlike the conventional generators, they cannot be connected to the point of common coupling (PCC) bus directly. Further, most of the distributed power sources generate power in a dc form, which is not compatible with the ac load or the power network. A power electronic converter (PEC) system plays a vital role to match the characteristics of the distributed generation units and the requirements of the interconnection; including the frequency, voltage, the active and reactive power regulation, minimization of harmonics, among the others [8]. Therefore, power electronics technology is an indispensable part of any renewable power systems, and it often shares upto 40% cost of the combined system [15], [16].

A PEC system accepts power from the distributed energy source and converts it into the desired voltage and frequency level. There are various types of PEC topologies, namely ac-ac, ac-dc, dc-ac and dc-dc interfaces. The choice of a particular one is specific to the type of the energy source or the storage application. An ac-ac conversion topology, such as cycloconverters or matrix converters, is used when power is generated in ac form with a frequency different from the load frequency like in microturbines, wind power etc. The ac-dc conversion topology, also known as the rectifier, is utilized to generate a controlled dc voltage from either an uncontrolled ac source (i.e., microturbine, wind turbine) or a controlled ac source (i.e., utility supply) [17]. For dc output systems like photo voltaics, fuel cells, batteries and ultracapacitors, a dc-dc converter is typically needed to change the dc voltage level. The dc-ac inverter is the most generic converter which converts a dc source to the grid-compatible ac power. Further, a bidirectional interfacing is required with the storage systems to exchange power with the external system. Table 2.1 summarizes the type of the power electronic conversion topologies to be used with distributed energy resources (DERs).

Table 2.1 Power electronic converters for different distributed energy resources

Distributed energy resources type	Power conversion	Common module name
Wind, micro-turbine, Internal combustion engine, flywheel	ac-dc	Rectifier
Battery, SMES	dc-ac	Inverter
Fuel cell, electrolyzer, ultracapacitor, SMES	dc-dc	Boost, buck, buck-boost, chopper
Wind, micro-turbine	ac-ac	Cycloconverter, matrix converter
Wind turbine, flywheel	ac-dc-ac	Back-to-back converter, rectifier inverter

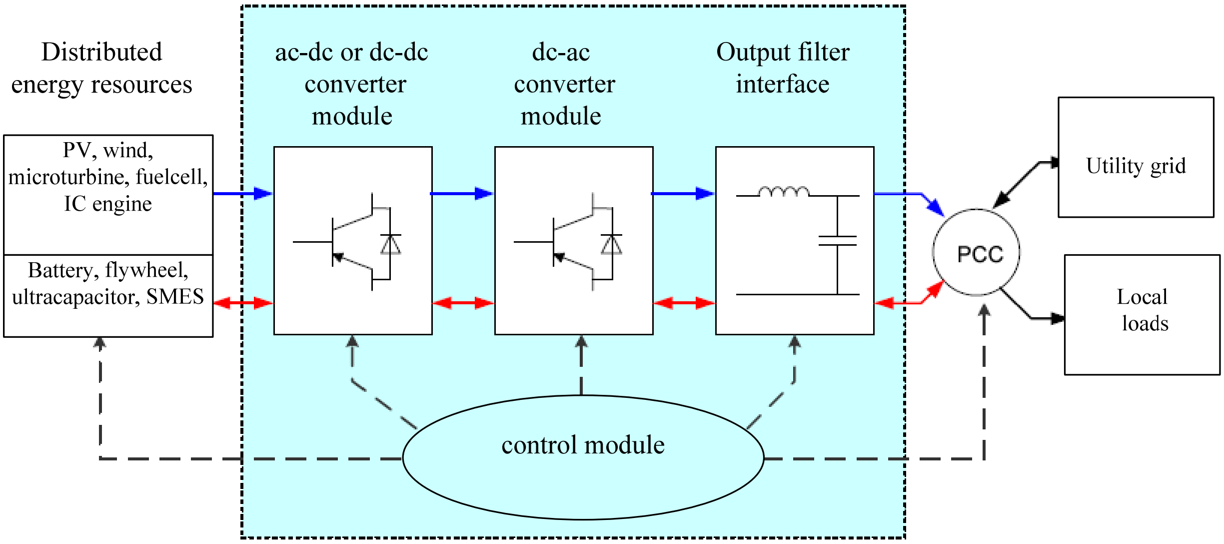

Fig. 2-5 General block diagram of power electronic converters for DERs.

A general approach to organize the interface into modules, in which each can be designed with a range of distributed generators (DGs) and storages, is illustrated in Fig. 2-5. It includes four major modules for a power electronic conversion, namely the source input converter module, an inverter module, the output interface module and the controller module. The first and second modules are the power electronic converter units, while the third and fourth are their associative parts. The blue unidirectional arrows depict the power flow path for the distributed energy resources, whereas the red arrows show the bidirectional power flows for the energy storage devices [16], [18].

In this study, wind power represents the DG unit, and a UC, an SOFC and an ELZ are utilized as the energy storage devices. As explained in the earlier section, the wind turbine adopts the back-to-back ac-dc-ac converters. Unlike in a usual DFIG configuration where the rotor side converter (ac-dc) and the line-side converter (dc-ac) are equally rated, the configuration in this study adopts a full-scale line-side converter. The reason of the increased size of the line-side converter is to handle the storage system to be connected to the intermediate dc bus. For the SOFC/ELZ and the UC, a two stages dc-dc conversion system is applied; in which the bidirectional chopper accommodates the SOFC and ELZ, and the full bridge isolated dc-dc converter regulates the dc-link voltage isolating the energy storage system from the rest of the network. The detailed configuration, topology and sizing of the hybrid system are discussed in the following sections.

2.7 Layout of Proposed Scheme

In a hybrid power system, DGs can provide the terminal power in the form of dc or ac, so their integration can be done through the ac or dc coupling. In a dc coupling configuration, different alternative energy sources are connected to a dc bus through appropriate power electronic converters. Then the dc energy is converted into 60 Hz (or 50 Hz) ac form through a dc-ac converter which can be bi-directional. The dc consumers are also coupled to the dc side, whereas the ac consumers are connected to the ac terminal of the inverter. The power range for dc coupled hybrid systems is broad and can be used cost-effectively for various off-grid applications. In this configuration, any numbers of DGs can be connected to the dc bus with a proper power management scheme and seen as a “virtual power plant” from the grid side. In an ac coupled hybrid system, the DGs are linked at the regulated ac bus through proper PEC(s). In general, when systems increase in size, they are implemented as ac coupled hybrid systems, and the extent to which dc buses are avoided can vary. In the ac coupled hybrid systems, an island grid or an isolated microgrid is built and different concepts can be utilized to operate it. One of the merits of ac linked systems is that the inverter can be employed to share active/reactive power in a relatively easy control structure [21].

In the both concepts mentioned above, the system has to cope with extra losses due to the inversion and rectification of the current for each energy flow. This two-stages conversion significantly reduces the overall system efficiency, since the number of PECs is not optimized. The third hybrid configuration, which is the mix of both ac and dc coupling, can be designed to exploit the benefit of both configurations by optimizing the number of converters used, so it is adopted in this study.

The schematic diagram of the proposed wind power and storage system (WPSS) is illustrated in Fig. 2-6. The system consists of a wind turbine, a doubly-fed induction generator (DFIG), a dedicated energy storage system (DESS), two bi-directional voltage source converters (VSC1 and VSC2) and the local load. The configuration can be visualized as a subset of a consumer scale local network or a microgrid that can be operated autonomously in different modes. For the medium size power generation, the DFIG is a recommended choice due to its variable speed operation with a reduced size of the ac-dc-ac converter [2], so the DFIG is adopted here with a partially rated (30%) ac-dc conversion system (VSC1). In this topology, the rating of the line-side dc-ac converter (VSC2) is higher, because it should handle the storage power as well. The stator terminals of the DFIG are directly connected to the ac bus, whereas the rotor terminals are connected to the intermediate dc bus through VSC1, so that the rotor circuit would participate to transfer active and reactive power. As shown in the figure, the line-side converter and the DESS are connected in parallel at the dc link bus. The line-side converter provides the power electronic conversion between the regulated dc-link bus and the coupling bus (bus #2). In the conventional operation as the grid-connected non-dispatchable power source, line-side converters are mainly assigned to control dc-link voltage and ensures the converter operation at the desired power factor. By introducing the DESS at the dc-link bus, the line-side converter provides the increased flexibility of operation that evolves the WPSS, making it self-sustainable and dispatchable entity. The ac buses (bus #1 and bus #2) may either be lumped in a single bus or connected by a line depending on their distance. The whole system is connected to the local distribution grid via a breaker (B) whose switching state decides whether the system is in islanded or grid-connected mode.

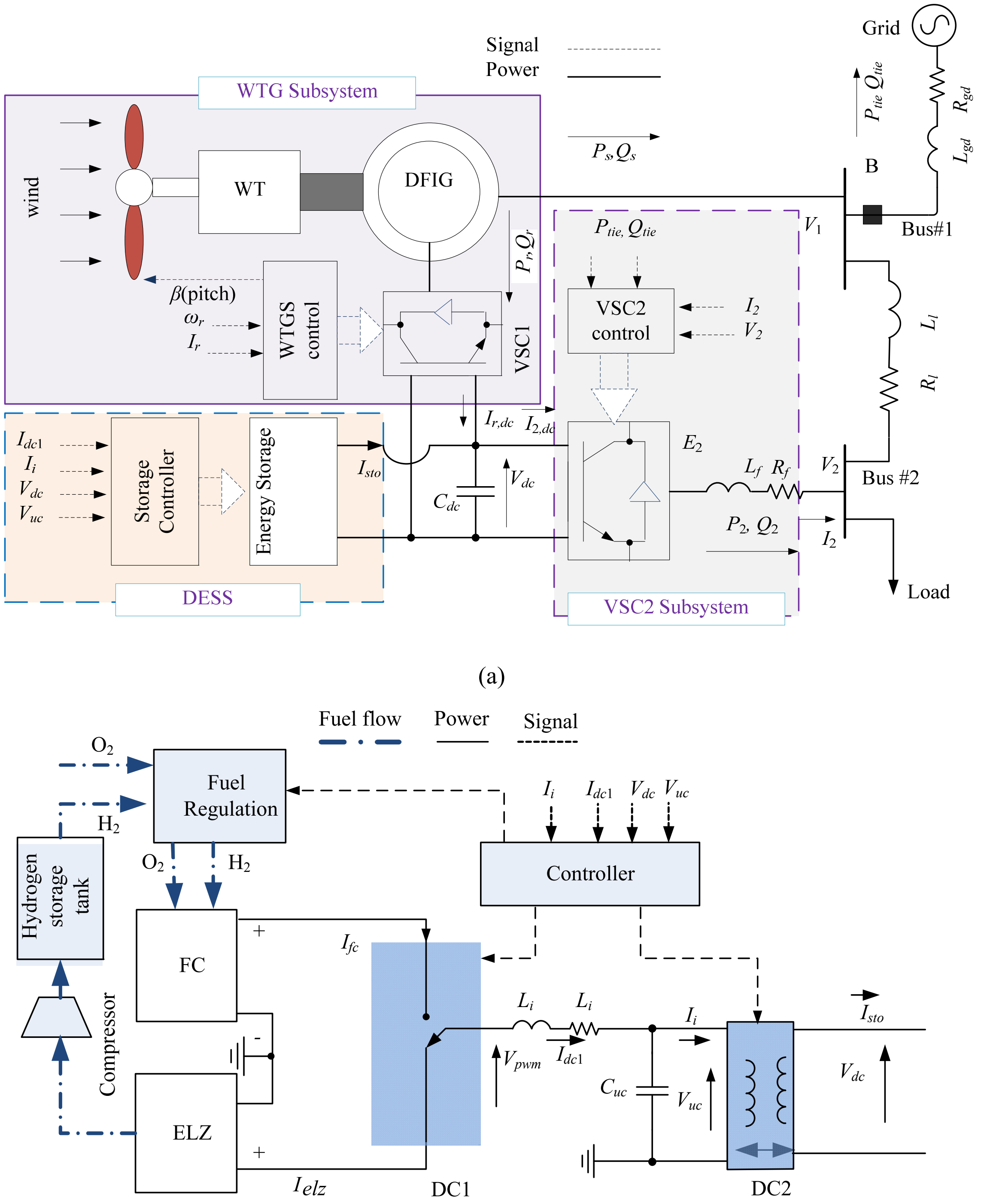

(a)

(b)

Fig. 2-6 Schematic diagram of proposed system. (a) Overall system topology, and (b) the dedicated energy storage subsystem. Here the symbols I, V, P, Q, L and R represent the current, voltage, active power, reactive power, inductance and resistance, respectively, and the subscripts denote the quantities for the corresponding part/unit.

The configuration of the DESS consists of an UC, a solid oxide fuel cell (SOFC) and an ELZ with a H_2 storage tank, as illustrated in Fig. 2-6(b). The UC and the SOFC/ELZ are connected electrically at the dc-link bus through dc-dc interfaces, DC1 and DC2. It is notable that the proposed scheme accommodates the ELZ and SOFC as a single unit, which can share the same converter (DC1) for the control of current flow. The DESS is capable of performing versatile activities; it monitors and controls many variables (currents and voltages of the UC, SOFC and ELZ, and fuel flow) which are applicable to manage transient and long-term power balance. The DESS can also assist in the supervisory control and demand response by providing the information of fuel reserve. In the worst case, when there is no reserve of H_2 or the DESS is out of service, it delivers its status signal to the VSC2 subsystem availing to alter the latter's operational scheme without disruption.

Since the power from the DFIG is non-dispatchable in nature and often regarded as a negative load or disturbance input, the DESS plays a role of the reliable power/energy balancing source. In particular, it is responsible for the voltage control of dc-link bus (V_{dc}) by enabling DC1 to inject the fast transient power and DC2 for the steady state power balance. The main focus of DC2 control action is on the inherently slow fuel cell dynamics which renders it unable in tracking fast current, leading to undesired pressure drop and fuel starvation [6]. During the surplus of power, ELZ/UC is operated to produce the H_2, while SOFC/UC comes into effect during the power deficit by the consumption of H_2. As a consequence, VSC2 becomes the fully controllable unit responsible for the voltage (reactive power) and the frequency (active power) regulation of bus #2 by adjusting the unbalanced power with the DESS.

2.8 Unit Sizing

Unit sizing in a power system is actually a multi-objective optimization problem that addresses number of operational criteria; such as minimizing the electricity production cost, ensuring that the load is served according to certain reliability criteria, and minimizing the loss [19], [20]. In the case of a generation system that uses renewable sources, the sizing is more complex in comparison with the conventional systems, due to the randomness of the renewable resources and the high cost of wind generators and storage modules [20]. Since the investigation of optimal unit sizing is beyond the scope, this study considers the operating requirement of the system in sizing the individual components.

While sizing the units, it is roughly estimated that the generation of energy would match the demand in long term by using H_2 storage, with no need of importing it. The maximum load of the system is kept equal to the rated capacity of the WTGS as 50 kW. Assuming that 20% of the connected load can be curtailed, an SOFC with 40 kW would be able to supply uninterruptable load during the worst situation when the DFIG is not generating any power. Similarly, the size of the ELZ is selected considering the extreme situation that the rated power from the WTGS would be consumed by the ELZ, with all loads are switched off. That would make the rating of the ELZ about 50 kW. The ratings of the other components (DC1, DC2 and VSCs) are selected as the technical demand of the configuration. That would make the ratings of DC1 and DC2 as 50 kW, the rating of rotor side converter (VSC1) as 20 kVA, and the rating of line-side converter (VSC2) as 75 kVA.

2.9 Summary

This chapter presented a brief discussion of hybrid distributed energy sources and power electronic conversion mediums utilized in the study. Distributed energy sources consist of diverse nature of generators that produce electricity in dc or ac forms. Beginning with brief discussion of energy resources and power electronic converters, the layout of proposed system has been illustrated in detail followed by the unit sizing of the system.

References

[1] Z. Chen and F. Blaabjerg, "Wind Energy –The World’s Fastest Growing Energy Source," *IEEE Power Electronics Society ,* Third Quarter Newsletter*,* 2006.

[2] F. Blaabjerg and Z. Chen, "Power electronics for modern wind turbines," *Synthesis Lectures on Power Electronics,* vol. 1, pp. 1-68, 2005.

[3] M. Winter and R. Brodd, "What are batteries, fuel cells, and supercapacitors?," *Chem. Rev,* vol. 104, pp. 4245-4270, 2004.

[4] A. Dicks and J. Larminie, *Fuel cell systems explained*: John Wiley & Sons, 2000.

[5] O.C. Onar, M. Uzunoglu and M.S. Alam, "Modeling, control and simulation of an autonomous wind turbine/photovoltaic/fuel cell/ultracapacitor," *Journal of Power Sources,* vol. 185(2), pp. 1273-1283, Dec. 2008.

[6] P. Thounthong, S. Raël and B. Davat, "Control strategy of fuel cell and supercapacitors association for a distributed generation system”, *IEEE Transactions on Industrial Electronics,* vol. 54(6), pp. 3225 - 3233, Dec. 2007.

[7] C. Wang and H. Nehrir, "A physically based dynamic model of solid oxide fuel cells," *IEEE Transaction on Energy Conversion,* vol. 22(4), pp. 887 - 897, Dec. 2007.

[8] F. Blaabjerg, Z. Chen and S. Kjaer, "Power electronics as efficient interface in dispersed power generation systems," *IEEE Transactions on Power Electronics,* vol. 19(5), pp. 1144-1154, Sep. 2004.

[9] C. Abbey and G. Joos, "Supercapacitor energy storage for wind energy applications," *IEEE Transactions on Industry Applications,* vol. 43(3), pp. 769-776, 2007.

[10] J. Schindall, "The charge of the ultracapacitors," *IEEE Spectrum,* vol. 44, pp. 42-46, 2007.

[11] A. Burke, "Ultracapacitors: why, how, and where is the technology," *Journal of power sources,* vol. 91(1), pp. 37-50, 2000.

[12] T. Zhou and B. Francois, “Modeling and control design of hydrogen production process for an active hydrogen/wind hybrid power," *International Journal of Hydrogen Energy,* vol. 34(1), pp. 21-30, Jan. 2009.

[13] Z. Yumurtaci and E. Bilgen, "Hydrogen production from excess power in small hydroelectric installations," *International Journal of Hydrogen Energy,* vol. 29(7), pp. 687-693, Jul. 2004.

[14] A. Smith and M. Newborough, "Low-cost polymer electrolysers and electrolyser implementation scenarios for carbon abatement," Report to the Carbon Trust and ITM Power*,* 2004.

[15] S. Blazewicz, "Distributed energy resources integration research program power electronics research assessment," Navigant Consulting California Energy Commission vol. CEC-500-2005-206, Sep. 2005.

[16] W. Kramer, S. Chakraborty, B. Kroposki, and H. Thomas, "Advanced power electronic interfaces for distributed energy systems part 1: systems and topologies," National Renewable Energy Laboratory, Golden, Colorado, Tech. Rep. NREL/TP-581-42672, 2008.

[17] Y. Khersonsky and G. Robinson, "PEBB modules in distributed generation applications," IEEE Power Engineering Society General Meeting, Jul. 2003.

[18] S. Chakraborty, B. Kramer and B. Kroposki, "A review of power electronics interfaces for distributed energy systems towards achieving low-cost modular design," *Renewable and Sustainable Energy Reviews,* vol. 13(9), pp. 2323-2335, 2009.

[19] R. Chedid and S. Rahman, "Unit sizing and control of hybrid wind-solar power systems," *IEEE Transactions on Energy Conversion,* vol. 12(1), pp. 79-85, 1997.

[20] D.B. Nelson, M.H. Nehrir and C. Wang, "Unit sizing and cost analysis of stand-alone hybrid wind/PV/fuel cell power generation systems," *Renewable energy Journal,* vol. 31(10), pp. 1641-1656, 2006.

[21] K. Moutawakkil and S. Elster, "RE hybrid systems: Coupling of Renewable Energy Sources on the AC and DC Side of the Inverter" *Refocus*, vol.7(5), pp. 46-48, 2007.

Chapter 3 System Modeling

The previous chapters described reasons for the interest and application of two time scale based energy storage system, namely the electro-chemical based long-term energy storage and the utracapacitor based short term energy storage in a wind power based microgrid, with the suitable inter-connecting layouts and sizing. This chapter will investigate the appropriate models of the components applicable to this study, and provide a detailed mathematical treatment to each of them; thereby presenting a computational platform useful for analyzing the hybrid power system.

For the effective analysis and testing, it is better to have a real time set up and observations of the system. However, this approach presents some drawbacks which cannot be overlooked, such as high costs of the elements under test, the infrastructure and security requirements (especially for a hydrogen storage and supply system) and the complexity associated to the performance of the test when a high number of elements are involved. Therefore, the most cost effective approach at the designing stage is to carry out computational analysis based upon the mathematical models involved in the system. Although a physical system cannot exactly be described by a mathematical expression, it is often convenient to utilize an approximated model for design and analysis purposes in engineering systems. In our case, the system includes a large number of components with diverse nature of dynamics. Since it is too complex and time consuming to take account of the dynamics in much greater depth, we will adopt those models which are adequate and simple enough to observe the system behaviors within the framework of the research objectives.

On this ground, the following sections will explain the dynamic model of the subsystems, namely the dedicated energy storage system (DESS), the wind turbine generator system (WTGS) and the line-side converter system. The DESS includes a fuel cell, an electrolyzer, an ultracapacitor, two dc-dc converters, and a H_2 regulation/storage unit. The WTGS includes a wind turbine, a doubly-fed induction generator (DFIG) and a voltage source converter (VSC1). Likewise, the line-side converter system has a voltage source converter unit (VSC2). In the following sections, the dynamic model for each of the subsystems is presented in detail. These models will be used in chapter four to design the control and management schemes and in chapter five to investigate operational modes and behavior of the overall system through numerical simulations.

3.1 Wind Energy Estimation

The energy of wind is in its kinetic which is a varying quantity affected by several factors, such as geographic location, climate characteristics, height above ground, and surface topography. Wind turbines interact with the wind, capture part of its kinetic energy, and convert it into the usable energy. The knowledge of the wind distribution is very crucial in designing and sizing of a wind energy conversion system. The most commonly used probability density function to describe the wind speed and available energy is the *Weibull function*, based upon the annual wind speed data [1]. The *Weibull distribution* is described by the following probability function,

$$f(v_w) = \frac{k}{c}\left(\frac{v_w}{c}\right)^{k-1} e^{-(v_w/c)^k}, \tag{3.1}$$

where k is a shape parameter, c is a scale parameter and v_w is the wind speed. The average wind speed (or the expected wind speed) can be calculated as

$$\overline{v}_w = \int_0^{\infty} v_w f(v_w)dv_w = \frac{c}{k}\Gamma\left(\frac{1}{k}\right), \tag{3.2}$$

where Γ is the *Eular Gamma function* defined by

$$\Gamma(z) = \int_0^{\infty} t^{z-1}e^{-t}dt. \tag{3.3}$$

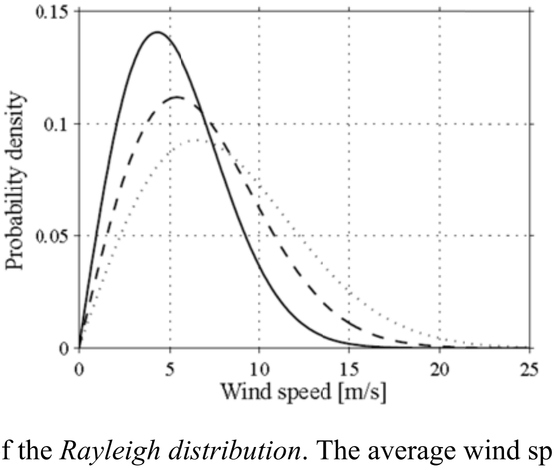

Fig. 3-1 Probability density of the *Rayleigh distribution*. The average wind speeds are 5.4 m/s (solid), 6.8 m/s (dashed) and 8.2 m/s (dotted).

For the application of wind power system, the *Weibull distribution function* can be reduced to the single parameter model, in which k = 2, such that a simpler *Rayleigh distribution* is constructed. Fig. 3-1 shows the annual *Rayleigh distribution* of wind speed. The average wind speeds in the figure are 5.4 m/s, 6.8 m/s and 8.2 m/s. A wind speed of 5.4 m/s correspond to a medium wind speed site in Sweden [2], while 8–9 m/s are wind speeds available at sites located outside the Danish west coast [3].

The probability distribution function is utilized in sizing the wind turbine and determining its rated wind speed. Considering the aerodynamic power in the wind passing through an area (A_w) as

$$P_{wind} = \frac{\rho}{2} A_w v_w^3, \tag{3.4}$$

the average power in the wind would be [1]

$$\bar{P}_{wind} = \frac{\rho}{2} A_w \int_0^{\infty} v_w^3 f(v_w) dv_w. \tag{3.5}$$

Here, ρ represents the density of air. The function $v_w^3 f(v_w)$ starts at zero for $v_w = 0$, reaches a peak value at some wind speed v_{wm} and finally returns to zero at large values of v_w. The yearly energy production in kWh at the wind speed v_w is the power obtained multiplied by the number of hours in the year. The wind speed v_{wm} is the speed which produces more energy than any other wind speed. Therefore, the maximum energy obtained from the given wind speed v_{wm} is

$$W_{\max} = \frac{\rho}{2} 8760 A_w v_{wm}^3 f(v_{wm}). \tag{3.6}$$

The turbine should be designed to maximize the energy in its best operating wind speed range. Some applications will even require a turbine to be designed with a rated wind speed equal to v_{wm}. This can be found by multiplying right hand side of (3.1) by v_w^3, setting the derivative equal to zero, and solving for v_w as

$$v_{wm} = c\left(\frac{k+2}{k}\right)^{1/k}. \tag{3.7}$$

Thus, we see that v_{wm} is greater than c, so it will be greater than the mean speed, $\bar{v}_w$. If the mean speed is 6 m/s, then v_{wm} will typically be about 8 or 9 m/s.

3.2 Wind Turbine Generator System

A general structure of a WTGS is depicted in Fig. 3-2. It consists of important subsystem models; a wind speed model, a rotor, a drive train and a generator. In this section, the modeling of these subsystems, which are of interest in this thesis, are discussed.

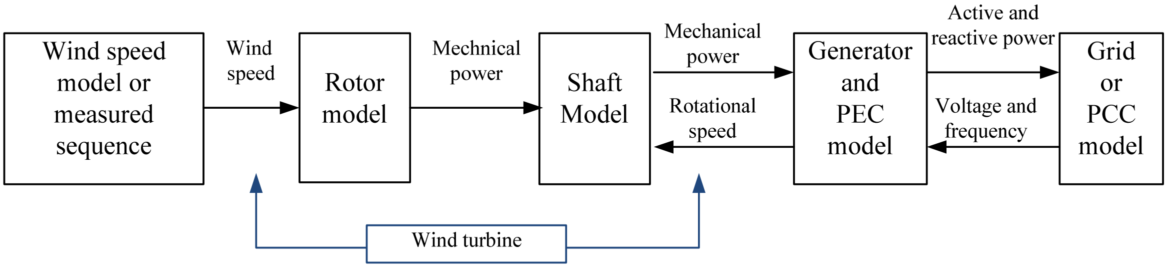

Fig. 3-2 General structure of a wind turbine generator system.

3.2.1 Wind speed model

The wind speed model gives the time series data of wind speed. One approach to model a wind speed sequence is to use data from measurements. If the certain wind speed range or turbulence intensity, which is not available in the measured data, is to be simulated, a user defined model is often used. This makes it possible to simulate a wind speed sequence with the desired characteristics, by setting the corresponding parameters to the appropriate values [4]. In the simulation of wind power in an electrical power system, it is often assumed that the wind speed is made up by the sum of the following four components [4], [5]:

a) the average value;

b) ramp component, representing a steady increase in wind speed;

c) gust component, representing a gust; and

d) turbulence component, representing fast variation.

This leads to the following equation,

$$v_w(t) = v_{wa}(t) + v_{wr}(t) + v_{wg}(t) + v_{wt}(t), \tag{3.8}$$

in which v_{wa} is the average value of the wind; v_{wr} is the ramp component; v_{wg} is the *gust* component; and v_{wt} is the turbulence component. The *ramp* component is characterized by three parameters: the amplitude of the wind speed ramp (A_{rm}), the starting time of the wind speed ramp (T_{sr}), and the end time of the wind speed ramp (T_{er}) as

$$v_{wr} = \begin{cases} 0, & for \quad t < T_{sr}; \\ A_{rm} \dfrac{(t - T_{sr})}{(T_{er} - T_{sr})}, & for \quad T_{sr} \le t \le T_{er}; \\ A_{rm}, & for \quad t > T_{er}. \end{cases} \tag{3.9}$$

The *gust* component is characterized by three parameters: the amplitude of the wind speed gust (A_g), the starting time of the wind speed gust (T_{sg}), and the end time of the wind speed gust (T_{eg}). The wind gust is modeled using the following equation,

$$v_{wg} = \begin{cases} 0, & for \quad t < T_{sg}; \\ 0.5 A_g \left[1 - \cos 2\pi \left(\dfrac{t - T_{sg}}{T_{eg} - T_{sg}} \right) \right], & for \quad T_{sg} \le t \le T_{eg}; \\ 0, & for \quad t > T_{eg}. \end{cases} \tag{3.10}$$

Finally, the *turbulence* component of the wind speed is characterized by a power spectral density. Here, the following power spectral density is used

$$P_{Dt}(f_w) = l_w \left[\ln \left(\frac{h}{\varepsilon} \right)^2 \right]^{-1} \left[1 + 1.5 \frac{f_w l}{v_{wa}} \right]^{5/3}, \tag{3.11}$$

which depends upon the tower height (h), turbulence length (l), frequency (f_w), and roughness length (ε) that defines the landscape of the region. A power spectral density can be used to derive information about the amplitude of a signal’s component at a given frequency. Then, a large numbers of sinusoidal, with a random initial phase angle and amplitude calculated from the power spectral density, are added for each time step. Thus, we can generate a time domain signal with a power spectral density that is the sampled equivalent of the original power spectral density.

3.2.2 Wind turbine model

Wind turbine is the medium which convert the aerodynamic energy from the wind into the mechanical energy in the form of blades’ rotation, which is then used to drive a generator that converts this energy into electricity. In comparison to the vertical axis type, the horizontal axis type turbine is more favorable due to their higher energy capturing capacity (due to the greater tower height) with more efficient propellers [6]. Therefore, this dissertation has adopted the horizontal axis wind turbine in the study and the corresponding modeling is presented here.

The steady-state mechanical power (P_{WT}) available at the turbine shaft, can be determined by [4]

$$P_{WT} = 0.5 C_P(\lambda_{tip}, \beta) \rho A_w v_w^3, \tag{3.12}$$

where

$$\left.\begin{aligned} &C_P(\lambda_{tip}, \beta) = c_1 \left(c_2 / \lambda_i - c_3 \beta - c_4 \beta^{c_5} - c_6 \right) \exp(-c_7 / \lambda_i) \\ &\frac{1}{\lambda_i} = \frac{1}{\lambda_{tip} + c_8 \beta} + \frac{c_9}{\beta^3 + 1} \\ &\lambda_{tip} = r_T \omega_r / v_w \end{aligned}\right\}. \tag{3.13}$$

Here, λ_{tip} is the tip speed ratio (TSR), β is the pitch angle of turbine blade, ρ is the air mass density, r_T is the radius of turbine rotor, ω_r is the rotor angular speed, and c_i (i=1,2..7) are the constant parameters. C_P is the power conversion coefficient which varies with λ_{tip} and β. Equation (3.12) shows that P_{WT} is a fraction of the available power at the rotor shaft determined by C_P. The theoretical maximum value of C_P is about 59% as derived by the *Belz law* [1], [4]. For practical cases, it is well below 59%. The plot of C_P vs. λ_{tip} is shown in Fig. 3-3(a). It can be noted that C_P is maximum at the certain value of β (zero degree in this case). In a variable-speed wind turbine, this curve is utilized to set C_P to its maximum value ($C_{P\text{-}max}$) by forcing λ_{tip} to its optimum value (λ_{tip}^{opt}), as long as the power or rotor speed is below its rated value. This, in turn, is made by adjusting the rotor speed to its optimum value (ω_r^{opt}) as,

$$\omega_r^{opt} = \frac{\lambda_{tip}^{opt}}{r_T} v_w. \tag{3.14}$$

Consequently, the mechanical power output from the turbine will be the maximum. The locus of the maximum power over a wide range of v_w is also depicted in P_{WT} vs. ω_r plot in Fig. 3-3(b) by the black-dashed line. This concept is utilized for the maximum power point tracking (MPPT) scheme.

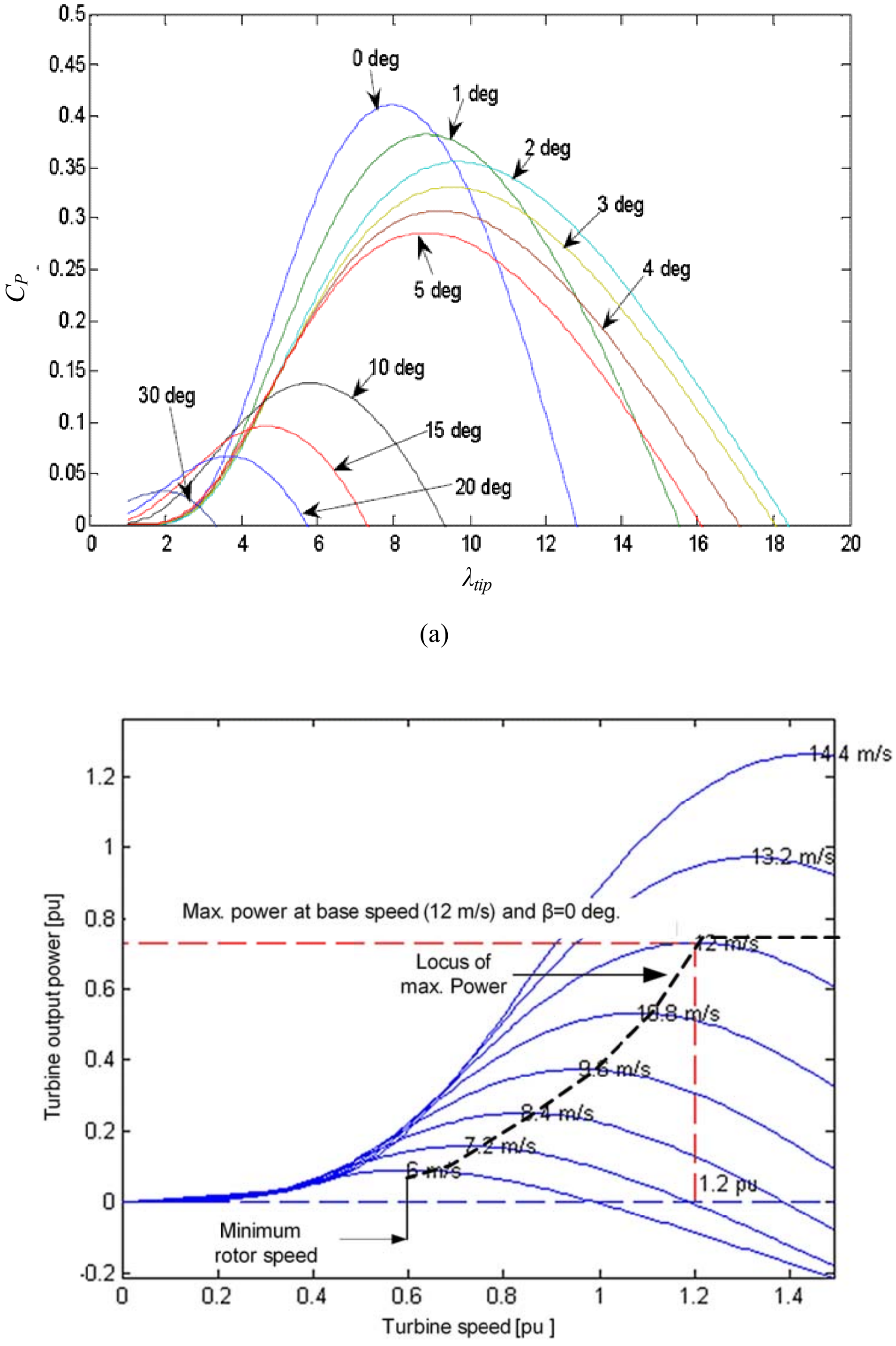

(a)

(b)

Fig. 3-3 Wind turbine characteristic curves. (a) C_P as a function of TSR and (b) power vs. rotor speed characteristics of proposed wind turbine.

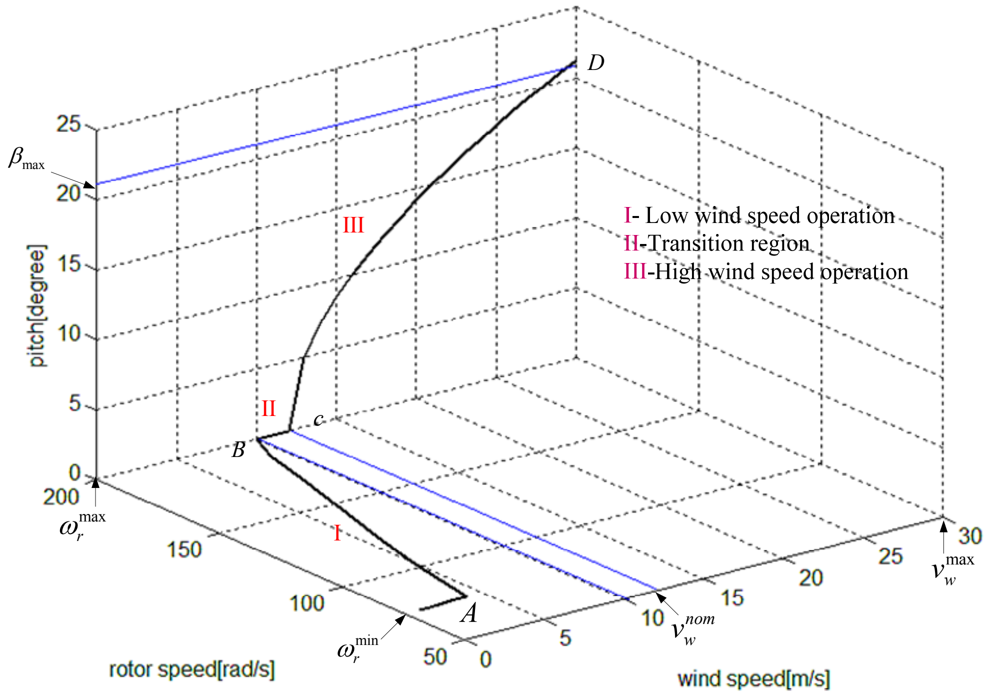

Fig. 3-4 Typical variable speed pitch control strategy plotted on the v_w-ω_r-β space.

For the higher wind speeds, mechanical power output from the turbine becomes greater than its rated value. There are two major ways of performing the aerodynamic power control, a stall control (passive or active) and a pitch control. The s*tall control* implies that the blades are designed to stall in high wind speed and no pitch mechanism is required [7],[8]. The *pitch control* is the most common method of controlling the aerodynamic power generated by the turbine rotor in modern variable-speed wind turbines. In the *pitch control*, the pitch angle is regulated to decrease the angle of attack, i.e. the angle between the chord line of the blade and the relative wind direction so that fraction of aerodynamic power spills away from the turbine fans. Fig. 3-4 illustrates a typical variable speed pitch control strategy plotted on the v_w-ω_r-β space. For the wind speed between 4 m/s to 10 m/s (region I), ω_r^{opt} is set according to (3.14); for the speed between 10 m/s to 12 m/s (region II), it is transition of low to high speed region; and for the speed greater than 12 m/s, the rotor speed is regulated at its rated value by utilizing the pitch angle regulation. An alternative treatment of power capture vs. wind speed is illustrated in Fig. 3-5 which indicates the different operating regions. Below 4 m/s, there is no power generation; for $4 \le v_w \le 12$ m/s, there is maximized generation by keeping C_P to $C_{P\text{-}max}$; for

$12 \le v_w \le 25$ m/s, there is constant generation through the pitch regulation; and above 25 m/s, wind turbine is shut down to protect it from storm.

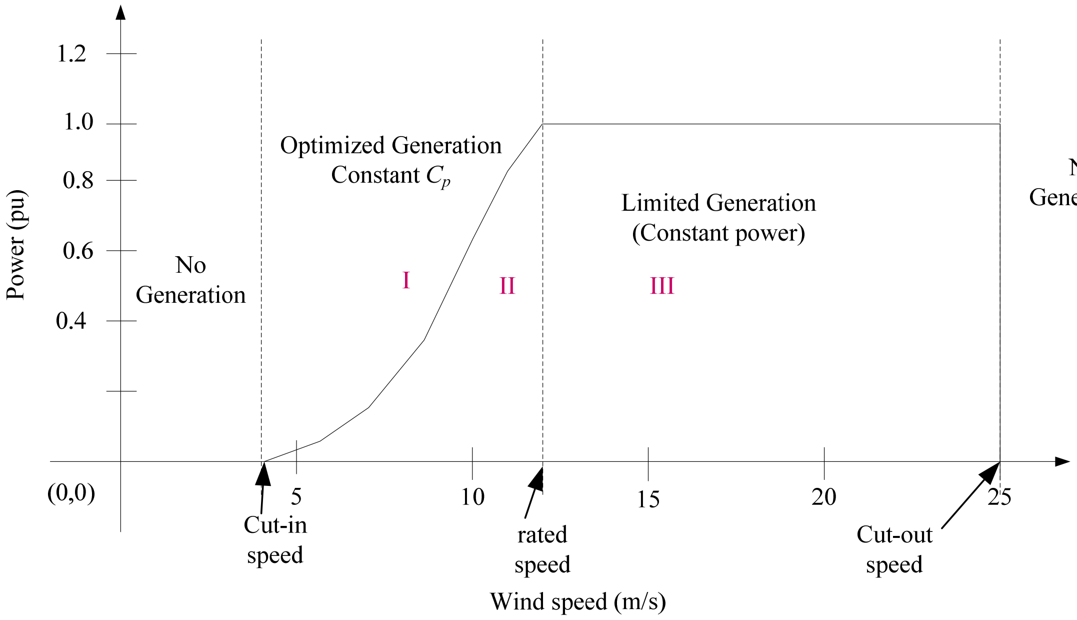

Fig. 3-5 Variable speed pitch controlled wind turbine operation regions.

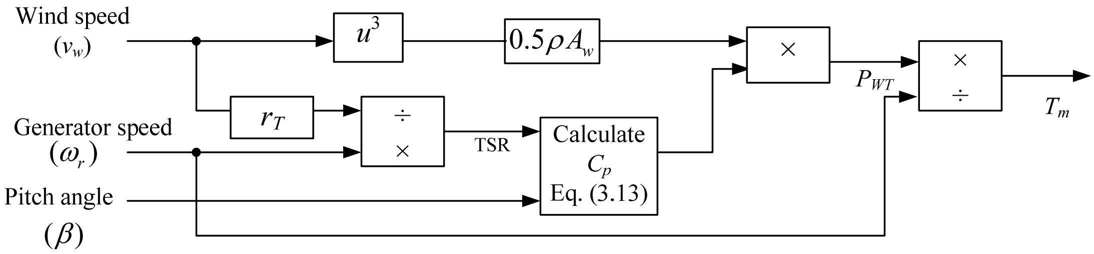

Fig. 3-6 Simulation model for wind turbine.

Fig. 3-6 illustrates the simulation model of the wind turbine developed for this study, in which the inputs are: wind speed, air density, radius of the wind turbine, mechanical speed of the rotor referred to the wind turbine side and the pitch angle. The output is the torque (T_m) which drives the electrical generator. The wind turbine calculates the TSR from the input values and estimates the value of the power coefficient from the performance curves. Here, inputs ω_r and β are the controlled inputs, in which ω_r is regulated by speed controller and the pitch angle controller maintains the value of the blade pitch at the optimum value until the power output of the wind turbine equals the rated power.

3.2.3 Doubly-fed induction generator model

A schematic diagram of a DFIG system with a back-to-back converter is shown in Fig. 3-7. The back-to-back converter consists of two converters: a rotor-side converter (VSC1) and a line-side converter (VSC2) connected back-to-back. Between the two converters, a dc-link capacitor is placed as energy storage to suppress the voltage variations in the dc-link bus. At this bus, other energy storage devices can be augmented for power and energy management. With the converter VSC1, it is possible to control the torque or the rotor speed and the power factor of the stator terminals; while the objectives of the converter VSC2 vary depending upon the operational modes. It is notable that in a DFIG, the power flow direction through the rotor is negative or positive depending upon the wind speed. For positive slip (lower wind speeds), the rotor draw power from the coupling bus; at zero slip, there is no power transfer from the rotor circuit; and at negative slip (higher wind speeds), the rotor also supplies power to the coupling bus (see Table 3.1). In following subsections, the detailed model of each component of the DFIG is presented.

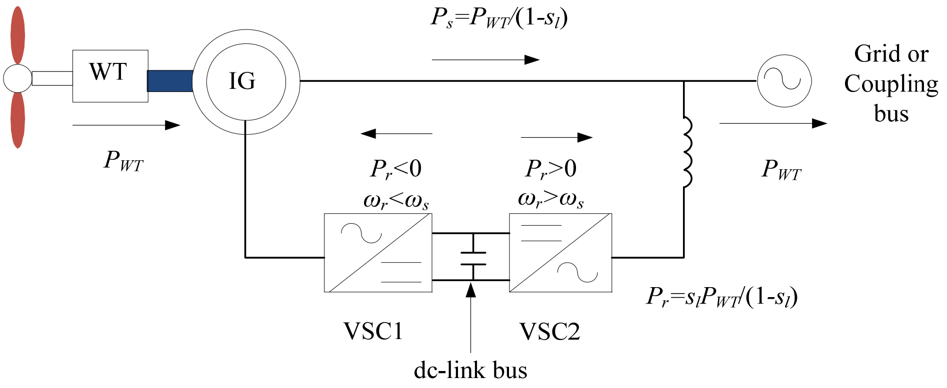

Fig. 3-7 Schematic diagram of a typical "loss-less" DFIG. It shows the power flow components through stator (P_s) and rotor circuit (P_r) as a function of slip (s_l).

Table 3.1 Example of the power flow for different slips of a DFIG system.

Slip, s_l	Rotor speed, ω_r [pu]	Rotor power, P_r	Stator power, P_s
0.3	0.7	-0.43 P_{WT}	1.43 P_{WT}
0	1	0	P_{WT}
-0.3	1.3	0.23. P_{WT}	0.77 P_{WT}

a) Machine model

The induction machine considered here has a three-phase stator and a wound rotor in which the terminal of the rotor windings are accessible from the slip rings. During the modeling, we adopt the classical assumptions; such as linearity of the materials (no saturation), sinusoidal distribution of the field in the air-gap, core losses are negligible, changes in resistance due to heating are negligible, and a balanced structure. Further, the wind turbine generator system assumes the wind turbine and the DFIG as a lumped unit, represented by their equivalent parameters: the moment of inertia and the damping coefficient. The equivalent circuit of a DFIG in the reference frame rotating at synchronous angular speed (ω_e) is shown in Fig. 3-8 [9],[10]. The expressions of the dynamic equation are given in the space vector form, in which $\boldsymbol{\psi}, \mathbf{i}$, and $\mathbf{v}$ represent space vector for flux, current, and voltage, respectively. The quantities for the rotor side and stator side are denoted respectively by subscripts '*r*' and '*s*'; whereas the quantities transformed to the rotating *d*-axis and *q*-axis are represented by subscripts '*d*' and '*q*', respectively. Thus, we have the general expression

$$\mathbf{x} = x_d + jx_{q,}$$

for $\mathbf{x} = \boldsymbol{\psi}_s, \boldsymbol{\psi}_r, \mathbf{i}_r, \mathbf{i}_s, \mathbf{v}_s, \mathbf{v}_r$; where $x = \psi_s, \psi_r, i_r, i_s, v_s, v_r$ *and* $j = \sqrt{-1}.$

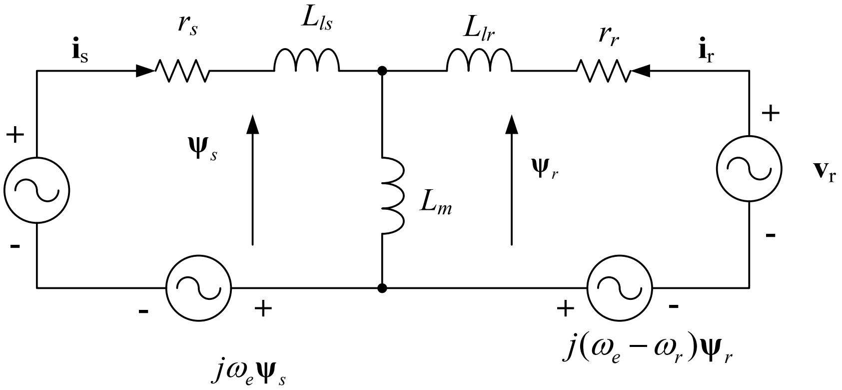

Fig. 3-8 Equivalent circuit for the DFIG in the synchronously rotating reference frame.

The stator and rotor flux state vectors in Fig. 3-8, can be written as

$$\left.\begin{aligned} \boldsymbol{\psi}_s &= L_s\mathbf{i}_s + L_m\mathbf{i}_r \\ \boldsymbol{\psi}_r &= L_m\mathbf{i}_s + L_r\mathbf{i}_r \end{aligned}\right\}, \tag{3.15}$$

where

$$L_s = L_{ls} + L_m, \qquad L_r = L_{lr} + L_m \ . \tag{3.16}$$

Here, L is the inductance; r is the resistance; subscripts s and r are used for denoting the stator or rotor quantity, respectively. Similarly, L_m represents the mutual inductance of the machine. The machine has fifth order dynamic equations, in which the first four are derived by applying the *Kirchhoff's voltage law* and the last from equation of motion, as

$$\left.\begin{aligned} d\boldsymbol{\psi}_s / dt &= \mathbf{v}_s - r_s\mathbf{i}_s - j\omega_e\boldsymbol{\psi}_s \\ d\boldsymbol{\psi}_r / dt &= \mathbf{v}_r - r_r\mathbf{i}_r - j(\omega_e - \omega_r)\boldsymbol{\psi}_r \\ d\omega_r / dt &= (T_m - T_{em}) / J_m + D_m / J_m \end{aligned}\right\}, \tag{3.17}$$

where

$$T_{em} = -0.75 n_p \operatorname{Re}\{\boldsymbol{\psi}_s \mathbf{i}_s^*\}. \tag{3.18}$$

Here, T_{em} is the electromagnetic torque, ω_r is the rotor angular speed, J_m is the combined moment of inertia of the turbine and the generator mass, and n_p is the number of pole pairs. Similarly, the expression of active (P_{ig}) and reactive power (Q_{ig}) is evaluated as

$$\left.\begin{aligned} P_{ig} &= 3\operatorname{Re}[\mathbf{v}_s\mathbf{i}_s^*]/2 \\ Q_{ig} &= -3\operatorname{Im}[\mathbf{v}_s\mathbf{i}_s^*]/2 \end{aligned}\right\}. \tag{3.19}$$

In the case of cage induction generators, the expressions (3.15) to (3.19) would be the same, except that the value of rotor voltage vector in (3.17) is zero. For the purpose of analysis, the equivalent stator magnetizing current vector ($\mathbf{i}_{mo}$) is defined so that

$$\boldsymbol{\psi}_s = L_s\mathbf{i}_s + L_m\mathbf{i}_r = L_m\mathbf{i}_{mo}. \tag{3.20}$$

That gives,

$$\left.\begin{aligned} \mathbf{i}_{mo} &= L_s\mathbf{i}_s / L_m + \mathbf{i}_r \\ \mathbf{i}_s &= L_m(\mathbf{i}_{mo} - \mathbf{i}_r) / L_s \end{aligned}\right\}. \tag{3.21}$$

Further, from (3.15) and (3.21), we have

$$\boldsymbol{\psi}_s = L_m^2\mathbf{i}_{mo} / L_s + \sigma L_r\mathbf{i}_r \tag{3.22}$$

where $\sigma = 1 - L_m^2 / L_s L_r$. Substituting $\boldsymbol{\psi}_s$ in (3.20), $\mathbf{i}_s$ in (3.21) and $\boldsymbol{\psi}_r$ in (3.15) into (3.17), yields the stator and rotor voltages in the synchronous *d-q* reference frame as

$$\left.\begin{aligned} \mathbf{v}_s &= r_s\mathbf{i}_s + L_m d\mathbf{i}_{mo} / dt + j\omega_e\boldsymbol{\psi}_s \\ \mathbf{v}_r &= r_r\mathbf{i}_r + \sigma L_r d\mathbf{i}_r / dt + (L_m^2 / L_s) d\mathbf{i}_{mo} / dt + j(\omega_e - \omega_r)\boldsymbol{\psi}_r \end{aligned}\right\}. \tag{3.23}$$

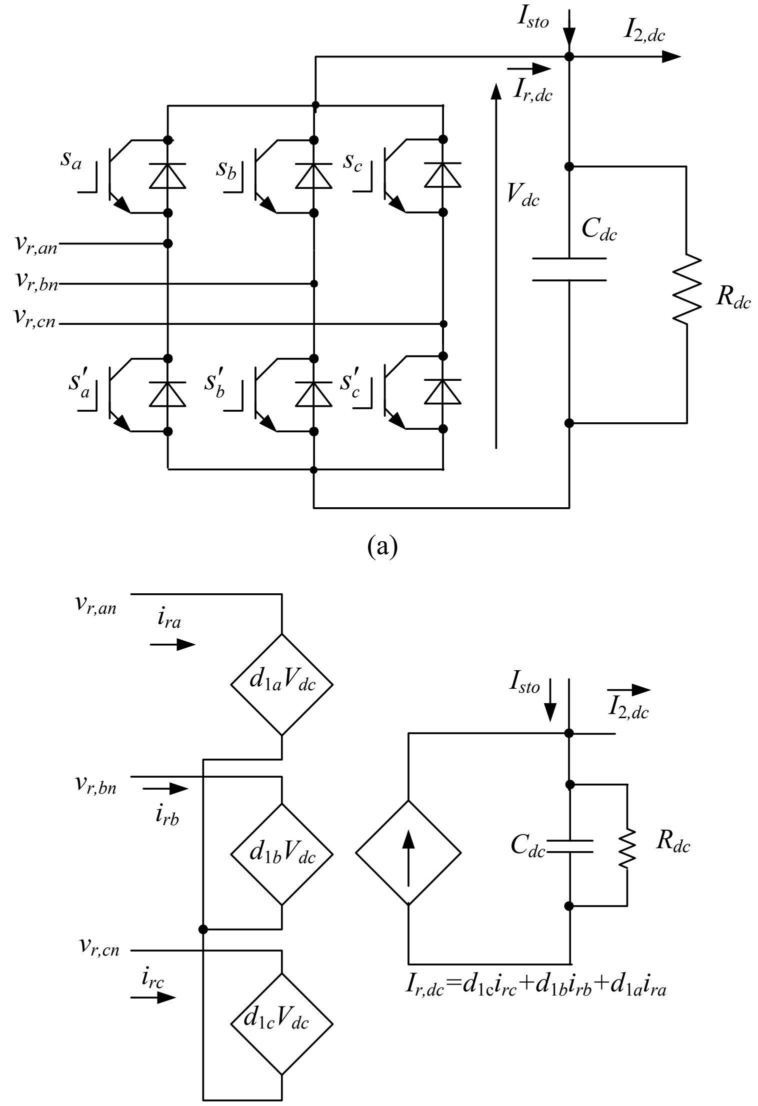

(a)

(b)

Fig. 3-9 Models for voltage source converter. (a) Switching model, and (b) averaged model. The notation “′” with the switching function represents the complimentary value, such that $s_i + s'_i = 1\ (i = a, b, c)$. Here, $I_{r,dc}$, I_{sto} and $I_{2,dc}$ represent the dc current injected from VSC1, from the storage system and from VSC2, respectively.

b) Rotor-side converter model

The model of voltage source converter consists of 3-phase transistor switching circuits operated through the PWM principle as detailed in Fig. 3-9(a). The relationship between the switching functions (s_a,s_b and s_c), and the terminal ac and dc voltages can be written as [11],[12]

$$\begin{bmatrix} v_{r,an} \\ v_{r,bn} \\ v_{r,cn} \end{bmatrix} = \frac{V_{dc}}{3} \begin{bmatrix} 2 & -1 & -1 \\ -1 & 2 & -1 \\ -1 & -1 & 2 \end{bmatrix} \begin{bmatrix} s_a \\ s_b \\ s_c \end{bmatrix}, \tag{3.24}$$

where V_{dc} is the dc link voltage, $v_{r,in}$ and s_i (i=a,b,c) represents the i^{th} phase to neutral point rotor voltage and switching function of the i^{th} switch, respectively. The complexity of a converter model increases with the desired level of accuracy. While certain applications demand the most precise model available, other application are satisfactory with a simplified averaged model. In case of a large system having many converters, the exact model is not feasible due to complexity of analysis and constraints of simulation time and data storage. In such cases, the fundamental frequency model is sufficient assuming that the high-frequency harmonics produced by the inverter as a result of the PWM control techniques are mostly filtered by a sinusoidal line filter. Therefore, the averaged modeling approach is utilized in this study to manage the simulation time and storage requirements. This makes the ac side of VSC1 a sinusoidal voltage source and dc side a current source, as represented by the following equations [13]

$$\left.\begin{aligned} [v_{r,an} \quad v_{r,bn} \quad v_{r,cn}]^t &= [d_{1a} \quad d_{1b} \quad d_{1c}]^t V_{dc} \\ I_{r,dc} &= [i_{r,an} \quad i_{r,bn} \quad i_{r,cn}][d_{1a} \quad d_{1b} \quad d_{1c}]^t \end{aligned}\right\} \tag{3.25}$$

where,

$$[d_{1a} \quad d_{1b} \quad d_{1c}]^t \approx \frac{1}{T_{sw}} \int_0^{T_{sw}} \begin{bmatrix} 2 & -1 & -1 \\ -1 & 2 & -1 \\ -1 & -1 & 2 \end{bmatrix} \begin{bmatrix} s_a \\ s_b \\ s_c \end{bmatrix} dt,$$

and i_{ri} (i=a,b,c) represents the i^{th} phase current from the rotor circuit. Fig. 3-9 (b) shows the schematic diagram of the averaged model. Noting that $\mathbf{d}_1 = d_{1d} + jd_{1q}$, the expression of rotor voltage dynamics can be written as

$$\mathbf{d}_1 V_{dc} = r_r \mathbf{i}_r + \sigma L_r d\mathbf{i}_r / dt + (L_m^2 / L_s) d\mathbf{i}_{mo} / dt + j(\omega_e - \omega_r)\boldsymbol{\psi}_r. \tag{3.26}$$

This equation, together with (3.15) to (3.22), are used to develop the control scheme of VSC1 discussed in the next chapter.

c) Line-side converter, filter and ac bus

Applying the same treatment as with VSC1, the time averaged fundamental frequency model of VSC2, the line filter and the grid voltage can be expressed by the following set of second order dynamic equations,

$$\left.\begin{aligned}
&\mathbf{e}_2 = R_f\mathbf{i}_2 + L_f d\mathbf{i}_2 / dt - j\omega_e\mathbf{i}_2 L_f + \mathbf{v}_2\\
&\mathbf{v}_2 = R_{th}\mathbf{i}_2 + L_{th}d\mathbf{i}_2 / dt + \mathbf{v}_{th}\\
&\mathbf{e}_2 = \mathbf{d}_2\, V_{dc}\\
&\mathbf{d}_2 = d_{2d} + jd_{2q}
\end{aligned}\right\},\tag{3.27}$$

with $\mathbf{e}_2 = e_d + je_q, \mathbf{d}_2 = d_{2d} + jd_{2q}, \mathbf{i}_2 = i_{2d} + ji_{2q}, \mathbf{v}_2 = v_{2d} + jv_{2q}$ and $\mathbf{v}_{th} = v_{thd} + jv_{thq}$.

Here, $\mathbf{d}_2, \mathbf{e}_2, \mathbf{v}_2, \mathbf{i}_2,$ and $\mathbf{v}_{th}$ represents vector quantities for the duty cycle vector of VSC2, the inverter terminal voltage, the voltage at bus #2, the current injected to bus #2, and the *Thevenin's voltage* of outer power network seen from bus #2, respectively. Similarly, $R_{f,}\ L_f, R_{th}$ and L_{th} are the interfacing resistance and interfacing inductance, the *Thevenin* resistance of external network and *Thevenin* inductance of the external network, respectively (see Fig. 2-6 (a)). This equation will be used to develop the control scheme for VSC2.

d) dc-link voltage

Considering the power conservation principle in the proposed VSC1 model, we have

$$\left.\begin{aligned}
&1.5(i_{rd}v_{rd} + i_{rq}v_{rq}) = I_{r,dc}V_{dc}\\
&1.5(i_{2d}v_{2d} + i_{2q}v_{2q}) = I_{2,dc}V_{dc}
\end{aligned}\right\}.\tag{3.28}$$

Applying, KCL at the dc link node, we get

$$C_{dc}\frac{dV_{dc}}{dt} = I_{r,dc} + I_{sto} - I_{2,dc} - \frac{V_{dc}}{R_{dc}}.\tag{3.29}$$

The variables and the parameters in above equations are defined in Fig. 3-9.

e) Summary of doubly-fed induction generator model

From the discussion in section 3.2.3, the dynamic model of DFIG can be summarized by the following set of equations.

$$\left.\begin{aligned}
&L_m\frac{d\mathbf{i}_{mo}}{dt}=\mathbf{v}_s-r_s\mathbf{i}_s-j\omega_e\boldsymbol{\psi}_s\\
&\sigma L_r\frac{d\mathbf{i}_r}{dt}=\mathbf{v}_r-r_r\mathbf{i}_r-\frac{L_m}{L_s}(\mathbf{v}_s-r_s\mathbf{i}_s-j\omega_e\boldsymbol{\psi}_s)-j(\omega_e-\omega_r)\boldsymbol{\psi}_r\\
&J_m\frac{d\omega_r}{dt}=(T_m-T_{em})-D_m\omega_r L_f\\
&C_{dc}\frac{dV_{dc}}{dt}=I_{r,dc}+I_{sto}-I_{1,dc}-\frac{V_{dc}}{r_c}\\
&\frac{d\mathbf{i}_2}{dt}=\mathbf{e}_2-r_f\mathbf{i}_2+j\omega_e\mathbf{i}_2-\mathbf{v}_2
\end{aligned}\right\}\tag{3.30}$$

where,

$$\left.\begin{aligned}
&\boldsymbol{\psi}_s=L_m^2\mathbf{i}_{mo}/L_s+\sigma L_r\mathbf{i}_r\\
&\boldsymbol{\psi}_r=L_m\mathbf{i}_s+L_r\mathbf{i}_r\\
&\mathbf{i}_s=L_m(\mathbf{i}_{mo}-\mathbf{i}_r)/L_s\\
&i_{r,dc}=1.5(i_{rd}V_{rd}+i_{rq}V_{rq})/V_{dc}\\
&i_{1,dc}=1.5(i_{2d}V_{1d}+i_{2q}v_{2q})/V_{dc}\\
&T_{em}=-0.75n_p\,\mathrm{Re}\{\boldsymbol{\psi}_s\mathbf{i}_s^*\}\\
&T_m=0.5C_P(\lambda_{tip},\beta)\rho A r_T^3\omega_r^2
\end{aligned}\right\}.\tag{3.31}$$

3.2.4 Model analysis

a) Voltage source converter

To test the model of the voltage source converter, the ac terminal of the VSC is connected to the 0.8 pu resistive load through filter, and 750V dc source is connected to the dc side. The PWM technique is employed for the switching of the transister/diode model built-up in MATLAB/Simpower toolbox. Likewise, the switching model is replaced by the average model of VSC with the identical value of filter impedances. Fig. 3-10(a) illustrates the current and the voltage response against the load with the switching model and Fig. 3-10(b) depicts those of the averaged model. It is noted that though there are harmonics in voltage and current from the switched model, its output voltage and current waveform are close to those of the averaged model when a properly designed filter is applied to the system. Nevertheless, the averaged model is capable of simulating a VSC with good accuracy for large time scale simulation and analysis purposes.

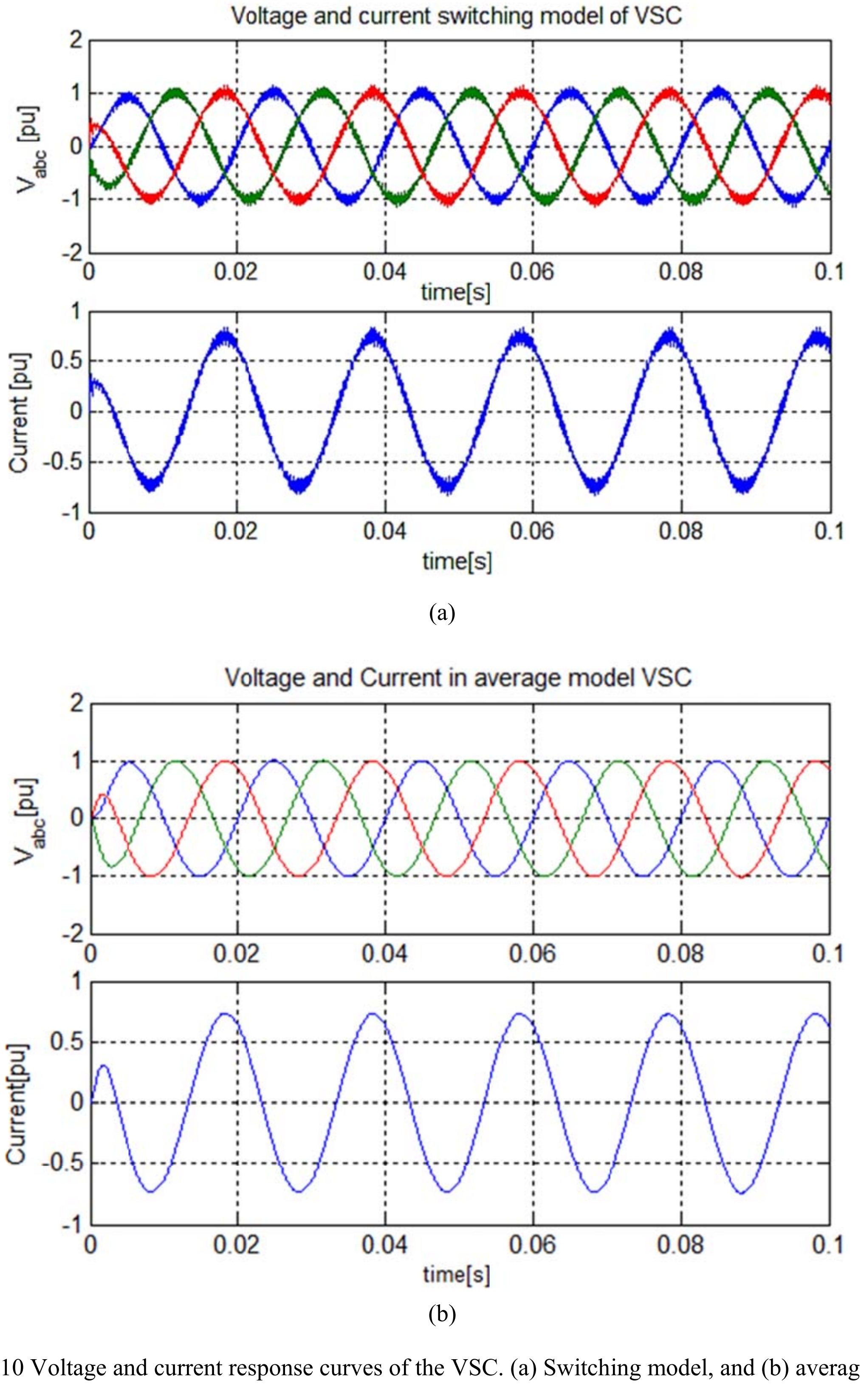

(a)

(b)

Fig. 3-10 Voltage and current response curves of the VSC. (a) Switching model, and (b) averaged model

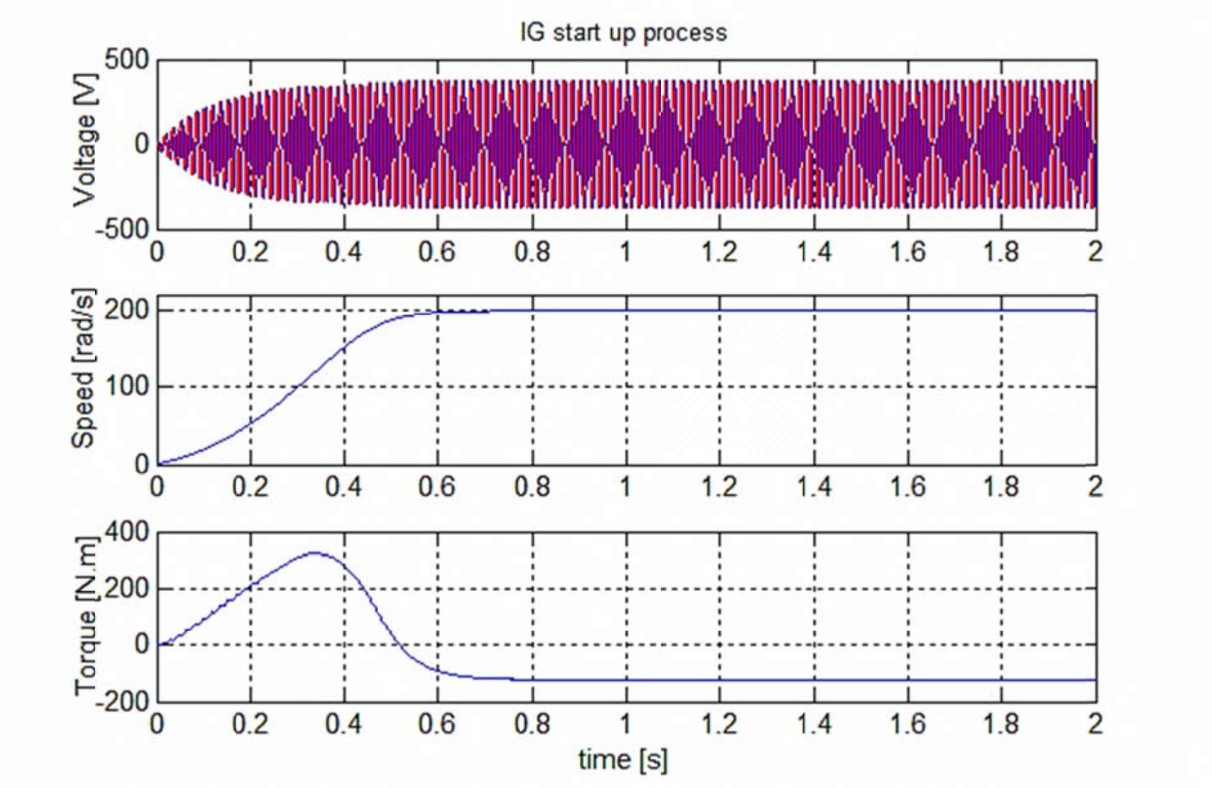

Fig. 3-11 DFIG startup process at no-load.

b) Doubly-fed induction generator

For the analysis process, the induction generator (IG) is configured with parameters given in the appendix; the rotor is connected to dc bus via an ideal inverter; and then the voltage build up process is observed at the stator terminal with no-load condition. Fig. 3-11 shows the ac voltage and the speed build-up process. Initially, the machine draws large power from the dc source and it starts as a motor. After a short transient, it reaches to the steady-state condition, at which the rotor speed and the ac voltage settle at their rated values because the electrical torque equals to the mechanical counterpart. These results are similar to those obtained from the dynamic model of the IG reported in the standard texts [10].

3.3 Dedicated Energy Storage System

As seen in the previous chapter, the storage system consists of the FC/ELZ and UC units; in which not only the electrochemical phenomena, but also the other process, such as thermal, chemical, fluid dynamic, etc., are also present. If all these phenomena should be taken into account at a time, the modeling process would be too complex and time consuming. When applying the modeling in engineering processes, different approaches can be considered, depending on the purpose of the study. For example, fluid dynamic, thermal, chemical and electrochemical approaches may suitable for the development stage of electrochemical system, especially for the wider time frame analysis. But for the application stage, in which the electrochemical system has to interact with the load to which it is connected, an electric modeling of the system could be more desirable. Therefore, in this chapter, we will focus on those models more suitable to effective integration in simulation tools of electrical network.

3.3.1 Fuel cell

An SOFC cell consists of *yttria-stabilized zirconia* electrolyte, onto which a porous cathode (lanthanum manganite) and a porous anode (Ni/ZrO_2-cermet) are deposited (see Fig. 3-12). At the cathode-electrolyte interface, oxygen molecules accept electrons coming from the external circuit to form oxide ions; the electrolyte layer allows only oxide ions to pass through; and at the anode-electrolyte interface, hydrogen molecules react with oxide ions to form steam and electrons get released. These electrons pass through the external circuit and reach the cathode–electrolyte layer, and thus the circuit is closed [14]. These FCs are characterized by their electrolyte material, the solid oxide or ceramic electrolyte. There are various models of SOFC depending upon the scope of interest. Some are the highly theoretical and are based on empirical equations [15],[16], and other are more application oriented [17]. This study utilizes the detailed dynamic model which considers the diffusion phenomena of reactant gases and the double layer charging effect [14],[18]. The assumptions in modeling are as follows.

- One-dimensional treatment of reactants flow.
- H_2 is directly available from the tank, so fuel combustion is not included.
- Large stoichiometric quantity of H_2 at anode and O_2 at cathode.
- The combustion zone is not included in the SOFC thermal model. The fuel and air are assumed to be pre-heated.
- The gases are ideal.
- Parameters for individual cells can be lumped together to represent a fuel cell stack.

In the following paragraphs modeling of different components of the fuel cell is presented.

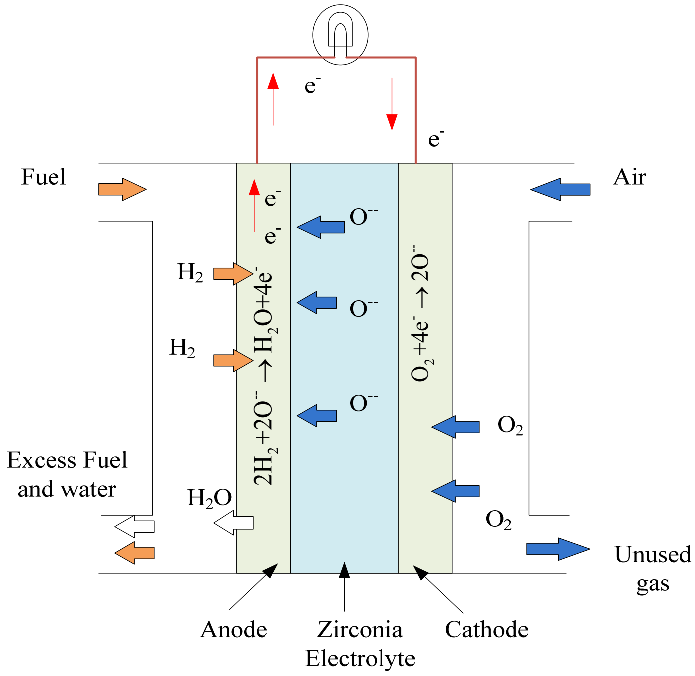

Fig. 3-12 Schematic diagram of SOFC.

a) Partial pressure dynamics

Partial pressures of H_2, H_2O and O_2 at anode and cathode channels are deducted in terms of the fuel cell operating parameters (e.g., fuel cell temperature, fuel and oxidant flow rates) by using material conservation equations. The resultant partial pressure values are, then, used to calculate the fuel cell output voltage.

The dynamics of the partial pressures of hydrogen and water vapor in the anode gas flow channel can be determined through the ideal gas equations as follows [18],[19].

$$\left.\begin{aligned} \frac{U_a}{RT_{fc}}\frac{d}{dt}p_{H_2} &= M_{H_2}^{in} - M_{H_2}^{out} - \frac{I_{fc}}{2F} \\ \frac{U_a}{RT_{fc}}\frac{d}{dt}p_{H_2O} &= M_{H_2O}^{in} - M_{H_2O}^{out} + \frac{I_{fc}}{2F} \\ \frac{U_c}{RT_{fc}}\frac{d}{dt}p_{O_2} &= M_{O_2}^{in} - M_{O_2}^{out} - \frac{I_{fc}}{4F} \end{aligned}\right\}, \qquad (3.32)$$

where the U_a and U_c are the volume of the anode and cathode side, respectively; p_i is the partial pressure of the i^{th} species (i=H_2, H_2O, O_2); M_i is the mass flow rate of i^{th} species; F is the *Faraday* constant; I_{fc} is fuel cell current; and R is the gas constant.

The values of inlet and outlet molar flows of the gases in (3.32) are given by,

$$\left.\begin{aligned}
M_{H_2}^{in} &= M_a x_{H_2}^{in} = M_a \frac{p_{H_2}^{in}}{P_a} \\
M_{H_2}^{out} &= M_a x_{H_2}^{out} = M_a \frac{p_{H_2}^{out}}{P_a} \\
M_{H_2O}^{in} &= M_a x_{H_2O}^{in} = M_a \frac{p_{H_2O}^{in}}{P_a} \\
M_{H_2O}^{out} &= M_a x_{H_2O}^{out} = M_a \frac{p_{H_2O}^{out}}{P_a} \\
M_{O_2}^{in} &= M_c x_{O_2}^{in} = M_c \frac{p_{O_2}^{in}}{P_c} \\
M_{O_2}^{out} &= M_c x_{O_2}^{out} = M_c \frac{p_{O_2}^{out}}{P_c}
\end{aligned}\right\}. \tag{3.33}$$

Here, M_a and M_c represent the total molar concentration at the anode and cathode, respectively, and x represents the fraction of flow quantity as specified by the subscripts. As a result, molar inflow (outflow) rate becomes proportional to the ratio of inflow (outflow) partial pressure and net gas pressure inside the electrodes. Assuming that the partial pressure of the species in the electrodes as an average of input and output pressures, i.e., $p_{H_2} = (p_{H_2}^{in} + p_{H_2}^{out})/2$, (3.32) can be rewritten as

$$\left.\begin{aligned}
\frac{d}{dt} p_{H_2} &= \frac{2RT_{fc}}{U_a} M_{H_2}^{in} - \frac{2M_a RT_{fc}}{P_a U_a} p_{H_2} - \frac{RT_{fc}}{2FU_a} I_{fc} \\
\frac{d}{dt} p_{H_2O} &= \frac{2RT_{fc}}{U_a} M_{H_2O}^{in} - \frac{2M_a RT_{fc}}{P_a U_a} p_{H_2O} + \frac{RT_{fc}}{2FU_a} I_{fc} \\
\frac{d}{dt} p_{O_2} &= \frac{2RT_{fc}}{U_c} M_{O_2}^{in} - \frac{2M_c RT_{fc}}{P_c U_c} p_{O_2} - \frac{RT_{fc}}{4FU_c} I_{fc}
\end{aligned}\right\}. \tag{3.34}$$

Note that the dynamic equation has effective time constants, $\tau_a = U_a P_a / 2M_a RT_{fc}$ and $\tau_c = U_c P_c / 2M_c RT_{fc}$. They are variable quantities that depend on the molar flow rates of the species at the anode or cathode.

b) Fuel cell output voltage

At the cathode, oxygen from air is converted to oxygen ions which move through the electrolyte membrane and reacts with the fuel at the anode-electrolyte interface, this process results the open circuit potential due to change in the *Gibbs energy*. The phenomenon of generation of electro-chemical potential of an SOFC is shown in Fig. 3-12. The chemical reaction taking place at the electrodes is written as,

$$\left.\begin{array}{l} Anode: \mathrm{H_2{+}O^{2-} \rightarrow H_2O{+}2e^-} \\ Cathode: \tfrac{1}{2}\mathrm{O_2{+}2e^- \rightarrow O^{2-}} \end{array}\right\}.$$

Based upon the chemical reactions at the cathode and the anode, the voltage generated in a cell (E_{cell}) can be written by the *Nernst equation* as [18], [20]

$$E_{cell} = E_{0,cell} - k_E(T_{fc} - 298) + \frac{RT_{fc}}{2F}\ln\left\{\frac{p_{H_2}\sqrt{p_{O_2}}}{p_{H_2O}}\right\}, \tag{3.35}$$

where $E_{0,cell}$ and k_E represents the *Gibbs potential* and empirical constant, respectively. E_{cell} calculated from (3.35) is the open-circuit voltage of the fuel cell. However, when the fuel cell is under a loading condition, the output voltage is less than E_{cell} due to activation loss, ohmic voltage drop and concentration over-potential. Consequently, the output voltage of a cell can be written as

$$V_{cell} = E_{cell} - V_{act,cell} - V_{ohm,cell} - V_{con,cell}, \tag{3.36}$$

where $V_{act,cell}, V_{ohm,cell}$ and $V_{con,cell}$ denote *activation voltage drop*, *ohmic voltage drop* and *concentration voltage drop*, respectively. Finally, the net output voltage (V_{fc}) and power flow (P_{fc}) from the fuel cell stack can be obtained as,

$$V_{fc} = N_{cell}V_{cell}, \qquad P_{fc} = V_{fc}I_{fc}, \tag{3.37}$$

where N_{cell} is the total number of cell in a stack. The voltage drop terms in (3.36) is determined as follows.

i) Activation Voltage Drop

Activation voltage loss represents an activation energy barrier that must be overcome before the chemical reaction occurs. During the process, a proportion of the voltage generated is lost in driving the chemical reaction that transfers the electrons to or from the electrode. A general equation for activation loss, for all working value of current, can be deduced from *Butler–Volmer equation* as [20],

$$V_{act,cell} = \frac{2RT_{fc}}{zF}\sinh^{-1}\left(I_{fc}/2i_0\right), \quad i_o = a_c e^{-(b_c/RT_{fc})}, \tag{3.38}$$

where a_c and b_c are the empirical parameters, and z is the number of electrons participating in the reaction. The current density i_0 is known as the *exchange current density,* which depends on the temperature. According to (3.38), the activation voltage drop will be zero when the load current is zero. The *ohmic* and *concentration voltage drops* (to be discussed in the following subsections) are also zero when the fuel cell is not loaded (I_{fc}=0). However, even the open-circuit voltage of an SOFC is known to be less than the theoretical value given by (3.35) [13]. To include the effect of no-load activation voltage drop, a constant and a temperature-dependent term can also be added to (3.38) [17]

$$V_{act,cell} = \underbrace{\kappa_0 + \kappa_1 T_{fc}}_{V_{act0,cell}} + \underbrace{\frac{2RT_{fc}}{zF}\sinh^{-1}\left(I_{fc}/2i_0\right)}_{V_{act1,cell}}, \tag{3.39}$$

where κ_0 is the constant term of the activation voltage drop and κ_1 is the temperature coefficient of the activation voltage drop. In the above expression, $V_{act0,cell}$ is the part of activation drop affected only by the fuel cell internal temperature, while $V_{act1,cell}$ depends both on current and temperature.

ii) Concentration loss

This results from the change in concentration of the reactants at the surface of the electrodes when the fuel is used. Since the concentration affects the voltage, this type of irreversibility is sometimes called *concentration loss* or *mass transport loss.* The expression for the concentration loss is derived by [14]

$$V_{con,cell} = -\frac{RT_{fc}}{zF}\ln(1 - I_{fc}/I_{limit}). \tag{3.40}$$

Here, I_{limit} is the *limiting current density* at which the fuel is consumed at the maximum supply rate. The current density cannot rise above this value, because the fuel gas cannot be supplied at a greater rate. At this current density the pressure would have just reached zero.

iii) Ohmic voltage drop

The *ohmic voltage drop* results from the resistance to the electrons in the interconnection of collecting plates and carbon electrodes, and the resistance to the oxygen ions in solid membrane. The total voltage drop due to resistive effect can be represented as [18], [21]

$$V_{ohm,cell} = V_{ohm,elecyt} + V_{ohm,interc} = I_{fc}R_{ohm,cell}, \tag{3.41}$$

where $V_{ohm,elecyt}$ is the voltage drop in electrolyte medium, $V_{ohm,interc}$ is the voltage drop in interconnection, and R_{ohm} is the equivalent resistance of the fuel cell. The resistance, R_{ohm} normally decreases as temperature increases. It can be expressed as

$$R_{ohm,cell} = \frac{\alpha_{elecyt} e^{(b_{elecyt}/T_{fc})}}{A_{cell}} \delta_{elecyt} + \frac{\alpha_{interc} e^{(b_{interc}/T_{fc})}}{A_{cell}} \delta_{interc}, \tag{3.42}$$

where α_is and b_is (i=*elecyt, interc*) are the constant parameters, δ_is are the resistivity of the material, and A_{cell} is the cross-section area of the fuel cell.

iv) Double layer effect

The phenomenon known as charge double layer exists in an SOFC because two electrodes are separated by the electrolyte (see Fig. 3-12) and two boundary layers are formed (anode-electrolyte layer and electrolyte-cathode layer). The charge layer acts as the storage of electrical charge behaving like an electrical capacitor. This causes a first order delay in charging and discharging. Such delay affects the activation and concentration potentials. However, the ohmic over-potential is not affected, since it is related linearly to the cell current through Ohm's law. The model for the SOFC considering this effect can be described by the equivalent circuit shown in Fig. 3-13.

The parameters $R_{ohm,cell}$, $R_{act,cell}$ and $R_{conc,cell}$ in the figure are equivalent resistances of *ohmic voltage drop, activation* and *concentration voltage drops*, which can be calculated according to (3.42), (3.38) and (3.40), respectively. C_{fc} represents the equivalent capacitance of the double-layer charging effect. Since the electrodes of the SOFC are porous, the value of C_{fc} is large and can be in the order of several farad [14]. The voltage across C_{fc} can be expressed as

$$V_{dl} = \left(I_{fc} - C_{fc} dV_{dl} / dt\right)(R_{act,cell} + R_{con,cell}). \tag{3.43}$$

Based upon the aforementioned discussion, the *V-I* curve for the SOFC stack is presented in Fig. 3-14 depicting the three regions. Voltage drop across the FC associated with low currents is due to the *activation loss* inside the SOFC, voltage drop in the middle of the curve (approximately linear) is due to the *ohmic loss* in the FC stack, and voltage drop at the end of the curve is due to the *concentration loss*.

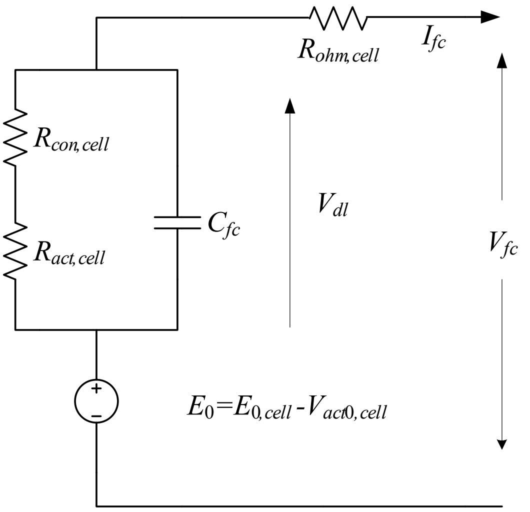

Fig. 3-13 Equivalent electrical model of SOFC. The term $V_{act0,cell}$ is part of $V_{act,cell}$ which is affected only by the fuel cell internal temperature (not by current so is added with $E_{0,cell}$).

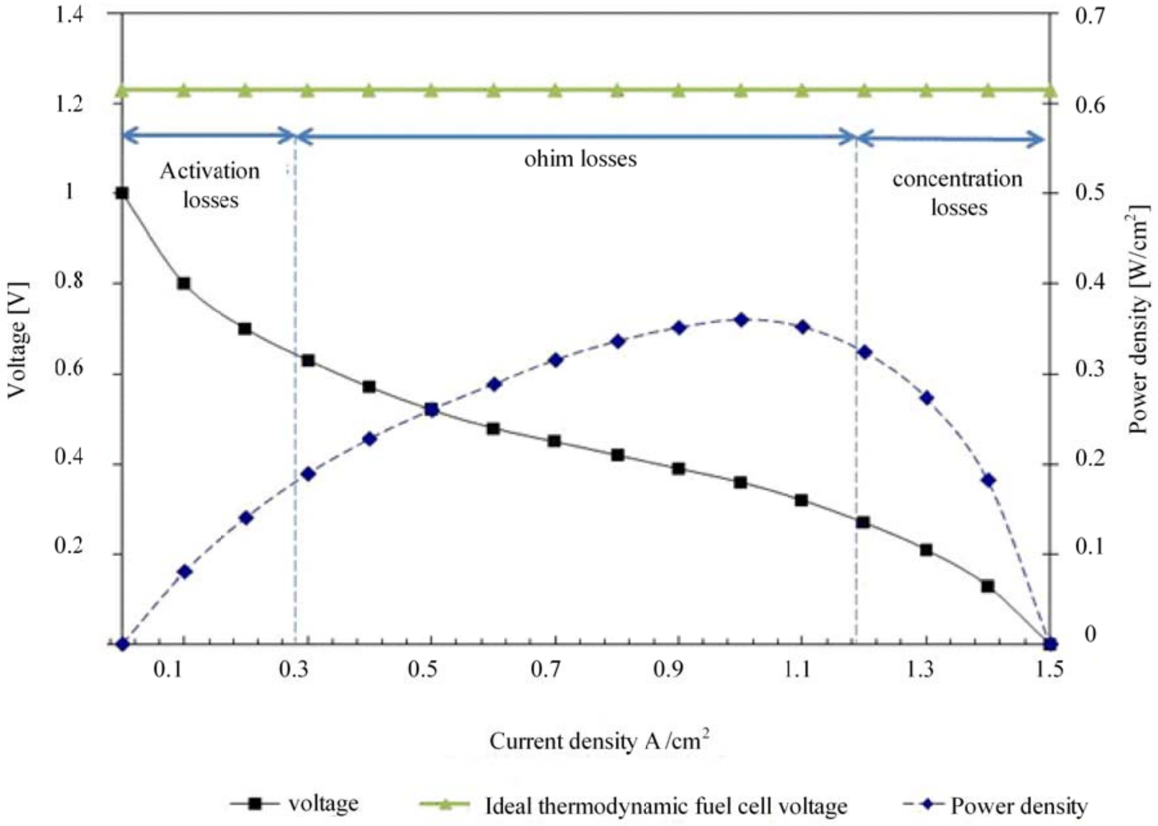

Fig. 3-14 Static *V-I and P-I* response of the SOFC.

c) Fuel processing unit

Considering the pure hydrogen is stored at the storage tank, a simple model of a fuel regulator operated in constant fuel utilization mode can be written by the first order equation in the *Laplace transformed* model as [18]

$$M_{H_2}^{in} = \frac{1}{\mu_f F}\left(\frac{1}{sT_d + 1}\right) I_{fc}, \tag{3.44}$$

where μ_f is the utilization factor and T_d is the time constant of the fuel regulator. Equation (3.44) shows that inflow rate of fuel is proportional to the current followed by the system delay. In case of oxygen, excess oxygen is provided to allow it completely react with hydrogen and maintain the pressure difference between the anode and the cathode below a certain threshold value. Oxygen flow rate is, then determined using the hydrogen-oxygen flow ratio, r_{H_2O}.

3.3.2 Model analysis of SOFC

To perform the model verification, a 5 kW SOFC model is developed using parameters given in the appendix. The dynamic and the static response of the fuel cell given in [17] are compared with the model as developed in the above section. The static characteristics of [17] are approximately obtained from the given *V-I* curve for the 5 kW model. To deduce the voltage response, the stack current is increased from 0 to 160 A gradually. The response of the output voltage from the simulink model and the sampled values obtained from [17] (mark by '×') are plotted in Fig. 3-15 (a). It can be seen that developed model agrees with the model as suggested in [17]. The voltage drop at the beginning and end of the curves showed in Fig. 3-15(a) are due to *activation* and *concentration losses*, respectively. The voltage drop in the middle of the curves (approximately linear) is due to the *ohmic loss* in the fuel cell stack.

Similarly, Fig. 3-15 (b) compares the dynamic responses between these models. To check the voltage response, the current waveform used in [17] is subjected to the developed model. The dynamic property the SOFC depends mainly on the double-layer charging effects, delays in fuel and oxidant flow and fuel regulation dynamics. In this case, the fuel regulation block is not included for the comparison with the standard model. Although the capacitance (C_{fc}) due to the double-layer charging effect is large (in the order of several farads for each cell), the time constant $C_{fc}(R_{con,cell} + R_{act,cell})$ is normally small (less than 1 s) because of the small value of net resistance $(R_{con,cell} + R_{act,cell})$. Therefore, C_{fc} will only affect the transient response of the SOFC in the very short time range. On the other hand, the fuel and oxidant flows cannot follow the load current changes instantaneously and the delays can be in the range to several tens of seconds. Fig. 3-15 (b) also illustrates that the developed model agrees with the model of [17]. It should, however, be noted that the voltage response will delay further when included the fuel regulation dynamics.

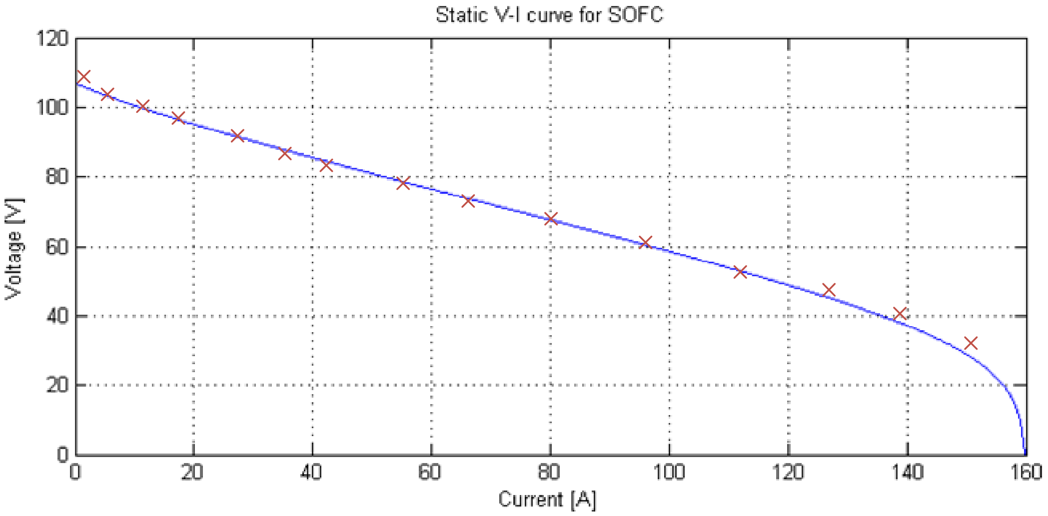

(a)

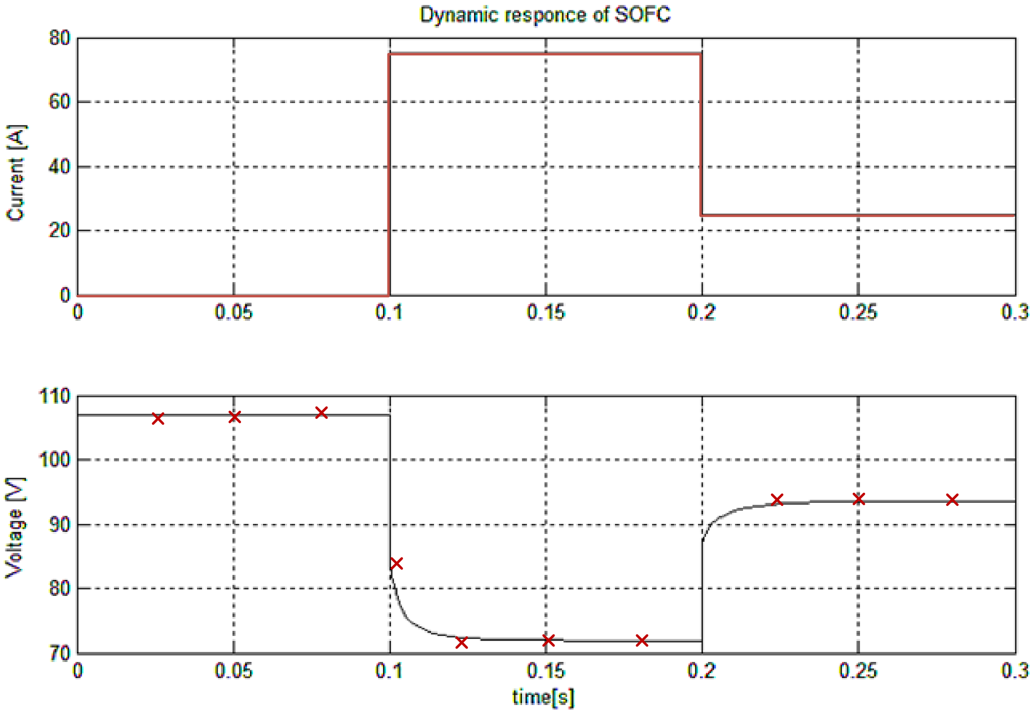

(b)

Fig. 3-15 Model validation of the SOFC. (a) Static and (b) dynamic model.

3.3.3 Electrolyzer

ELZs are the electrochemical devices which produce hydrogen and oxygen by consuming electricity and water, and broadly characterized as the opposite of the fuel cell system [22]. The modeling for the alkaline electrolyzer consists of the electro-chemical part, electrical part, thermal part and hydraulic part. In this study, the thermal modeling is excluded and constant temperature mode is adopted assuming the large time constant (around several minutes) of the thermal model [22],[23].

The electrochemical reaction taking place in the alkaline ELZ with the application of electricity is written as

$$\left.\begin{array}{l} Anode: 2\mathrm{OH}^{-}(aq) \rightarrow \tfrac{1}{2}\mathrm{O}_2(g)+\mathrm{H_2O}+2\mathrm{e}^{-} \\ Cathode: 2\mathrm{H_2O}(l)+2\mathrm{e}^{-} \rightarrow \mathrm{H}_2(g)+2\mathrm{OH}^{-}(aq) \\ l = liquid,\ g = gas,\ aq = aqueous \end{array}\right\}.$$

According to the *Faraday law*, the hydrogen molar production rate can be written as

$$M_{H_2,pro} = \eta(T_{elz}, J_{elz})\frac{N_{elz}}{2F} I_{elz}\,. \tag{3.45}$$

Here J_{elz}, I_{elz}, N_{elz}, T_{elz}, and η are current density, current, number of cell in the stack, temperature of the ELZ and the *Faraday* efficiency, respectively. Equation (3.45) shows that molar production of H_2 is proportional to current, and it is modulated by the Faraday efficiency which is defined as the ratio between the actual and the theoretical maximum amount of hydrogen produced in the ELZ. The Faraday efficiency is often called the current efficiency, because it is caused by parasitic current losses along the gas ducts. The parasitic currents increase with decreasing current densities due to an increasing share of electrolyte and result a lower electrical resistance. Further, an increase in temperature leads to the increase parasitic currents losses, thereby lowering the Faraday efficiencies. An empirical expression for *Faraday efficiency* as the function of current density (J_{elz}) and the temperature is given by [22]

$$\left.\begin{array}{l} \eta = \dfrac{J_{elz}^2}{f_1 + J_{elz}^2} f_2 \\ with,\ \ f_1 = 50 + 2.5T_{elz},\ \ f_2 = 1 - 0.00075T_{elz} \end{array}\right\}. \tag{3.46}$$

The electrical model of the ELZ represents the cell output voltage as a function of input current. It is often derived from the empirical parameters deducted from the experiments. The *V-I* relationship of the ELZ is written as

$$u_{cell} = u_0 + I_{elz} \frac{r_1 + r_2 T_{elz}}{A_{elz}} + u_1 \log\left(\frac{t_1 + t_2 / T_{elz} + t_3 / T_{elz}^2}{A_{elz}} I_{elz} + 1 \right). \tag{3.47}$$

Here u_{cell}, u_0, u_1, and A_{elz} denote the terminal voltage, thermodynamic cell voltage, overvoltage parameter and electrode surface area, respectively. The parameters r_is and t_is represent the dependency of ohmic resistance and overvoltage coefficient on temperature. The terminal voltage across the ELZ cell is the sum of three components: thermodynamic cell voltage which is the function of temperature and pressure, the ELZ overvoltage, and ohmic drop. Based on the parameters values (given in the appendix), static *I-V* curve is plotted (see Fig. 3-16). Clearly, the ELZ can be conceived as a voltage source with an internal resistance; both are nonlinear and sensitive to the temperature and current flow through it.

Since a unit cell has a low value of output potential, a stack is build embedding a number of such units in series, giving the net terminal voltage (V_{elz}) as

$$V_{elz} = N_{elz} u_{cell} . \tag{3.48}$$

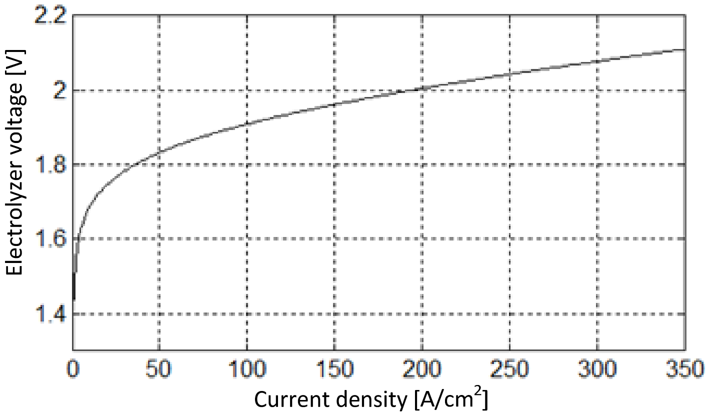

Fig. 3-16 Static *V-I* characteristics curve of the alkaline ELZ.

For a given temperature, an increase in hydrogen production (i.e., an increase in current density) increases the cell voltage (Fig. 3-16), which consequently decreases the energy efficiency. For a given current density, the energy efficiency increases with increasing cell temperature. In order to calculate the overall performance of an ELZ system, information about the number of cells in series and/or parallel per stack and the number of stacks per unit is needed. The rated voltage of an ELZ stack is found from the number of cells in series, while the number of cells in parallel yields the rated current (and thus H_2 production). The total power is simply the product of the current and voltage. While developing the stack of the rated value, it is considered that the no-load voltages of the SOFC and ELZ are equal. In other words making $N_{cell}E_{cell}=N_{elz}u_0$, there would be a continuous static *I-V* curve for the SOFC/ELZ unit leading to smooth transition between the SOFC to ELZ operation modes.

The *hydraulic part* of an ELZ consists of the dynamics of the resultant gases. If we ignore the H_2 leakage rate, the accumulating rate of the H_2 inside the ELZ is difference between the production and outlet rate. Based upon the ideal gases law, the resultant pressure dynamics can be written as

$$\frac{U_{elz}}{RT_{elz}}\frac{d}{dt}p_{H_2,elz}=M_{H_2,pro}-M_{H_2,out}, \tag{3.49}$$

where $p_{H_2,elz}$ is the partial pressure of hydrogen inside the ELZ, U_{elz} is the volume of electrolyzer and $M_{H_2,out}$ is the outflow rate of hydrogen from the ELZ. At steady state, the outflow rate is maintained equal to the production rate to make the pressure constant.

3.3.4 Compressor and tank model

According to the *polytropic* compression model, the relationship between the hydrogen molar flow rate and the compressor power is [23]

$$\left.\begin{aligned} M_{H_2,out}&=\frac{\alpha_{com}}{w}P_{comp}\\ w&=\frac{\nu T_{elz}}{\nu-1}\left[\left(\frac{p_{tank}}{p_{H_2,elz}}\right)^{\frac{\nu-1}{\nu}}-1\right]\end{aligned}\right\}. \tag{3.50}$$

Equation (3.50) shows outflow of H_2 from the ELZ is decided by the compressor power (P_{comp}), the polytropic work (w), polytropic coefficient (ν) and the compression efficiency (α_{com}). Polytropic work is derived from the thermodynamic law, by which H_2 is supplied to the higher pressure (p_{tank}). The stored hydrogen rate in the tank depends upon the difference between the inflow rate and the outflow rate. Thus, the pressure of stored hydrogen in the tank can be written as

$$\frac{U_{tank}}{RT_{tank}}\frac{d}{dt}p_{tank}=M_{H_2,out}-M_{H_2}^{in}, \tag{3.51}$$

where U_{tank} and T_{tank} represent the volume and temperature of storage tank, respectively. Based upon the above equations, the block diagram of hydrogen production and storage is constructed and shown in Fig. 3-17.

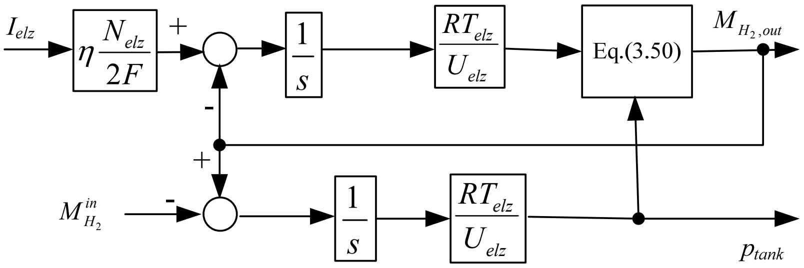

Fig. 3-17 Block diagram of hydrogen production and storage model.

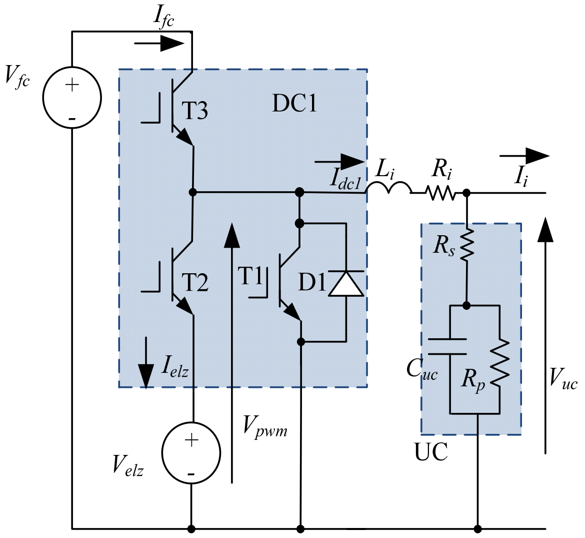

(a)

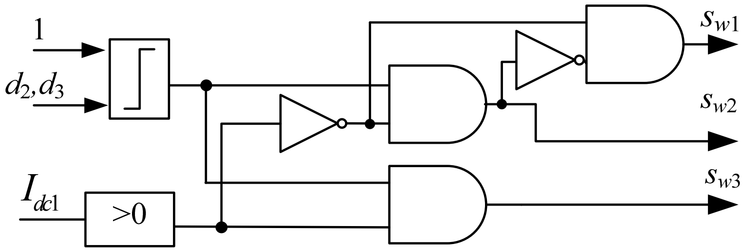

(b)

Fig. 3-18 Electrical diagram of the bi-directional dc-dc chopper. (a) Circuit diagram, and (b) switching logic. The variable s_{wi} are the gate signals for the transistor Ti (i=1,2,3).

3.3.5 dc-dc converters

Proposed DESS employs two dc-dc converters, the FC/ELZ side converter (DC1) and isolating converter (DC2). While the converter DC1 is responsible for the regulation of the FC/ELZ current and ultracapacitor terminal voltage, the converter DC2 is responsible for the dc-link bus regulation. In other words, DC1 and DC2 are operated in current and voltage regulation modes, respectively.

The model for the chopper (DC1) employed to regulate the current through the FC/ELZ and V_{uc} is illustrated in Fig. 3-18(a). This model resembles the classical two-quadrant dc-dc chopper with minor modifications in switching elements to accommodate the FC and ELZ control action by the same converter. The working principle of DC1 is easily understood from the switching pattern depicted in Fig. 3-18(b). The direction I_{dc1} determines the operating modes of DC1– buck or boost mode. During the power deficit (for $I_{dc1}>0$), the duty cycle (d_3) generates s_{w3} to turn T3 through the PWM action activating the FC, and then turns T1/T2 OFF (with $s_{w2}=s_{w1}=0$) at the same time. Similarly during power surplus (for $I_{dc1}<0$), the duty cycle generates s_{w2}/s_{w1} to turn T2/T1 in complementary way and activates ELZ, while turning T3 OFF (with $s_{w3}=0$) at the same time. By forcing the desired value of I_{dc1} (hence the current flowing through the FC/ELZ), the control action provides direct control over the UC voltage without using a separate dc-dc interface. With d_2 (d_3) as the duty cycle of T2 (T3) and noting that d_2 (d_3) is activated when $I_{dc1}<0$ ($I_{dc1}>0$), the averaged equations for voltage and current can be written as

$$\left.\begin{aligned} &I_{fc}=d_3 I_{dc1},\ I_{elz}=-d_2 I_{dc1} \\ &V_{pwm}=d_3 V_{fc}+d_2 V_{elz} \end{aligned}\right\}. \tag{3.52}$$

From Kirchhoff's voltage law, we can write

$$L_i \frac{dI_{dc1}}{dt}+I_{dc1}R_i=V_{pwm}-V_{uc}. \tag{3.53}$$

For the regulation of V_{dc}, a full-bridge converter (DC2) is implemented because of its (i) high power capability, (ii) zero voltage/current switching provision for loss reduction, and (iii) isolation of FC/UC/ELZ system from the rest of the electrical network. The switching model of DC2 is shown in Fig. 3-19(a). For the simplicity of analysis and managing the simulation time/storage, the average model is used here, which can be deducted with following set of equations [24],[25]

$$\left.P=\frac{V_{uc}V_{dc}}{2\pi f_s L_t}\left(\delta-\frac{\delta^2}{\pi}\right),\quad V_{uc}I_i=V_{dc}I_{dc}\right\};\tag{3.54}$$

$$\left.I_i=\frac{V_{dc}}{2\pi f_s L_t}\left(\delta-\frac{\delta^2}{\pi}\right),\quad I_{dc}=\frac{V_{uc}}{2\pi f_s L_t}\left(\delta-\frac{\delta^2}{\pi}\right)\right\};\tag{3.55}$$

where δ is the phase shift angle, and the other parameters/variables in the above equations are defined in Fig. 3-19(a). From (3.54) and(3.55), it can be observed that the phase shift variable determines the magnitude and direction of the current. The positive value of δ indicates the power deficit (current supplying to dc bus), and the negative value indicates the power surplus (current drawing from the dc-link bus). The approximated averaged model is depicted in Fig. 3-19(b).

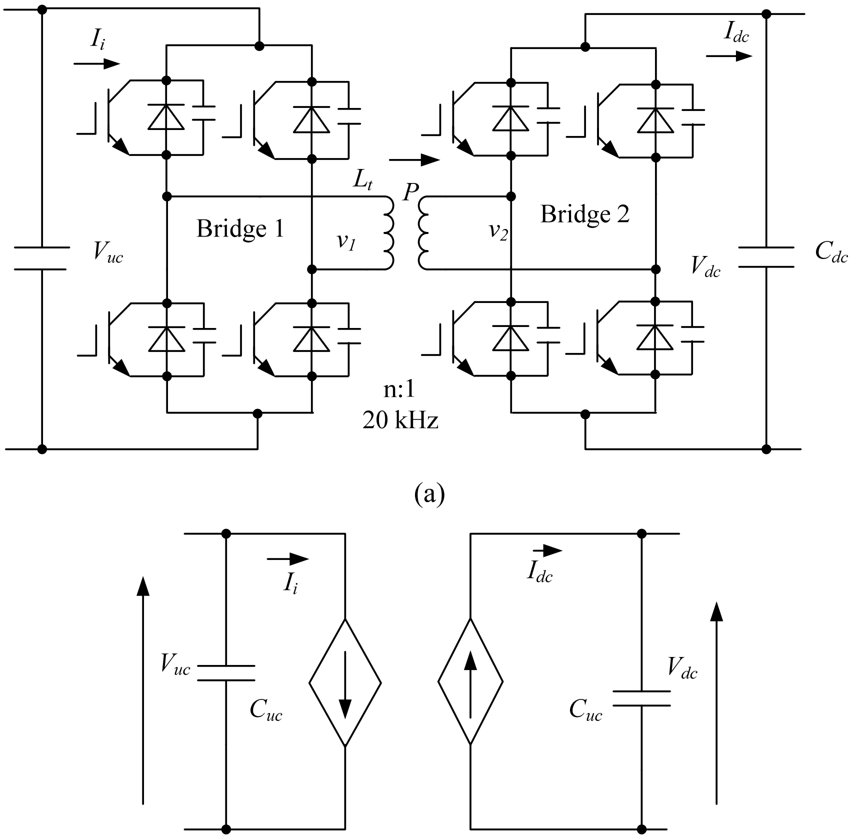

(a)

(b)

Fig. 3-19 Electrical diagram of the full bridge dc-dc converter. (a) Switching model, and (b) averaged model on the basis of (3.55).

3.3.6 Ultracapacitor

This study has used the classical model of a UC (see Fig. 3-20), which consists of an electrical double layer capacitance (C_{uc}), an equivalent series resistance (R_{sr}) and a parallel resistance (R_{pl}). R_{sr} represents the charging and discharging resistance, whereas R_{pl} models the leakage effects applicable in the long-term energy storage performance of the UC [26],[27]. The dynamic equation representing the *Kirchhoff's current law* is written as

$$C_{uc}\frac{dV_{uc}}{dt}+\frac{V_{uc}}{R_{pl}}=I_{dc1}-I_i\,. \tag{3.56}$$

Unlike battery system, a UC allows a wide range of voltage variation to leverage the maximum energy exchange. The amount of energy consumed/drawn from the UC bank (E_{uc}) in extreme condition is deducted, with the specified values of the initial and final value of the UC voltages, as

$$E_{uc}=\frac{1}{2}C_{uc}\left(V_i^2-V_f^2\right). \tag{3.57}$$

When the energy is released from the UC, the magnitude of the voltage is decreased and vice versa. While sizing the UC, we consider the amount of energy that UC can exchange on the extreme conditions. This, in turn, is decided by the transient behavior of the FC and the loading conditions. Since the FC has poor transient response, the UC should have a large value, sufficient enough, to fulfill the transient demand (by remaining within the allowable range of terminal voltage), until the FC provide the rated steady-state current. To match the desired voltage level and the capacitance, numbers of UC units are assembled in the series and parallel fashion, based upon the data sheet of Maxwell BMOD0110® [28].

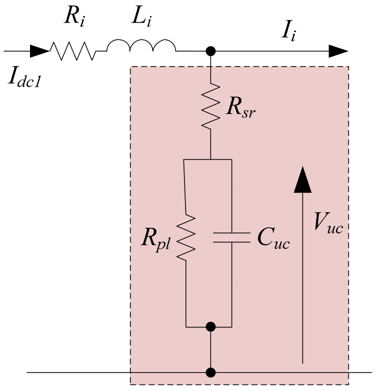

Fig. 3-20 Electrical diagram of UC.

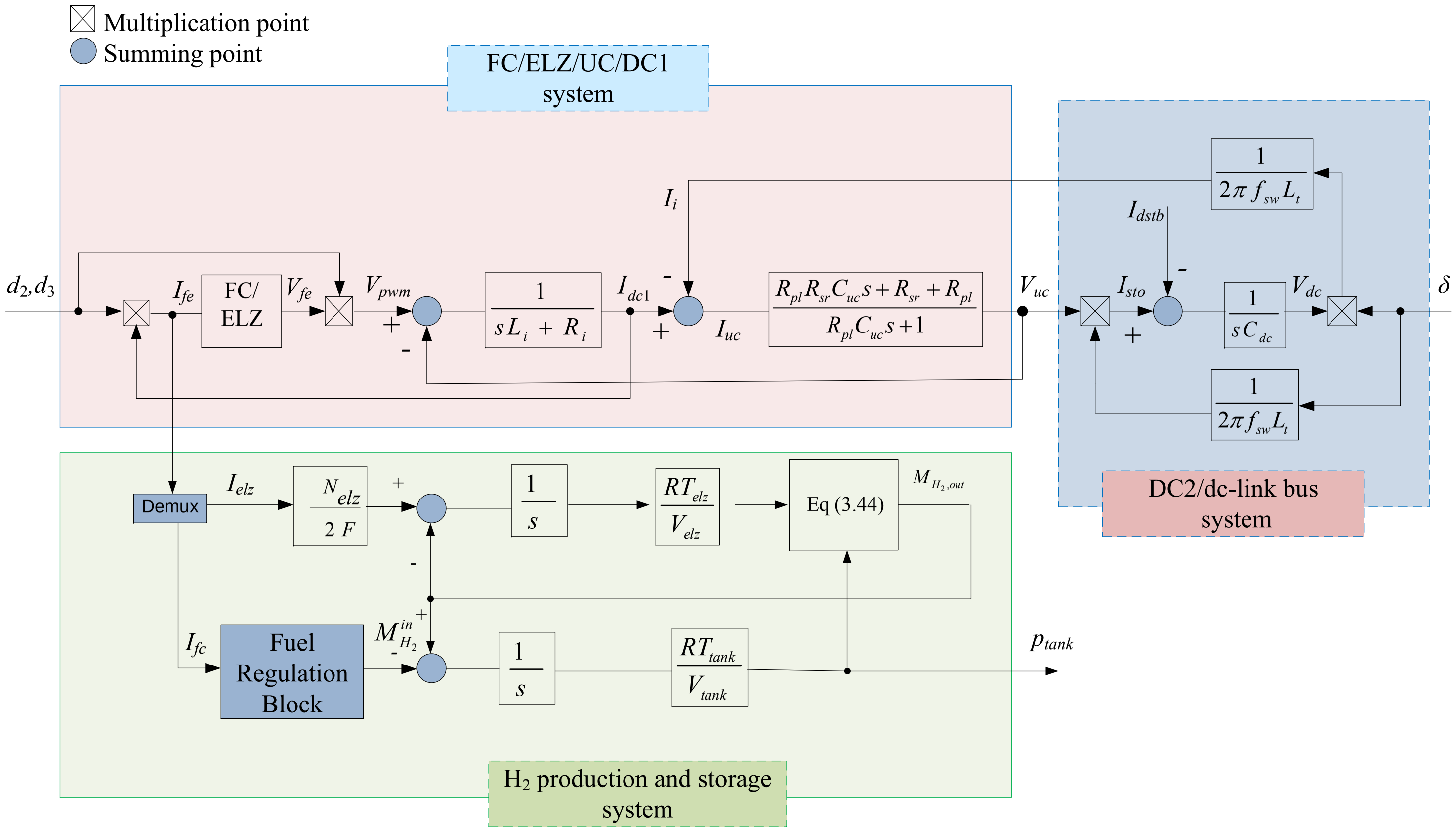

Fig. 3-21 Overall control block diagram of the dedicated energy storage system.

3.3.7 Summary of dynamics in the DESS

The dynamic equations for DESS are summarized by the following set of equations.

$$\left.\begin{aligned}
&\frac{d}{dt}p_{H_2}=\frac{2RT_{fc}}{U_a}M_{H_2}^{in}-\frac{2M_aRT_{fc}}{P_aU_a}p_{H_2}-\frac{RT_{fc}}{2FU_a}I_{fc}\\
&\frac{d}{dt}p_{H_2O}=\frac{2RT_{fc}}{U_a}M_{H_2O}^{in}-\frac{2M_aRT_{fc}}{P_aU_a}p_{H_2O}+\frac{RT_{fc}}{2FU_a}I_{fc}\\
&\frac{d}{dt}p_{O_2}=\frac{2RT_{fc}}{U_c}M_{O_2}^{in}-\frac{2M_cRT_{fc}}{P_cU_c}p_{O_2}-\frac{RT_{fc}}{4FU_c}I_{fc}\\
&V_{dl}=\left(I_{fc}-C_{fc}dV_{dl}/dt\right)(R_{act,cell}+R_{con,cell})\\
&T_d\frac{dM_{H_2}^{in}}{dt}=-M_{H_2}^{in}+\frac{1}{\mu_fF}I_{fc}\\
&T_d\frac{dM_{O_2}^{in}}{dt}=-M_{O_2}^{in}+\frac{r_{H_2O}}{\mu_fF}I_{fc}
\end{aligned}\right\}\qquad(3.58)$$

$$\left.\begin{aligned}
&L_i\frac{dI_{dc1}}{dt}=-I_{dc1}R_i-V_{uc}+d_3V_{fc}+d_2V_{elz}\\
&C_{uc}\frac{dV_{uc}}{dt}=I_{dc1}-\frac{V_{uc}}{R_p}-I_i
\end{aligned}\right\}\qquad(3.59)$$

$$\left.\begin{aligned}
&\frac{U_{elz}}{RT_{elz}}\frac{d}{dt}p_{H_2,elz}=M_{H_2,pro}-M_{H_2,out}\\
&\frac{U_{\text{tank}}}{RT_{\text{tank}}}\frac{d}{dt}p_{\text{tank}}=M_{H_2,out}-M_{H_2}^{in}
\end{aligned}\right\}\qquad(3.60)$$

The overall control block diagram of DESS is depicted in Fig. 3-21. It consists of three units; FC/ELZ/UC/DC1 system, DC2/dc-link bus system, and H_2 production and storage system. The FC/ELZ/UC/DC1 system has two inputs (duty cycle as command reference and I_i as the disturbance input) and two outputs (I_{fc} and V_{uc}); DC2/dc-link bus system has three input variables (δ, V_{uc} and I_{dstb}) and an output variable (I_i); and H_2 production and storage system. The first and second block will be used to design the control schemes for DC1 and DC2, respectively; while the last one is the feed forward block reflecting the fuel production/consumption.

While observing the set of differential equations, it can be noticed that (3.60) only appears at the output part and does not include the feedback loop, so it has no role in the system stability. The remaining state transition matrix is almost diagonal except those related to (3.59) where cross coupling exists. Here, the equilibrium point of the system is at origin as the stable node. That means with no inputs, all the states finally converse into the origin irrespective of the initial conditions. Further, the system has time constants of different time scales. Time constant for the reactants' partial pressure, fuel processing in (3.58), have larger values of around several seconds dominating the system dynamics; while the time constants for I_{dc1} and V_{dl} is around few milliseconds. The presence of the sluggish dynamics in the FC, represents the attribute of poor power density; that means its inability for transient mitigation. Therefore, an energy storage device with high power density is required, and the UC fulfils this demand. These characteristics, together with the block diagram in Fig. 3-21, will be in focus while designing the control laws for DC1 and DC2 to be explained in the next chapter.

3.4 Remarks on System Modeling

In the system modeling explained in this chapter, we observed that dynamic equations are mainly the linear types under various assumptions, which are selected to investigate the fundamental aspects of dynamic behavior within the frame work of the research objectives. It applies to the WTGS, DESS and VSC models. These models may be too optimistic when we try to study the system responses under the broader operating conditions and system severities. In such cases, adoption of more comprehensive models with in-depth nonlinear dynamics may be suggested, which can provide a larger picture on the equilibrium points and the stability regions. In that context, the component models reported here may not be enough; thereby demanding more work, especially, on the element level research. Nevertheless, in the integrated system level study with given operational objectives of the proposed microgrid, the models adopted here are expected to expose system responses without losing the accuracy level.

References

[1] G. Johnson, *Wind energy systems*: Prentice-Hall Englewood Cliffs (NJ), 1985.

[2] T. Thiringer and J. Linders, "Control by variable rotor speed of a fixed-pitch wind turbine operating in a wide speed range," *IEEE Transactions on Energy Conversion*, vol. 8(3), pp. 520-526, 1993.

[3] Horns rev offshore wind farm, available online at: http://www.hornsrev.dk/nyheder/brochurer/Horns_Rev_GB.pdf.

[4] T. Ackermann, *Wind power in power systems*, John Wiley and Sons Ltd, 2006.

[5] P. Anderson and A. Bose, "Stability simulation of wind turbine systems," *IEEE Transactions on Power Apparatus and Systems*, Vol. PAS-102(12), pp. 3791-3795, 1983.

[6] Danish Wind Energy Association, Guided Tour, available online: http://guidedtour.windpower.org/en/tour/wtrb/stall.htm

[7] T. Burton, D. Sharpe, N. Jenkins and E. Bossanyi, *Wind Energy Handbook,* John Wiley and Sons Ltd, 2004.

[8] F. Bianchi, et al., *Wind Turbine Control Systems: Principles, Modelling and Gain-scheduling Design,* Springer, 2006.

[9] J. Hu and Y. He, "Dynamic modelling and robust current control of wind-turbine driven DFIG during external AC voltage dip," J*ournal of Zhejiang University Science*, vol. 7(10), pp. 1757-1764, 2006.

[10] C. Ong, *Dynamic simulation of electric machinery: using Matlab/simulink,* Prentice Hall, New Jersey, 1998.

[11] M. Rashid, *Power electronics handbook*: Academic Press, 2001.

[12] M. Tsai and W. Tsai, "Analysis and design of three-phase AC-to-DC converters with high power factor and near-optimum feedforward," *IEEE Transactions on Industrial Electronics*, vol. 46(3), p. 535, 1999.

[13] V. Blasko and V. Kaura, "A new mathematical model and control of a three-phase AC–DC voltage source converter," *IEEE Transactions on Power Electronics*, vol. 12(1), 1997.

[14] A. Dicks and J. Larminie, *Fuel cell systems explained*: John Wiley & Sons, 2000.

[15] R. Bove and P. Lunghi, "SOFC mathematic model for systems simulations-Part 2: definition of an analytical model," *International Journal of Hydrogen Energy*, vol. 30(2), pp. 189-200, 2005.

[16] P. Aguiar, D. Chadwick and L. Kershenbaum, "Modeling of an indirect internal reforming solid oxide fuel cell," Chemical Engineering Science, vol. 57(10), pp. 1665-1677, 2002.

[17] J. Padulles, G. Ault and J. McDonald "An integrated SOFC plant dynamic model for power systems simulation," *Journal of Power Sources*, vol. 86(1-2), pp. 495-500, 2000.

[18] C. Wang and H. Nehrir, "A physically based dynamic model of solid oxide fuel cells," *IEEE Transaction on Energy Conversion,* vol. 22(4), Dec. 2007.

[19] G. Hatsopoulos and J. Keenan, *Principles of general thermodynamics:* Wiley New York, 1965.

[20] *Fuel cell handbook:* EG & G Services, 2002.

[21] S. Chan, C. Low and O. Ding, "Energy and exergy analysis of simple solid-oxide fuel-cell power systems," *Journal of Power Sources*, vol. 103(2), pp. 188-200, 2002.

[22] Ø. Ulleberg, "Modeling of advanced alkaline electrolyzers: a system simulation approach," *International Journal of Hydrogen Energy*, vol. 28(1), pp. 21-33, Jan. 2003.

[23] T. Zhou and B. Francois, "Modeling and control design of hydrogen production process for an active hydrogen/wind hybrid power," *International Journal of Hydrogen Energy*, vol. 34(1), pp. 21-30, Jan. 2009.

[24] S. Inoue and H. Akagi, "Bi-directional dc/dc converter for an energy storage system," 22nd IEEE Applied Power Electronics conference, Feb.-Mar. 2007.

[25] R. De Doncker, D. Divan and M. Kheraluwala, "A three-phase soft-switched high power density DC/DC converter for high power applications," *IEEE Transaction on Industry Application*, vol. 27(1), pp. 63-73, 1991.

[26] O.C. Onar, M. Uzunoglu and M.S. Alam, "Modeling, control and simulation of an autonomous wind turbine/photovoltaic/fuel cell/ultracapacitor," *Journal of Power Sources*, vol. 185(2), pp. 1273-1283, Dec. 2008.

[27] R. L. Spyker and R. M. Nelms, "Analysis of double-layer capacitors supplying constant power loads," *IEEE Trans. Aerospace Electron*, vol. 36(4), pp. 1439-1443, Oct. 2000.

[28] "Electric Double Layer Capacitor: BOOSTCAP_ Ultracapacitor," Available online at: http://www.maxwell.com/pdf/uc/datasheets/mc_power_series_48_1009365_rev3.pdf.

Chapter 4 Control and Operation Schemes

The purpose of an autonomous electric power system is to produce electricity from its generators so that it can supply the local demand and transfer predefined power to the external network at acceptable quality and reliability. In the conventional power generation system, the balance of supply and demand is made by controlling the fuel input to the generator's governing system, so the load-following approach can be handled easily. In a power system with renewable generators, the load-following approach cannot be achieved since the power generation is affected by the intermittent weather conditions. Instead, the generators are operated in the way to capture maximum input energy available. Consequently, integration of the dedicated energy storage system (DESS) is indispensable to make renewable based power system an autonomous one, which serves as the medium of energy and power balance.

The main objectives of the proposed hybrid power system are: to capture as much as wind energy available, and supply the local load demand and dispatchable power using the dedicated energy storage system. To fulfill the objectives, there are three subsystems to be controlled. In particular, the control action for the wind turbine generator system (WTGS) enables in getting optimum power from wind; the control action for the line side converter (VSC2) regulates the power, frequency and voltage of the point of common coupling (PCC) bus; and the control action for the DESS balances the supply and demand of power (in transient condition) and energy (in steady-state condition), irrespective of fluctuations in load and variations in generation. Each of these subsystems has many control variables to achieve the desired results, and the control laws of the variables are based on the dynamic models of each subsystem. There are many approaches to the controller or the compensator design. Due to simplicity for designing, internal model control (IMC) scheme is used in this study to select the parameters of the controllers. In the following sections, the conceptual framework of the IMC based design is described first, followed by the description of the control/operational schemes for the each subsystem.

4.1 Internal Model Control Based Design of Controllers

The goal of a typical control design is to get fast and accurate *set-point tracking* against the effect of *external disturbances*. Further, the resultant system should be capable to operate over a wide range of operating conditions with enough *stability margins*. The controller is usually designed based on an approximate model of the real plant, and it is likely that the parameters of the plant vary with operating conditions and time. Therefore, it is essential to design a control system that shows robust performance against mismatches. In this study, proportional-integral-derivative (PID) type controllers are applied due to their relatively simple structures, which can be comprehended and implemented easily in practices. Finding a simple design technique for PID type controllers with the desired performances is an important issue in tuning the controllers. There are a number of methods for tuning PID controllers, among which the IMC based design approach is often used in process control systems because it demonstrates a clear tradeoff between the closed loop performance and robustness, by means of a single tuning parameter namely the filter time constant [1]. The following paragraphs describe an evolution of a simple IMC structure to obtain the PID control schemes, in brief.

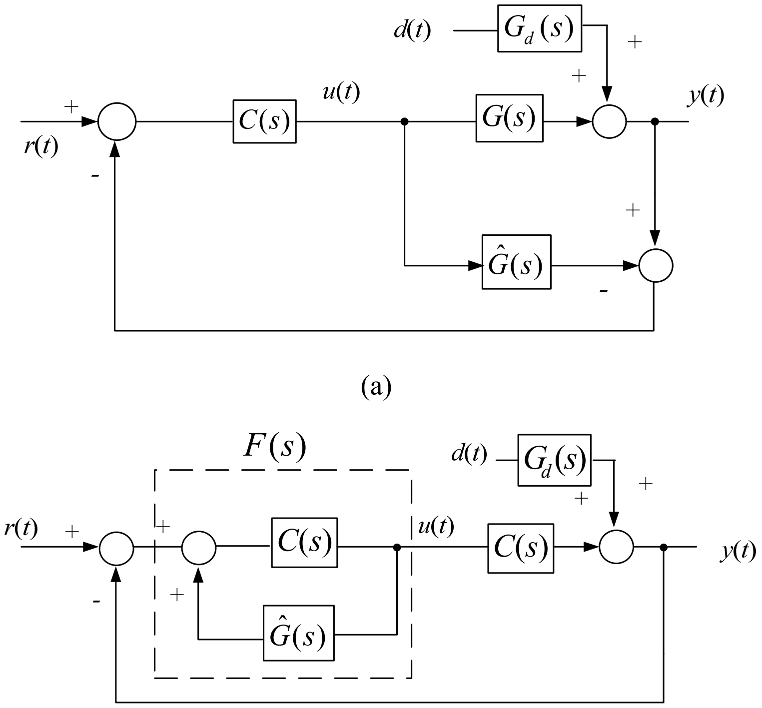

(a)

(b)

Fig. 4-1 Plant control topologies. (a) Internal model structure, and (b) equivalent classical model.

A commonly used IMC structure is illustrated in Fig. 4-1(a). The structure uses an internal model $\hat{G}(s)$ in parallel with the controlled plant $G(s)$. To get the desired response, a control block $C(s)$ is augmented so that the output is related as [2]

$$Y(s)=\underbrace{\left(\frac{C(s)G(s)}{1+[G(s)-\hat{G}(s)]C(s)}\right)}_{G_{CLR}}R(s)+\underbrace{\left(\frac{1-C(s)\hat{G}(s)}{1+[G(s)-\hat{G}(s)]C(s)}G_d(s)\right)}_{G_{CLD}}D(s) \tag{4.1}$$

where "^" denotes the measured value of the parameter; the symbols *r, y, u* and *d* denote the reference input, the controlled output, the plant input and the disturbance input, respectively as specified in the figure. Similarly, $G_d(s)$ is the disturbance transfer function and the variables with capital letters represent the mathematical expressions in the *Laplace Transformation* domain. This IMC can be considered as a special case of the classical control structure as shown in Fig. 4-1(b), where an equivalent controller block $F(s)$ is related to the internal model in the following way

$$F(s)=[1-C(s)\hat{G}(s)]^{-1}C(s). \tag{4.2}$$

If we desire to get set-point tracking, it is necessary to make $C(0)\hat{G}(0)-1=0$. This guides us to set $C(0)\hat{G}(0)=1$. For the sake of simplified understanding of the IMC, consider the case when the internal model is perfect, i.e., $G(s)=\hat{G}(s)$, then there is no feedback in Fig. 4-1(a). Consequently, the output becomes

$$Y(s)=C(s)G(s)R(s)+[1-C(s)G(s)]G_d(s)D(s). \tag{4.3}$$

In this case, the close loop system is stable if $C(s)$ and $G(s)$ are both stable, implying that we have stablizing controllers $F(s)$, given by (4.2), for the stable plant $G(s)$. Under this condition, if we set $C(s)=\hat{G}^{-1}(s)$, all plant dynamics would be canceled and the output signal would attain the set point instantaneously. Though the approach seems tempting, it is not applied because of several reasons, such as: (i) the possibility of $G(s)$ being non-mimimal phase (presence of zeros in the right-half plane, which makes $G^{-1}(s)$ unstable), (ii) the possibility of $G^{-1}(s)$ being improper, and (iii) the approach is highly sensitive to the model error. This conpect, however, can still be used with a minor modifications in the control structure. A general approach is to factorize $G(s)=G_M(s)G_A(s)$; such that $G_A(s)$ is the *allpass* part of $G(s)$ including all zeros in the right-half complex plane and the time delay, and $G_M(s)$ is the remaining part. Then, we introduce a filter

$$L(s) = \left(\frac{1}{1+s\alpha}\right)^n, \tag{4.4}$$

where n is a positive integer chosen sufficiently large so that $C(s)$ becomes proper, and α is the parameter to adjust the filtering function that provides the tradeoff between performance and the robustness. Now, by setting $C(s) = \hat{G}_M^{-1}(s)L(s)$, we can address all the aforementioned issues with $C(s) = \hat{G}^{-1}(s)$ [1]. Let us derive the resultant close loop response as

$$Y(s) = \underbrace{\left(\frac{\hat{H}(s)[1+E_M(s)]}{1+\hat{H}(s)E_M(s)}\right)}_{G_{CLR}} R(s) + \underbrace{\left(\frac{1-\hat{H}(s)}{1+\hat{H}(s)E_M(s)} G_d(s)\right)}_{G_{CLD}} D(s), \tag{4.5}$$

where $\hat{H}(s) = L(s)\hat{G}_A(s)$ and $E_M(s)$ is the model error given by $E_M(s) = [G(s) - \hat{G}(s)] / \hat{G}(s)$. For the special case of a perfect model ($E_M(s) = 0$), (4.5) reduces to

$$Y(s) = \hat{H}(s)R(s) + [1-\hat{H}(s)]G_d(s)D(s), \tag{4.6}$$

as a result of pole-zero cancellation. Clearly, (4.6) demonstrates that for the model with no mismatch, the nominal close loop transfer function $\hat{H}(s) = L(s)\hat{G}_A(s)$ is the designer's choice provided $\hat{G}_A(s)$ contains all the right-half plane zeros and delays, and $L(s)$ must be of sufficiently high order to avoid physically unrealistic control action. This idea leads us to designing the equivalent classical model of feedback control structure via $F(s)$ as defined in (4.2) and Fig. 4-1(b).

Substituting the value of $C(s)$ in (4.2), we get

$$F(s) = \frac{L(s)}{\hat{G}_M(s)[1-L(s)\hat{G}_A(s)]}. \tag{4.7}$$

In our study model, there are no zeros on the positive half-plane nor the delay part (i.e $\hat{G}_A(s) = 1$), which simplifies the design part substantially. As an illustration, consider a first order system $G(s) = k_M / (\tau_p s + 1)$ where k_M and τ_p are the value of gain and time constant, it is sufficient to set n = 1, in which case α becomes the desired bandwidth of the closed-loop system. Consequently, the controller becomes an ordinary proportional-integral (PI) controller expressed by

$$F(s)=\frac{1}{\alpha s}\hat{G}^{-1}(s)=\frac{s\tau_p+1}{s\alpha k_M}=\frac{\tau_p}{\alpha k_M}+\frac{1}{s\alpha k_M}. \tag{4.8}$$

Then, the output response with the nominal model becomes

$$Y(s)=\frac{1}{\alpha s+1}R(s)+\frac{\alpha s}{\alpha s+1}G_d(s)D(s). \tag{4.9}$$

Thus, the tracking of command input and disturbance rejection is matter of selecting desired value of α.

Improved IMC

While the conventional filter suggested by (4.4) provides good performance for set point tracking, it may result poor performance for disturbance rejection. To show this, consider the closed-loop output response, in which $G_d(s)$ having the same dynamics as that of the plant in Fig. 4-1. Then, the output response of (4.9) can be written as

$$Y(s)=\frac{1}{1+\alpha s}R(s)+\frac{k_M\alpha s}{(s\alpha+1)(s\tau_p+1)}D(s). \tag{4.10}$$

If τ_p is large, the disturbance rejection will be poor as guided by τ_p, whatever the value of α we select. That means there will exist a long tail in $y(t)$ due to $d(t)$. To fix this problem, an improved filter form (for *type I* with step input) is suggested as [3]

$$L(s)=\frac{1+\gamma s}{(1+\alpha s)^n}. \tag{4.11}$$

The constant parameter γ is chosen so that the slow pole of $G_d(s)$ is canceled by a zero (via pole zero cancellation) in the transfer function, $Y(s)/D(s)$. Such a pole-zero cancellation is effective if: (i) the plant dynamics is relatively known, (ii) plant does not have unstable open loop poles, and (iii) the system does not have internal disturbances associated with the dynamics slower than the desired closed-loop response. Consequently, by substituting the value of $L(s)$ from (4.11) to (4.7), the expression for $F(s)$ can be written as

$$F(s)=\frac{\gamma s+1}{\hat{G}_M(s)[(\alpha s+1)^n-(\gamma s+1)]}. \tag{4.12}$$

As an illustration, for the first order system with $G(s)=k_M/(s\tau_p+1)$ as in the earlier example, we set $n=2$, in which case $F(s)$ becomes

$$F(s) = \frac{(\gamma s+1)}{s(\alpha^2 s+2\alpha-\gamma)}\hat{G}_M^{-1}(s) = \frac{(\gamma s+1)}{s(\alpha^2 s+2\alpha-\gamma)}\frac{s\tau_p+1}{k_M} \ . \tag{4.13}$$

By setting $\tau_p = \alpha^2/(2\alpha-\gamma) \ or \ \gamma = 2\alpha - \alpha^2/\tau_p$, the output response with ideal model becomes

$$Y(s) = \frac{(\gamma s+1)}{(\alpha s+1)^2}R(s) + \frac{k_M(2\alpha-\gamma)s}{(\alpha s+1)^2}D(s) \ . \tag{4.14}$$

Thus, we can select the desired settling time for the command point tracking and disturbance rejection by specifying the parameters α and γ. In case of models having mismatches with the real plants, the resultant output response will be close to (4.14) as guided by (4.5) and (4.7).

This concept of the controller design as summarized by (4.8) and (4.12) is used in tuning them and the resultant control transfer function is given in the appendix at the respective places.

4.2 Wind Turbine Generator System Controller

The main objectives of the WTGS controller are to regulate and smooth the generated power; maximize the energy captured, alleviate the transient loads throughout the wind turbine, and reduce the machine rotor flux at light load. These objectives are effectively accomplished by utilizing a variable-speed drive and pitch angle control. While the variable-speed operation is employed to the rotor-side converter (VSC1) throughout operation, the pitch angle control is activated only at the wind speed above the rated value (see section 3.2.2).

The control of VSC1 deals with the dynamic characteristics given in (3.17) and (3.29). At first glance, the design of control scheme seems to be complex, as it has sixth order non-linear multiple-input multiple-output (MIMO) system. The design part, however, can considerably be simplified if we note following points.

- Since the stator terminal is connected to the voltage regulated ac bus (either it is regulated by the VSC2 controller or it is impressed by the grid voltage), the derivative of $\mathbf{i}_{mo}$ is very small and the voltage equation becomes algebraic one.
- The dc-link bus voltage regulation is delegated to the DESS, so the control scheme does not have to deal with it [4].
- In the vector control scheme, the cross-coupling effect is nullified. It means that the variables of the other axis are termed as disturbance signals. This leads to simplifying the MIMO system into the separate single-input single-output (SISO) systems.

With these conditions, the control law associated with VSC1 can be expressed by two SISO systems that handle the third order dynamics. The detail description of control scheme is presented in the following subsections.

4.2.1 Inner current control of rotor-side converter

The main task of the rotor-side converter is to control the machine speed and flux. Due to the machine inherent dynamics, the speed and the flux control is accompanied with the fast inner current control loop that controls the rotor current. To achieve the effective control, it is preferred to decouple the torque and flux quantities by employing the *field orientation* concept, such that q-axis component of the rotor current dictates the torque and the d-axis component is used to regulate the excitation flux or the reactive power.

In the *stator field oriented control*, synchronously rotating d-axis is oriented along the stator flux vector position. Assuming the stator terminal is connected to the voltage regulated bus, the magnetizing current vector ($\mathbf{i}_{mo}$) is nearly constant. Further, the influence of stator resistance is very negligible. Under this orientation, expressions for the quantities of interest (voltages, torque, rotor speed, stator flux and stator reactive power) can be deducted from (3.15) to (3.22) as [4, 5]

$$\left.\begin{aligned} |\boldsymbol{\psi}_s| &= \psi_{sd} = L_s|\mathbf{i}_{mo}| = L_s i_{sd} + L_m i_{rd} \\ \psi_{rd} &= L_m^2 i_{mo}/L_s - \sigma L_r i_{rd},\ \psi_{rq} = \sigma L_r i_{rq} \end{aligned}\right\}, \tag{4.15}$$

$$\left.\begin{aligned} v_{rd} &= r_r i_{rd} + \sigma L_r (di_{rd}/dt) - v_{dcom} \\ v_{rq} &= r_r i_{rq} + \sigma L_r (di_{rq}/dt) + v_{qcom} \\ J_m(d\omega_r/dt) &= (T_m - T_{em}) - D_m\omega_r \end{aligned}\right\}, \tag{4.16}$$

with

$$\left.\begin{aligned} v_{dcom} &= (\omega_e - \omega_r)\sigma L_r i_{rq} \\ v_{qcom} &= (\omega_e - \omega_r)\sigma L_r i_{rq} + (L_m/L_s)\psi_{sd} \end{aligned}\right\} \tag{4.17}$$

$$T_{em} = 0.75 n_p \psi_{sd} i_{rq} \tag{4.18}$$

$$Q_s = 1.5(\omega_e - \omega_r)L_m\psi_{sd}(i_{rd} - \psi_{sd}/L_m)L_s^{-1}. \tag{4.19}$$

To design the observer for the stator flux vector position, the stator voltage and the current quantities are taken as feedback variables. By using stationary *Clark's transformation*, the flux and its phase angle is calculated as [6]

$$\left.\begin{aligned}
&\psi_{s\alpha} = \int (v_{s\alpha} - r_r i_{s\alpha})dt, \;\; \psi_{s\beta} = \int (v_{s\beta} - r_r i_{s\beta})dt \\
&\theta_f = \tan^{-1}(\psi_{s\beta} / \psi_{s\alpha}) \\
&\psi_s = \sqrt{\psi_{s\alpha}^2 + \psi_{s\beta}^2}
\end{aligned}\right\}, \tag{4.20}$$

where the subscripts α and β represents the variables in α and β axes, respectively; and θ_f denotes angle of rotating flux. From (4.16), it is possible to include a feed-forward compensating term in the control law that will compensate the tracking error caused by the variation of v_{dcom} and v_{qcom}. Consequently, the desired rotor voltage is derived as

$$\left.\begin{aligned}
v_{rd} &= (i_{rd}^{ref} - i_{rd})G_{C1}(s) - \hat{v}_{dcom} \\
v_{rq} &= (i_{rq}^{ref} - i_{rq})G_{C1}(s) + \hat{v}_{qcom}
\end{aligned}\right\}, \tag{4.21}$$

where the superscript '*ref*' represents the set value of the respective quantity. Here, the same controller $G_{C1}(s)$ is used for the d and q rotor current control because of similar electrical dynamics in those axes.

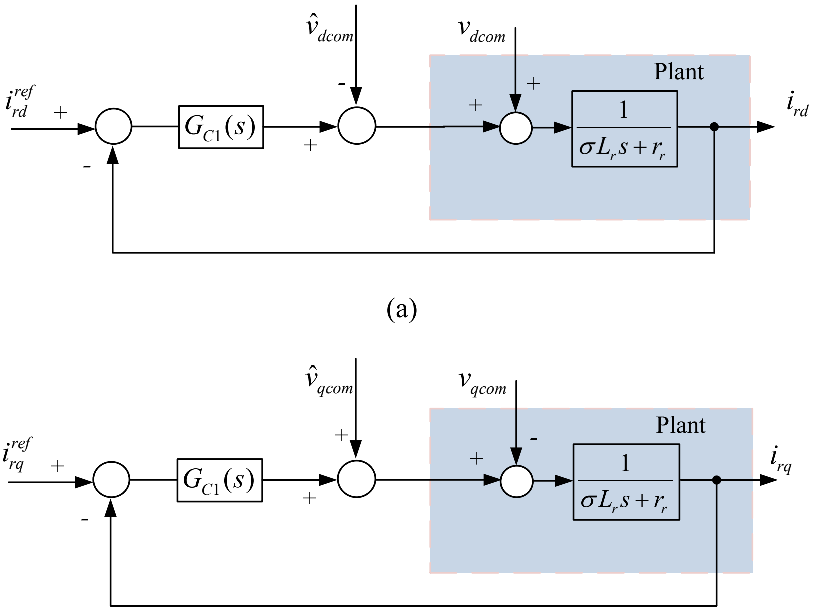

(a)

(b)

Fig. 4-2 Control block diagram of inner current control loops. (a) d-axis current control, and (b) q-axis current control.

With help of dynamic equations given in (4.16) and control laws expressed in (4.21), the overall control diagram is constructed as in Fig. 4-2. The aim of the controller $G_{C1}(s)$ is to regulate current against the disturbance in the feed forward path. While deriving the control law of control block $G_{C1}(s)$, we assume that the dc-link voltage (V_{dc}) is at the rated value (so that the rotor voltage is written as $v_{rd} = V_{dc}^{ref} d_{1d}$) and ω_r varies slowly with compare to current (in fact ω_r is regulated by outer q-axis control loops, so for the inner loops it is assumed as constant). Consequently, the model can be linearized at the nominal values ($V_{dc} = V_{dc}^{rated}$ and $\omega_r = \omega_r^{rated}$) and the controller is designed using the IMC concept. With the help of the expression in (4.8), the $G_{C1}(s)$ is reduced to a proportional-integral controller defined as

$$G_{C1}(s) = \frac{1}{\alpha_{1c} s}(\sigma L_r s + r_r)\,, \tag{4.22}$$

where α_{1c} is the desired time constant of the close loop system, and its value is selected as 10 ms to assist the fast tracking of the current. The reference value i_{rq}^{ref} in (4.21) is set from the outer speed control loop (to be discussed later), whereas the setting of i_{rd}^{ref} is guided by (4.19). For the operation of an induction machine in the generating mode, the reactive power is always drawn by the machine from the system. If the reactive component of rotor current is zero (i_{rd} =0), the stator reactive power (Q_s) assumes a negative value, meaning that stator absorbs the required reactive power from bus #1, in which case Q_s is drawn from VSC2 (keeping the operation of the microgrid at unit power factor mode). This may not be a desired condition as VSC2 would be overloaded. The reactive power demand for the generator can be supplied by VSC1 if i_{rd} is imposed such that

$$i_{rd}^{ref} = \psi_{sd} / L_m\,. \tag{4.23}$$

While setting the reference current by (4.23), the kVA rating of VSC1 is to be increased for a given value of generating torque. In this study, Q_s is nullified through the rotor current (i_{rd}) to reserve the kVA capacity of the grid-side converter (VSC2) for storage management.

4.2.2 Speed control of wind turbine

There are two modes of rotor speed control with a variable speed wind turbine. The first mode is in the region of lower wind speeds, in which the set-point speed is varied with wind speed (known as maximum power point tracking) and speed regulation is performed by the rotor-side converter by varying the power output. On the other hand, the second mode is in the region of higher wind speeds, in which the set-point of rotor speed is kept constant and the rotor speed is regulated via pitching the rotor blade until the output power reduces to the rated value. Following paragraphs explain the control approach for each scheme.

(a) Speed control through rotor-side converter

The rotor speed control of is related to the outer control loop of the rotor-side converter shown in Fig. 4-3, in which the deviation in the rotor speed caused by the disturbance torque (the mechanical torque) is nullified by employing the compensator $G_{C2}(s)$. The controller action generates the set-point electromagnetic torque (T_{em}^{ref}) given by

$$T_{em}^{ref} = (\omega_r^{ref} - \omega_r)G_{C2}(s), \tag{4.24}$$

where ω_r^{ref} is the command reference of rotor speed set by the maximum power point tracking (MPPT) technique. Noting that $T_{em} = 0.75 n_p \psi_{sd} i_{rq}$ (from (4.18)) and the stator flux (ψ_{sd}) is fairly constant, the controller output generates q-axis set-point current (i_{rq}^{ref}) consequently.

For the speed control scheme, we set the time constant α_{1c} of the inner current dynamics sufficiently smaller than the speed dynamics, so that the current control loop can be assumed as the unit gain, while looking from the outer loop. Considering the mechanical dynamics of the WTGS given in (4.16), the transfer function from T_{em}^{ref} to ω_r becomes the linear function, given by

$$\frac{\omega_r(s)}{T_{em}^{ref}(s)} = \frac{1}{sJ_m + D_m}. \tag{4.25}$$

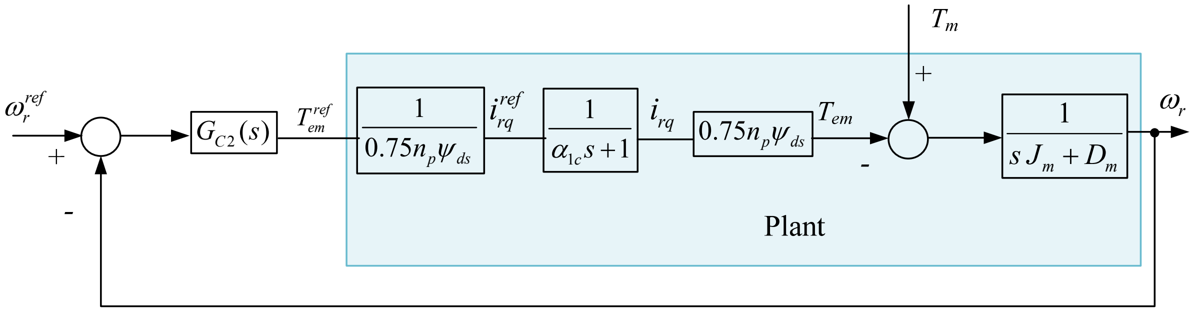

Fig. 4-3 Block diagram of speed control loop.

It should be noted that the IMC method described in (4.8) would be insufficient to set the parameters for $G_{C2}(s)$, as the time constant of the plant (J_m/D_m) is quite larger than the time constant of the associated filter $L(s)$. Therefore, the improved IMC is utilized for tuning. From (4.13) with n=2, the expression for $G_{C2}(s)$ can be derived as

$$G_{C2}(s) = \frac{(1+s\gamma_{2c})D_m}{s\left[(\alpha_{2c}s+1)^2-(\gamma_{2c}+1)\right]}(sJ_m/D_m+1).$$

Rearranging, we get

$$G_{C2}(s) = \frac{(1+s\gamma_{2c})D_m}{s(2\alpha_{2c}-\gamma_{2c})\left(\dfrac{\alpha_{2c}^2}{2\alpha_{2c}-\gamma_{2c}}s+1\right)}(s\tau_{tg}+1),\ \ \tau_{tg}=J_m/D_m. \tag{4.26}$$

Here, α_{2c} and γ_{2c} are the constant parameters to be set for the IMC. To accomplish the fast disturbance rejection, we set $\tau_{tg}=\alpha_{2c}^2/(2\alpha_{2c}-\gamma_{2c})$, which gives

$$G_{C2}(s)=\frac{(1+s\gamma_{2c})D_m}{s(2\alpha_{2c}-\gamma_{2c})}=\frac{D_m}{s(2\alpha_{2c}-\gamma_{2c})}+\frac{\gamma_{2c}D_m}{(2\alpha_{2c}-\gamma_{2c})}. \tag{4.27}$$

Finaly, the output response can be written as

$$\omega_r(s)=\frac{(\gamma_{2c}s+1)}{(\alpha_{2c}s+1)^2}\omega_r^{ref}(s)+\frac{D_m(2\alpha_{2c}-\gamma_{2c})s}{(\alpha_{2c}s+1)^2}T_m(s). \tag{4.28}$$

Thus, by the choice of suitable value of α_{2c} and γ_{2c}, we can eliminate the long settling time of the rotor angular velocity due to the disturbance torque, irrespective of the disturbance transfer function, $G_d(s)$. In this case, the time constant of the speed control loop is selected as 0.7 s considering the slower mechanical dynamics of the rotor, which leads to setting $\gamma_{2c}=1.35\,\text{s}$.

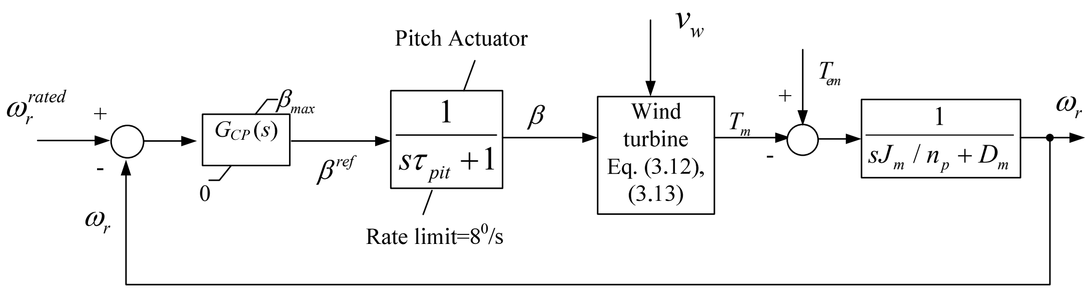

Fig. 4-4 Block diagram of rotor pitch angle control.

(b) Speed regulation through pitch angle control

As discussed earlier, the pitch angle control is operated in high wind speeds. In those circumstances, the rotor speed can no longer be controlled by increasing the generated power, as this would lead to overloading the generator and the converter. Once maximum rating of the generator/converter is reached, the pitch angle is increased; which in turn reduces the power conversion coefficient (C_P), and consequently the excess power is spilled away from the turbine. It should be noted that during this period, the set-point torque for the variable speed drive (VSC1) reached to its upper limit due to saturation, so it cannot provide the speed regulation.

The control block diagram for the pitch control scheme is shown in Fig. 4-4. The wind turbine and generator model acts as the plant for the system represented by (3.12) and (3.13) (chapter three), in which a compensator is employed for the speed regulation to generate the set-point value of pitch angle (β^{ref}), given by [7],

$$\beta^{ref} = G_{CP}(s)(\omega_r^{rated} - \omega_r), \tag{4.29}$$

where $G_{CP}(s)$ denotes the compensator transfer function. To put the blades into the necessary position, pitch servos are employed as actuators which may be hydraulic or electrical systems. Because of large mass of the rotor, the actuator cannot regulate the rotor speed quickly. Therefore, the actuator is represented by an integral function, and subsequently the transfer function for the pitch angle control loop becomes the first order delay (with time constant, τ_{pit}) and a pitching rate limiter [7]. As a result, the regulated pitch angle alters the power conversion coefficient (C_P) till the turbine power output equals to the rated value.

To design the compensator $G_{CP}(s)$ for the rotor speed control, a PID controller is selected with the parameters as suggested in [7, 8], represented as

$$G_{CP}(s) = k_{pit}\left(1 + \frac{1}{T_{i,pit}s} + T_{d,pit}\frac{s}{1 + 0.1T_{d,pit}s}\right),$$

where $k_{pit}, T_{i,pit}$, and $T_{d,pit}$ are the control parameters of $G_{CP}(s)$.

4.2.3 Maximum power point tracking scheme

To capture the maximum power from the wind turbine, it is necessary to alter the set-point of the rotor angular speed according to the variation in wind speed. The conceptual framework for setting optimum value of rotor speed, referred to maximum power point tracking (MPPT) technique, can be understood from Fig 3.3(b). It can be observed that the steady-state maximum power from the turbine is obtained when power conversion coefficient is at its maximum value ($C_{P\text{-max}}$). This can be achieved by setting the rotor speed proportional to the measured value of wind speed as

$$\omega_r^{opt} = \frac{\lambda_{tip}^{opt}}{r_T} v_w, \tag{4.30}$$

where ω_r^{opt} is the optimum rotor speed related to the maximum power output from wind turbine. From (4.30), we note that ω_r^{opt} is set by direct measuring of wind speed, which may not be always desirable. To avoid the direct measurement of wind speed, it is modified to set the rotor speed corresponding to the measured value of the active power from the generator (P_{ig}), with copper loss included, as [9]

$$\left.\begin{aligned} P_{ig} &= k_{opt}(\omega_r^{opt})^3, \qquad k_{opt} = \frac{0.5\rho A r_T^3 c_{P-\max}}{(\lambda_{tip}^{opt})^3} \\ \omega_r^{opt} &= \sqrt[3]{\frac{P_{ig}}{k_{opt}}} \end{aligned}\right\}. \tag{4.31}$$

Since k_{opt} is a constant parameter for the turbine, only measuring the transferred power allows calculating the reference speed which, in turn, seeks the optimal operation. This speed can be imposed in the controller scheme, and optimum operation can be achieved after a few computational iterations following the dynamics, $(1+s\gamma_{2c})/(1+s\alpha_{2c})^2$.

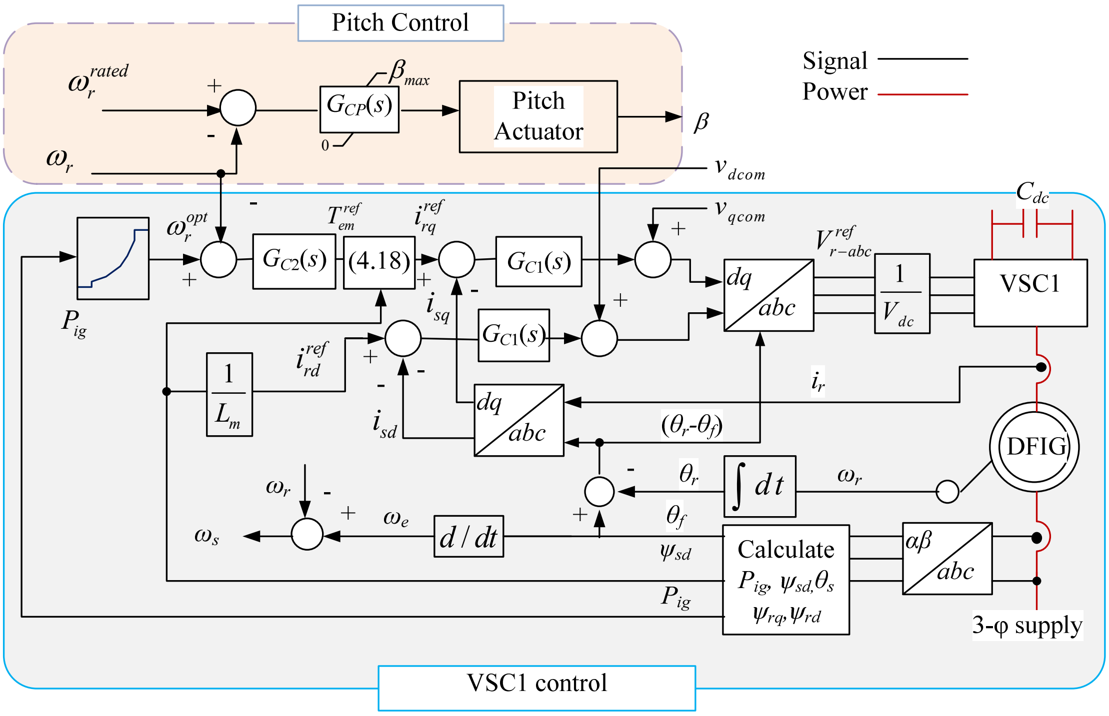

Fig. 4-5 Block diagram of overall control scheme for the DFIG.

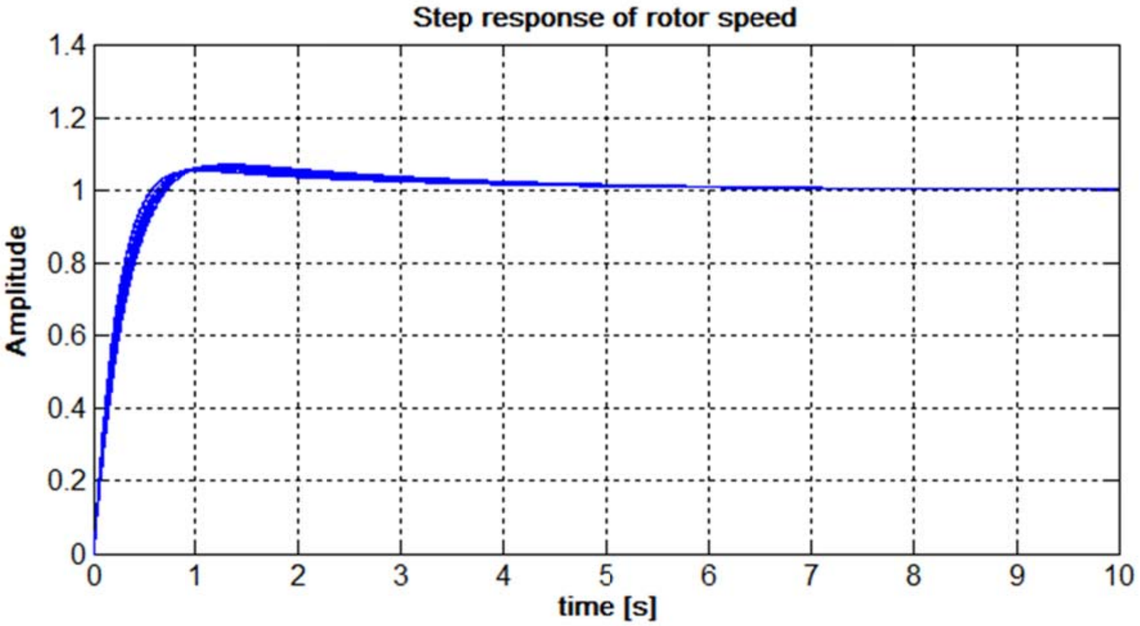

(a)

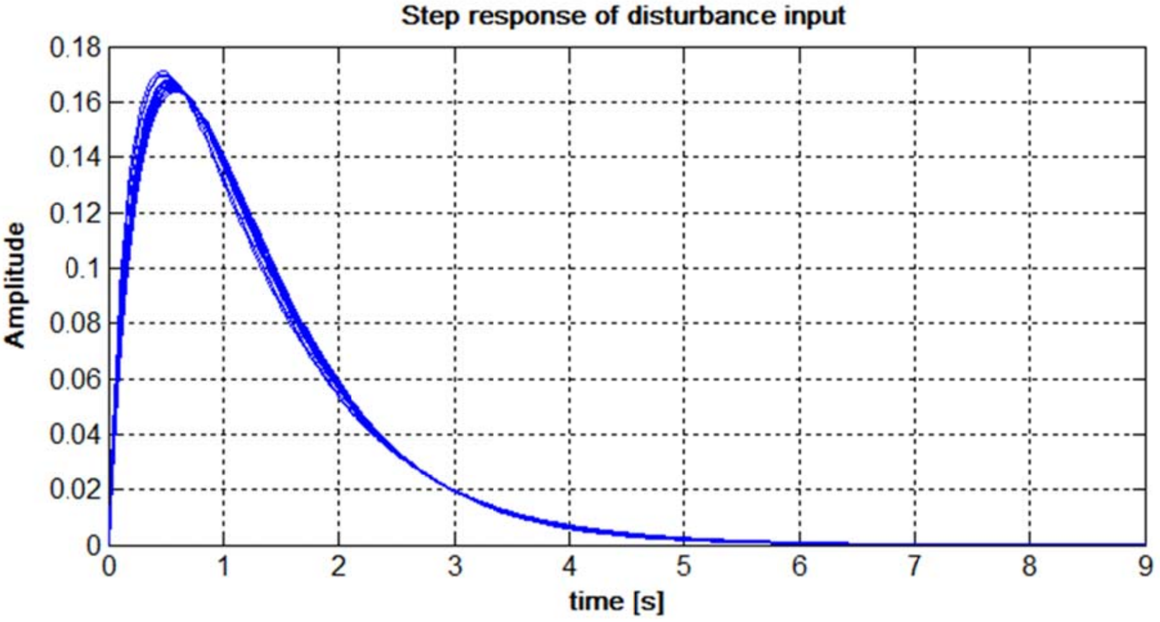

(b)

Fig. 4-6 Output responses of control block shown in Fig. 4-3 with ±20% variation of plant parameters: r_r, L_m, L_r, D_m *and* J_m . (a) Step command input, and (b) step disturbance input.

4.2.4 Overall block diagram and test of controller

Fig. 4-5 shows the overall control block diagram of the system illustrating how the individual control schemes fit into the plant. For the VSC1 control action, the input is the electrical power measured from the generator output terminal. Based upon the measured power, the command speed is calculated using the MPPT technique. The set value of command torque (T_{em}^{ref}) is calculated either by the outer speed control loop (when $\omega_r^{opt} < \omega_r^{rated}$) or set as T_{em}^{rated} (when $\omega_r^{opt} \geq \omega_r^{rated}$), and then the set value of the rotor q-axis current (i_{rq}^{ref}) is deduced. Likewise, the rotor d-axis current (i_{rd}^{ref}) is calculated from the measured value of stator flux. The current control loop generates duty cycles for the converter that produces the required rotor voltage space vector ($\mathbf{v}_r$) at the terminal of VSC1. In case when $\omega_r^{opt} \geq \omega_r^{rated}$ or $P_{ig} \geq P_{ig}^{rated}$, the pitch angle controller is guided to generate the desired value of pitch angle (β). This, in turn, adjusts C_P below its optimum value, so that the generated power can be kept at its nominal value.

To check the applicability of controllers $G_{C1}(s)$ and $G_{C2}(s)$ in the block diagram of Fig. 4-2 and 4-3, a number of tests are performed. The tests include the robustness of the designed controllers under the variation of the plant parameters. Due to lack of real data for the parameters uncertainties, this dissertation assumes $\pm 20\%$ variation of the parameters from their respective nominal values. The dynamic uncertainty is, however, not included in the analysis. The performance test includes

- capability of reference point tracking,
- disturbance rejection, and
- wide stability margin.

Fig. 4-6 shows the output response (ω_r) under the unit step command input (ω_r^{opt}) and disturbance input (T_m). With uncertainty of plant parameters (J_m, L_m, L_r, r_r and D_m) specified above, there is minor variation in rise time with the step input of ω_r^{opt} in Fig. 4-6(a). Note that the desired value of settling time (5 s) is achieved with zero steady state error for all ranges of parameters' variation. Similarly, the disturbance rejection is also observed with similar settling time, as that of reference input tracking, thanks to the modified IMC control (see Fig. 4-6(b)). It may be noted that the response curve shows the band between the most optimistic and pessimistic response. At the boundary, the fastest and the slowest rise times correspond to

$min\{J_m, L_m, L_r\} \cap max\{r_r, D_m\}$ and $max\{J_m, L_m, L_r\} \cap min\{r_r, D_m\}$, respectively. For the intermediate responses, the curves are related to the different combinations of the parameters. Since we are concerned with the values in the boundaries, the determination of each combination related to the intermediate responses are of less important. Likewise, Fig. 4-7 depicts the Bode plot of the tuned system. Clearly, the plot has wide stability margin (75^{o} phase margin) even under the most pessimistic plant model. These figures validate the desired robust performances of the controllers under the assumed level of parameters' uncertainty.

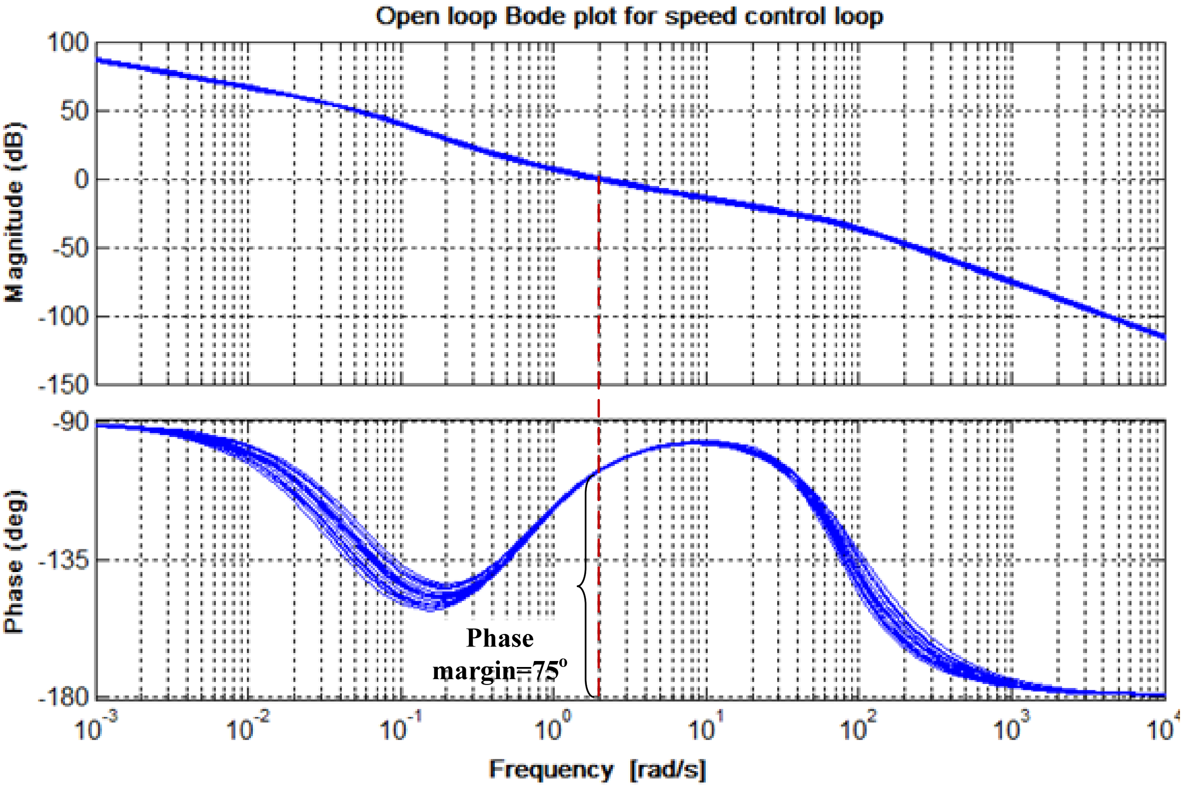

Fig. 4-7 Bode plot of control block shown in Fig. 4-3 with ±20% variation of plant parameters: r_r, L_m, L_r, D_m and J_m.

4.3 Dedicated Energy Storage System Controller

The objectives of the DESS controller are to generate the actuating signals for the dc-dc converters, DC1 and DC2. The converter DC2 is assigned for regulating the dc-link bus voltage in the expense of drawing (delivering) compensating current, while the converter DC1 forces to share the compensating current from the UC and FC/ELZ units in the expense of consuming (generating) H_2. Fig. 3-21 (chapter three) provides the guideline for selecting control behavior. The system has nonlinear dynamics with two command inputs: duty cycle for DC1 switches and phase shift angle for DC2 (d_2/d_3, δ), a disturbance current input (I_{dstb}), and number of outputs. By observing the block diagram following information is noted.

- In the DC2/dc-link bus system block, the dynamics of the UC voltage (V_{uc}) is quite slow in compare to the dynamics of the phase shift variable (δ).
- The DC2 input current (I_i) appears as the disturbance input for the FC/ELZ/UC/DC1 system.

These properties lead to decoupling the DESS into two SISO blocks, simplifying the control design. The control schemes associated with these units are discussed in the following subsections.

4.3.1 Control approach for fuel cell side dc-dc converter

The converter DC1 is an actuator that assists in sharing the desired current in a manner that transient and steady-state parts are supplied by the UC and FC/ELZ, respectively. This can be achieved by implementing a control scheme in two loops, in which the inner one is employed for current regulation and the outer one is designated for the UC voltage regulation. The plant associated with the DC1 control action is the FC/ELZ/UC/DC1 system shown in Fig. 3-21 (chapter three), in which the controller blocks $G_{C3}(s)$ and $G_{C4}(s)$ are augmented to achieve the desired closed loop response. The resultant control block diagram for the system is depicted in Fig. 4-8. Here the blocks $G_{C3}(s)$ and $G_{C4}(s)$ represent the controllers for inner current control loop and outer voltage control loop, respectively.

While designing the inner controller, $G_{C3}(s)$, the dynamics of system given in the FC/ELZ/DC1 part has to be dealt with. Since the system has nonlinearity as represented in (3.58), it is linearized around the stable operating point to investigate the control approach. The dynamic equations along with other related algebraic equations are linearized at the nominal operating point of the SOFC (rated value of fuel cell current, $I_{dc1} = I_{dc1}^{rated}$; rated value of voltage, $V_{fc} = V_{fc}^{rated}$; and nominal value of duty cycle for switches: $d_2, d_3 = D_2, D_3$). The entire pole and zeros of the linearized system lie on the left-half of the complex plane, in which the dominant pole-zeros are depicted in Fig. 4-9. Clearly, the system is stable, but it has a sluggish dynamics due to the poles near -0.2 (state represented by fuel regulation dynamics). This leads to selecting a proportional-integral-derivative (PID) controller for tracking the current. Since the response of the current control loop should be fast, we specify the bandwidth and phase margin as 200 rad/s and 85 degree respectively. The resultant close loop step response plot with current as the reference input is depicted in Fig. 4-10. It can be observed that, the control loop has fast current tracking property thanks to the applied PID controller.

In the fuel cell model, the states related to the partial pressure dynamics do not have the provision of feedback regulation. The presence of these non-controllable states having sluggish dynamics puts the constraints of selecting the reference current for the FC/ELZ in a way that the current dynamics should not have smaller time constant than that of the dominant poles. Otherwise, it may result fuel starvation in the FC. This demands a high farad rating of the UC which takes care of the transient part until the steady state current flows through the FC/ELZ part. From (3.52), the output current from DC1 (I_{dc1}) is proportional to the FC or ELZ current (I_{fc} or I_{elz}), so it would be convenient to control I_{dc1} alone. For this, a reference output current for DC1 is generated as

$$I_{dc1}^{ref} = \frac{I_i}{T_d s + 1} + G_{C4}(s)(V_{uc}^{ref} - V_{uc}) . \tag{4.32}$$

The first part of (4.32) ensures that only slow varying and the steady state part of current flows through the FC/ELZ. The current rise time is decided by the consideration of the SOFC parameters, the maximum value of the fuel cell current ramp rate and time constant of the fuel regulation block. The second term is associated with the outer control loop that regulates the UC voltage. The design of the controller $G_{C4}(s)$ is based upon the allowed range of V_{uc}. This, in turn, is decided by the minimum operating voltage for the SOFC ($V_{fc,min}$), the maximum allowable voltage for the ELZ ($V_{elz,max}$) and the capacitance of the UC (C_{uc}). In this study, the range of V_{uc} is taken from 225 to 275 V with its nominal value at 250V. By doing so, it subjects the rated UC voltage below $V_{fc,min}$, ensuring the desired buck/boost operation for the DC1 converter. By these considerations, $G_{C4}(s)$ is represented by a PID controller to obtain the close loop step response having settling time of 20 s and the maximum overshoot of about 5% with a satisfactory stability margin.

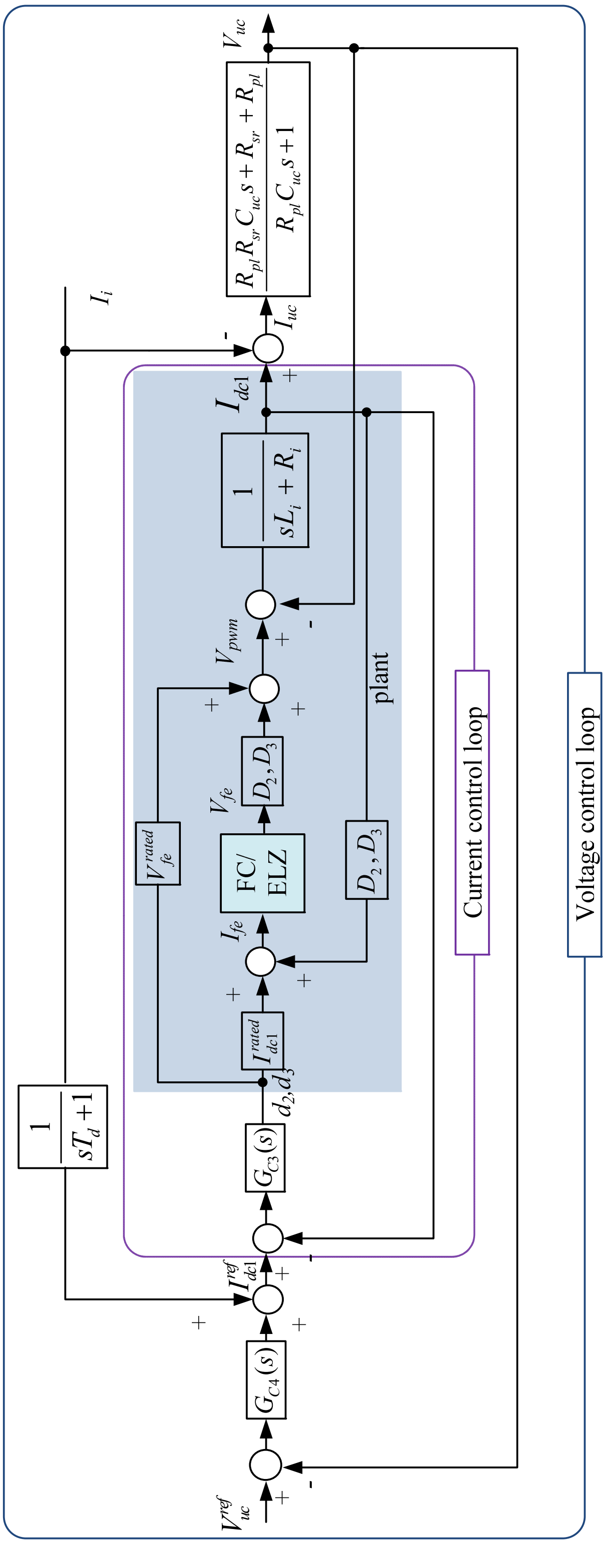

Fig. 4-8 Control block diagram of FC/ELZ/UC/DC1 system.

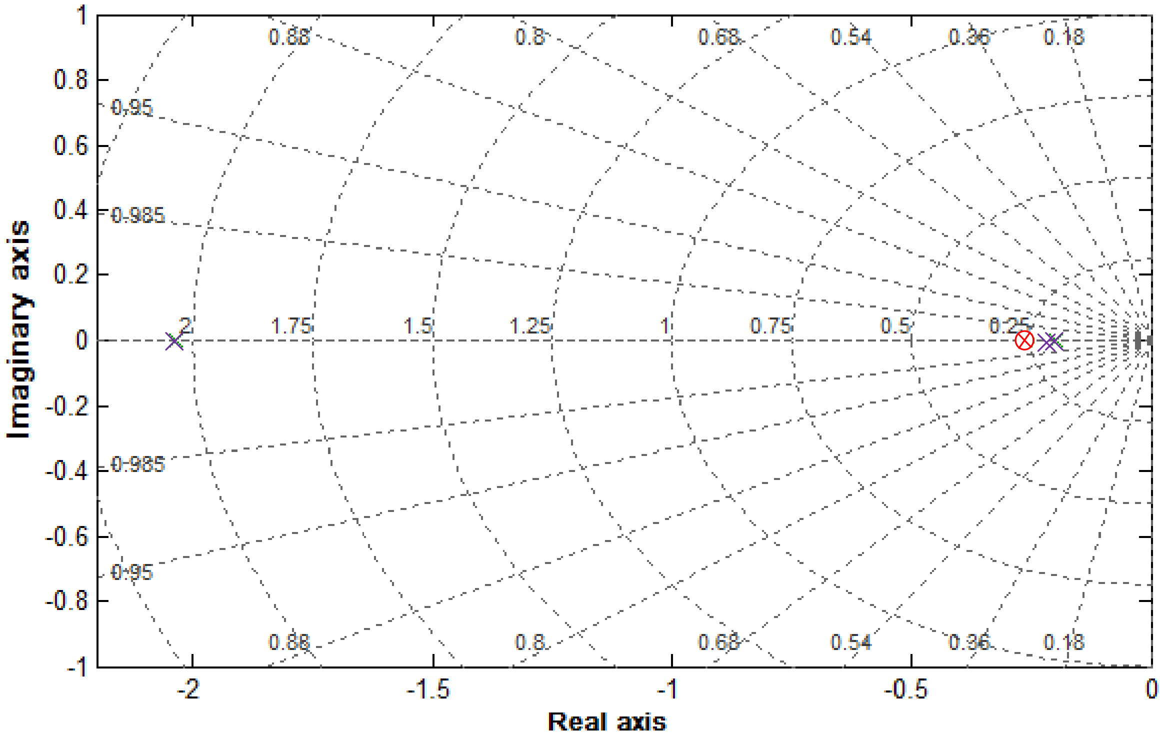

Fig. 4-9 Pole zero plot of FC/ELZ/DC1 system. "zero-mark" and "cross-mark" are set for zero and pole respectively. The number in the radial line represents the cosine of angle between the radial line and the negative real axis.

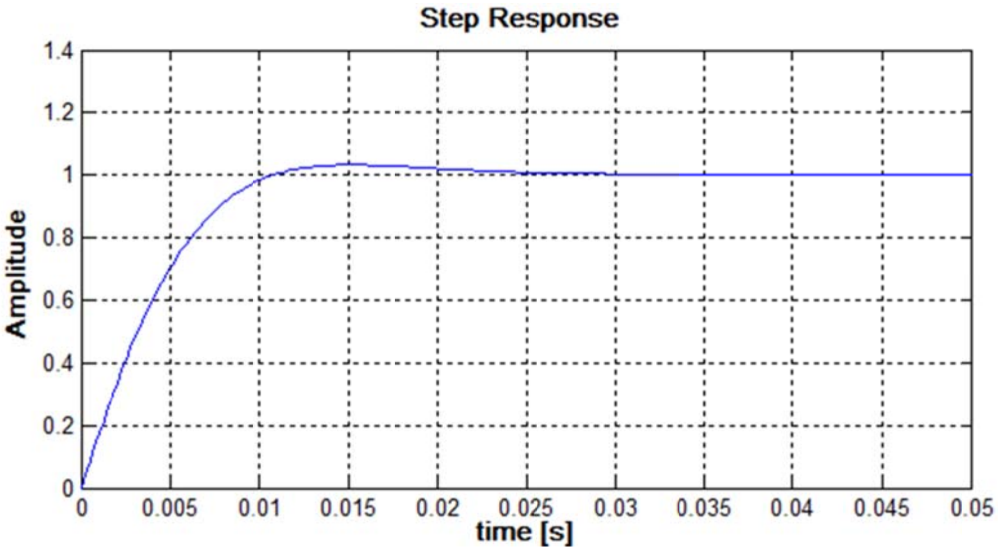

Fig. 4-10 Step response of the inner current control loop.

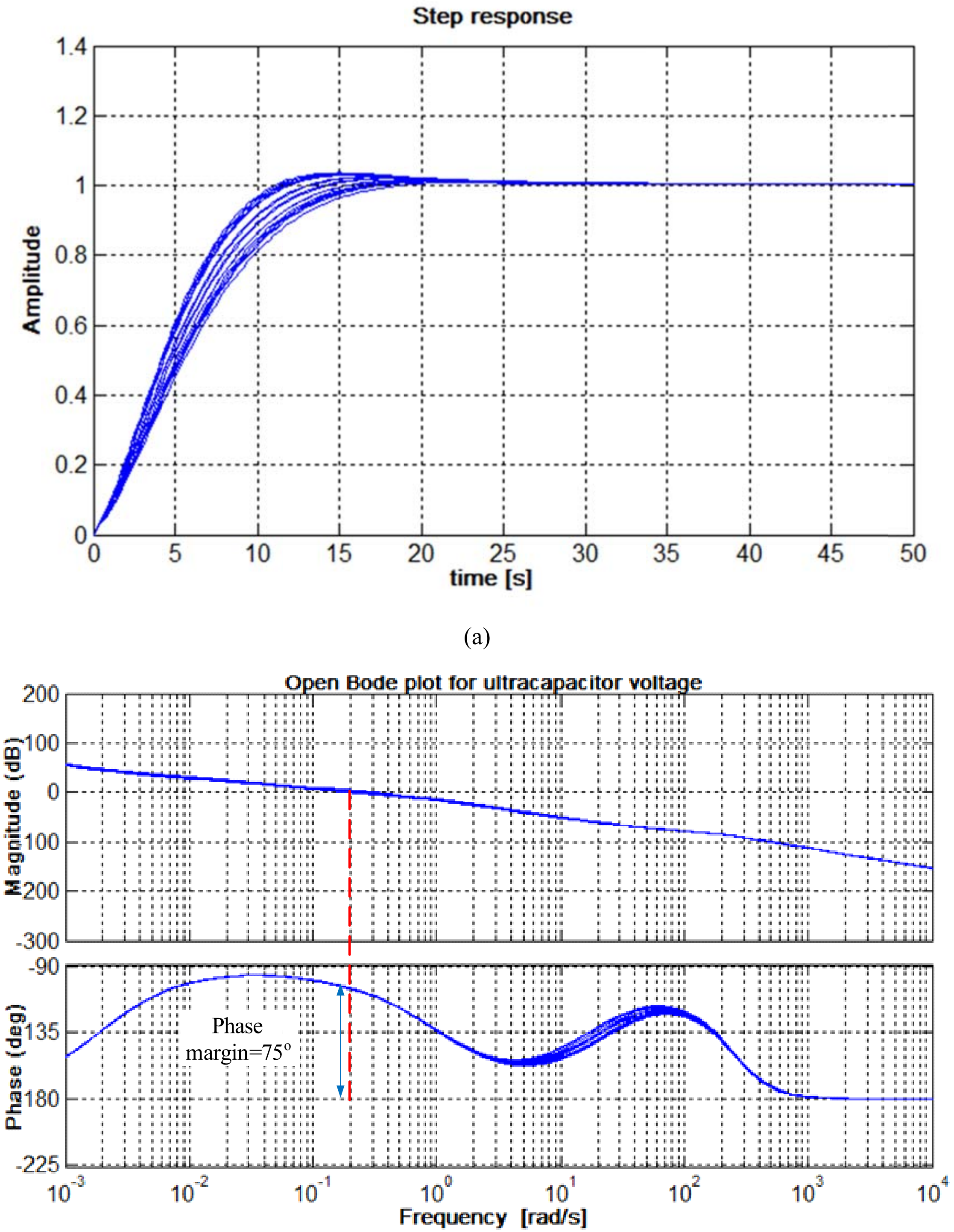

(a)

(b)

Fig. 4-11 Responses of DC1 controller with ±20% variation of plant parameters: T_d, C_{fc}, R_i and L_i from their nominal values. (a) Unit step response plot, and (b) frequency response plot.

Test of controller

In order to test the applicability of the proposed control actions, the control block diagram is subjected to various tests, by considering the uncertainties of the plant parameters (T_d, L_i, C_{uc}, R_i and R_{sr}) as $\pm 20\%$ with their nominal values. Fig. 4-11(a) represents the step response plot for the outermost control loop given in Fig 4-8. It can be observed that the controller provides good tracking of the reference input against the uncertainties of the plant parameters. The effect of uncertainties is on rise time, but the settling time and steady state responses are not affected. It is also notable that the response curves show the band between the most optimistic and pessimistic responses. On the boundary, the fastest rise time and the slowest rise time correspond to the $min\{T_d, L_i, C_{uc}\} \bigcap max\{R_i, R_{sr}\}$ and $max\{T_d, L_i, C_{uc}\} \bigcap min\{R_i, R_{sr}\}$, respectively. The intermediate response curves, on the other hand, are related to the different combinations of the parameters.

In order to test the stability margin of the system over the range of parameter uncertainties, the open loop *Bode plot* is also presented in Fig. 4-11(b). It is shown that the controller provides wide stability margin of about 75^{o} even in the assumed pessimistic scenario. These control parameters are transferred to the original large signal model to test the system under various operating conditions.

4.3.2 Control approach for the isolating dc-dc converter

The control block for the isolating dc-dc converter is associated with the *DC2/dc-link bus system* (illustrated in Fig. 3-21), having a simple first order linear system. Since the time constant of the UC terminal voltage (V_{uc}) is very large with compared to the dc-link voltage (V_{dc}), the former varies very slowly and assumed as a constant quantity while designing the V_{dc} control loop. Thus, by linearizing at the rated UC voltage (V_{uc}^{ref}), the control block diagram is constructed as in Fig. 4-12(a). The controller block, $G_{C5}(s)$ is employed here for the regulation of V_{dc} at the designated value, against the disturbance current (I_{dstb}) imposed from the dc-load, VSC1 and VSC2. In this case, the controller $G_{C5}(s)$ needs to have good disturbance rejection, as the command input (V_{dc}^{ref}) is the constant quantity. This is achieved by a PID controller, in which the settling time of the close loop step input is chosen about 0.4 s. Clearly, the desired disturbance response of the controller is achieved for the given choice of the parameters (see Fig. 4-12 (b)), and consequently the fast voltage regulation is achieved.

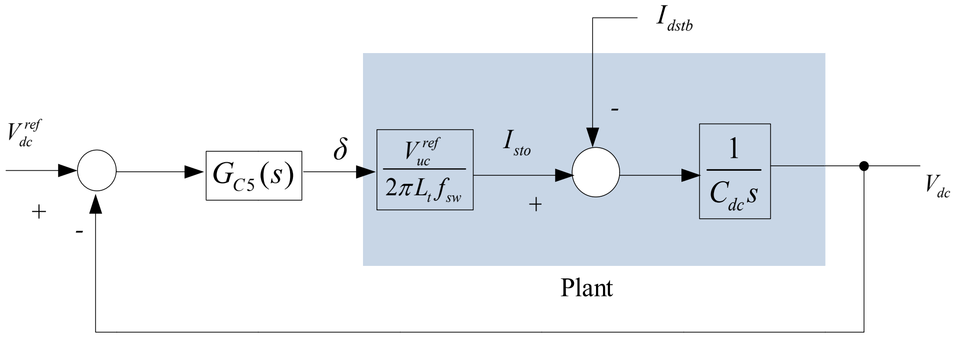

(a)

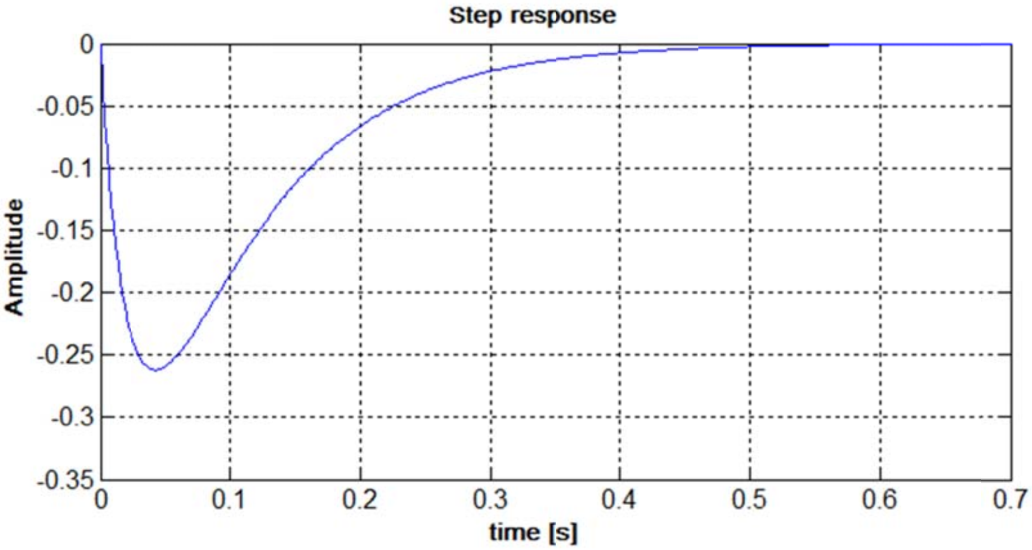

(b)

Fig. 4-12 Control scheme for the DC2/dc-link bus system. (a) Block diagram , and (b) step response of the disturbance input.

4.4 Line-Side Converter Control

The controller employed with the line-side converter (VSC2) has wide range of control actions. In case of a line converter operation when the DESS is not connected, main objectives remain to inject available power of wind power to the grid by regulating the dc-link voltage and maintain the desired power factor, which means to operate in a non-dispathable mode. However, by incorporating the DESS, it can control the frequency and voltage of the PCC bus (during islanded mode) or regulate the dispatchable tie-line power (in grid interconnected mode). Therefore, the control action should be designed to operate in both modes like a traditional excitation and governor controlled synchronous generator. To accomplish the objective, the subsystem is designed to mimic the conventional excitation and governor control schemes system, by utilizing the artificial frequency-active power and voltage-reactive power droop concepts [10],[11].

4.4.1 Frequency and active power control

Basic idea behind the frequency control is to introduce an artificial droop such that any increase in the power demand decreases the system frequency, and vice versa. The expression of frequency-power droop and phase angle of terminal voltage can be written as

$$\omega_e^{ref} = \omega_0 + m(P_2^{ref} - P_2), \quad \theta_e = \int \omega_e^{ref} dt. \tag{4.33}$$

Here, P_2 is the active power output from the inverter, m is the droop coefficient, ω_0 is the nominal value of angular frequency of terminal voltage. Likewise, ω_e^{ref} and θ_e are the reference frequency and the phase angle of VSC2 terminal voltage, resepctively.

From Fig. 2.6(a) (see chapter two), the impedance between the terminal of inverter and bus #2 being inductive in nature ($2\pi L_f >> R_f$), the phase angle and the voltage drop become relatively linear with the injected active and reactive power, respectively, as

$$\left. P_2 \approx \frac{E_2 V_2}{X_f}\theta_e, \quad Q_2 \approx \frac{E_2}{X_f}\left(E_2 - V_2\right), \; X_f = \omega_e L_f \right\} , \tag{4.34}$$

where Q_2 is the reactive power flow from VSC2. The other variables and parameters are defined in Fig. 2.6(a). From (4.33) and (4.34), we have

$$\frac{d\theta_e}{dt} = -\frac{mE_2V_2}{X_f}\theta_e + \omega_0 + mP_2^{ref}. \tag{4.35}$$

The value of P_2^{ref} is derived from the outer active power management loop (to be discussed in the next section). Equaion (4.35) illustrates that the power injecting to bus #2 with droop of the inverter frequency resembles the governor and the inertia characteristics of traditional generators and provides a degree of negative feedback, aiding the smooth frequency regulation. This phenomenon is also illustrated in Fig. 4-13. The frequency becomes the nominal value only when the desired and the actual active power flow are equal. Otherwise, it deviates from the nominal value as decided by (4.33). The integral of this frequency becomes the phase shift (θ_e) that controls the active power flow. At steady state, the phase angle corresponds to $(mP_2^{ref} + \omega_0)X_f / mE_2V_2$ following the dynamics. Consequently, the power injected from VSC2 becomes

$$P_2 = P_2^{ref} + \omega_0 / m, \tag{4.36}$$

where the droop coeffiecient is defined as

$$\frac{\omega_0 - \omega_{fullload}}{P_2^{rated}} = m. \tag{4.37}$$

Here, $\omega_{fullload}$ is the full-load frequency of VSC2 terminal voltage (E_2). The selection of m is based upon the allowable range of the frequency deviation from no-load to full loaded condition. In case of an inverter interfaced system, m is usually set to 2% [12]. Alternately, it decides the tracking error by ω_0 / m, which is nullified later by the secondary frequency control.

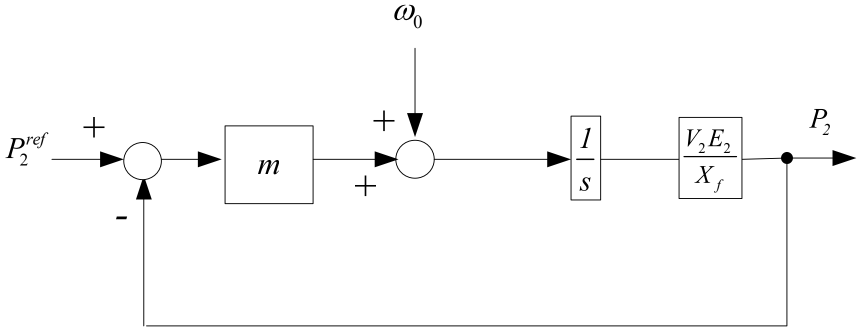

Fig. 4-13 Block diagram of *P*/*f* control.

4.4.2 Voltage control

The concept of voltage and reactive power regulation (*V/Q control*) is similar to the traditional excitation control with increased flexibility thanks to the converter application. Here, the voltage control is exercised in the rotating *d-q* coordinate system, in which the output voltage magnitude reference aligned with the *d*-axis of the inverter reference frame as presented as

$$v_{2d}^{ref} = V_2, \quad v_{2q}^{ref} = 0; \tag{4.38}$$

where, v_{2d} and v_{2q} are respectively the *d* and *q* axis components of v_2. The command value of voltage (v_{2d}^{ref}) is derived from the outer *V/Q management* loop (to be discussed later). It is notable that by forcing v_{2q} to zero, the angle θ_e generated from the frequency control action becomes the phase shift between E_2 and V_2, and thereby making P_2 proportional to θ_e. There are two cascaded control loops for both *d* and *q* axes. The outer loops regulate the ac bus voltage and provide the reference signals for the inner current loops. The purpose of the inner current control is to decouple the *d-q* axis variables, reject high frequency disturbances and provide sufficient damping for the output filter.

The design of inner current control is based upon the dynamic given in (3.27) which are rewritten as

$$\left.\begin{aligned}\mathbf{e}_2 &= R_f\mathbf{i}_2 + L_f d\mathbf{i}_2/dt - j\omega_e L_f\mathbf{i}_2 + \mathbf{v}_2\\ \mathbf{v}_2 &= R_{th}\mathbf{i}_2 + L_{th}d\mathbf{i}_2/dt + \mathbf{v}_{th}\end{aligned}\right\}. \tag{4.39}$$

We note that the control law for the inner current loop is similar to (4.21), where the cross-coupling voltage drop terms are compensated. The control law is defined as

$$\mathbf{e}_2 = G_{C6}(s)(\mathbf{i}_2^{ref} - \mathbf{i}_2)k_{pwmi} - j\omega_e L_f\mathbf{i}_2 + \hat{\mathbf{v}}_2, \tag{4.40}$$

where $G_{C6}(s)$ is the transfer function of the controller; and k_{pwmi} is the gain of the pulse width modulation (PWM) generator, which is considered as the constant parameter neglecting the high frequency dynamics of the PWM logic. It is because the rise time of a PWM generator gain is in the range of microseconds whereas the rise time for the current control loop is in the range of milliseconds. The parameters for the controller is determined using the IMC defined in (4.8). In this case, $G_{C6}(s)$ is designed as

$$G_{G6}(s) = \frac{1}{k_{pwmi}\alpha_{6c}s}(sL_f + R_f) = \frac{\hat{L}_f}{k_{pwmi}\alpha_{6c}} + \frac{\hat{R}_f}{k_{pwmi}\alpha_{6c}s}. \tag{4.41}$$

Consequently, the current is tracked quickly following the first order dynamics with bandwidth $(1/\alpha_{6c})$ as

$$\mathbf{i}_2 = \frac{1}{\alpha_{6c}s + 1}\mathbf{i}^{ref}. \tag{4.42}$$

Since we desire fast current tracking for the inner loop, we set the value of bandwidth as 100 rad/s.

The design of the outer voltage control loop is relatively slower than the current control loop, for which we specify its band width ten times smaller than the inner one ($\alpha_{7c} = 10\alpha_{6c}$). This can be achieved by employing $G_{C7}(s)$ with the voltage error signal, producing the current reference signal as

$$\mathbf{i}_2^{ref} = (\mathbf{v}_2^{ref} - \hat{\mathbf{v}}_2) G_{C7}(s). \tag{4.43}$$

For voltage control loop, the inner current loop can be approximated as a simple delay block given by (4.42) to simplify the analysis, without losing the accuracy [13]. Consequently, the IMC scheme in (4.7) with the filter $L(s) = 1/(s\alpha_{7c} + 1)$, gives the desired controller $G_{C7}(s)$ as

$$G_{C7}(s) = \frac{1}{\alpha_{7c} s} \left(\frac{s\alpha_{6c} + 1}{s\hat{L}' + \hat{R}'} \right). \tag{4.44}$$

The overall control block, including the inner and the outer control loops, is depicted in Fig. 4-14. The plant is constructed from (4.39), (4.40) and (4.43), in which the controllers are defined by (4.41) and (4.44). With the value of designated parameters, the *unit step response* and *Bode plot* for the outer voltage tracking loops are plotted and depicted in Fig. 4-15. While plotting the response curves, the robustness of the controller is checked against the variation of parameters (L_f, R_f, L_{th}, R_{th}), around their nominal values. It can be seen that utilizing the proposed control approach, the overall control demonstrates the desired performances (set-point tracking, stability, robustness), against the assumed level of the parameters' uncertainty.

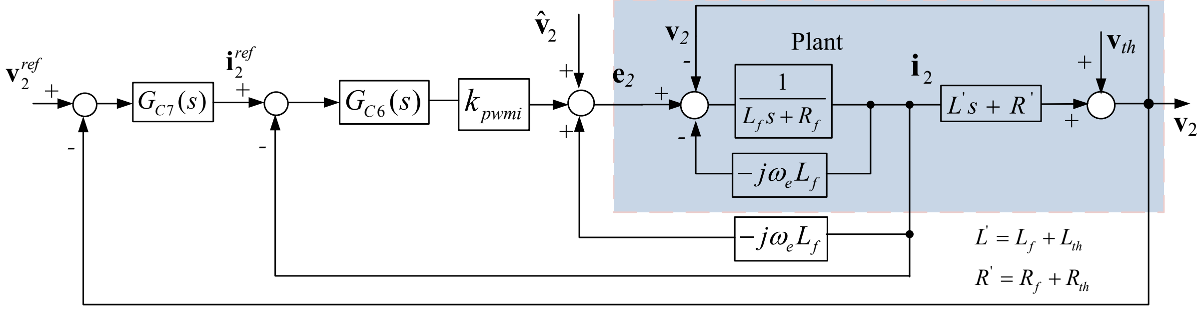

Fig. 4-14 Control block of the line-side voltage source converter, including outer voltage control and inner current control loops. Note that switching function of VSC2 is replaced by the averaged duty cycle variables, and the *d-q* axes control actions are accommodated in a single complex variable domain.

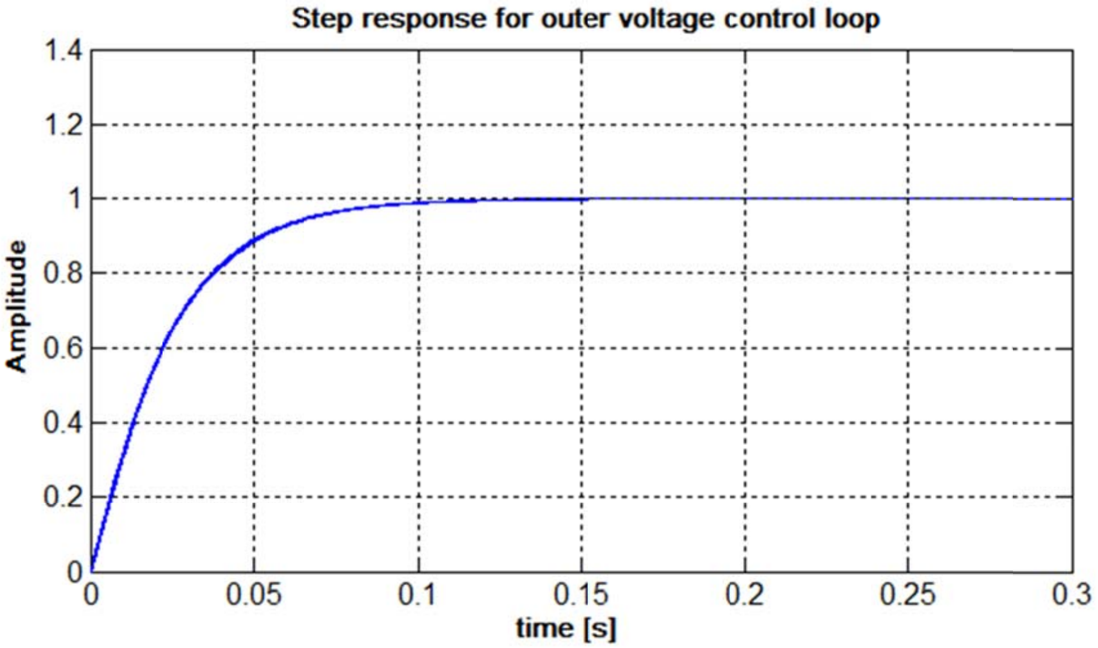

(a)

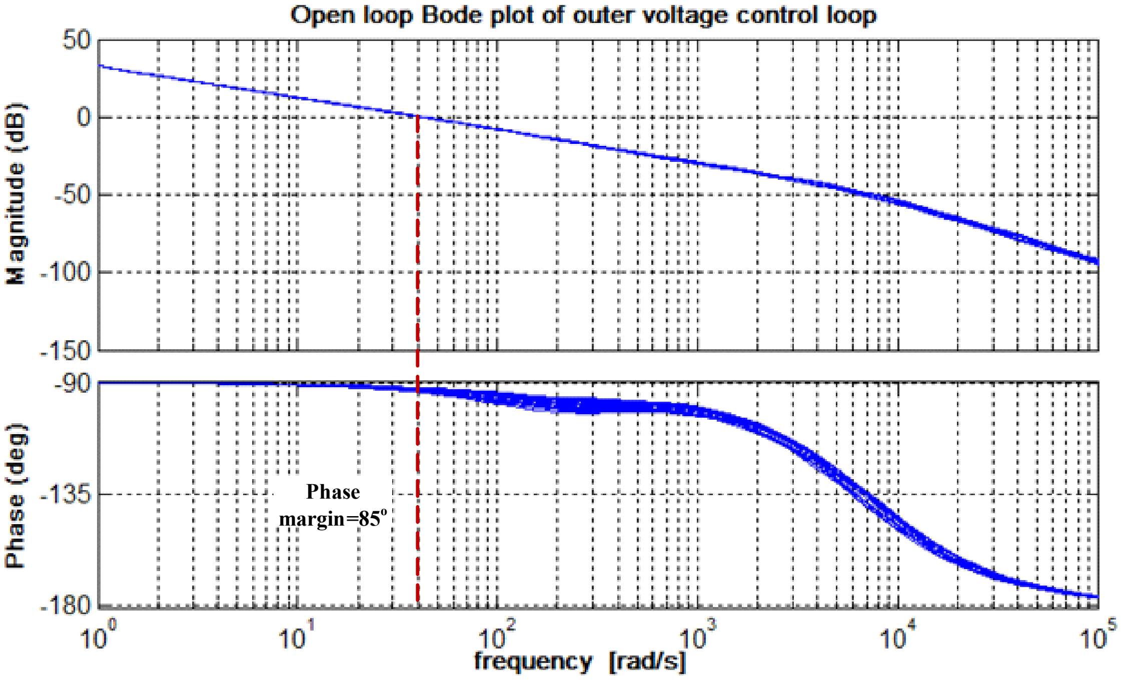

(b)

Fig. 4-15 Responses of the outer voltage control loop. (a) Unit step response, and (b) Bode plot. The responses are obtained by varying the plant parameters (R_f and L_f) by $\pm 20\%$ of nominal values.

4.4.3 Active power management

Power flow management scheme of VSC2 is the secondary level control utilized to determine the preset values of active power (P_2^{ref}) and voltage magnitude (V_2^{ref}) for the inner frequency and voltage regulation blocks, respectively. VSC2 can be operated in three different modes: the islanded, dispatchable grid-connected and non-dispatchable grid-connected modes. In the first and second modes, the DESS is assigned for the dc-link voltage regulation by injecting the compensating current (I_{sto}) from it. In the third case (when the DESS is not working), VSC2 can still supply the power in the non-dispatchable mode. Similar objective of the power management is also discussed in [14]. However, due to the different storage system and control strategies applied in the inner loops of the VSC2 controller, a modified power management scheme is introduced here, making it compatible with the proposed configuration.

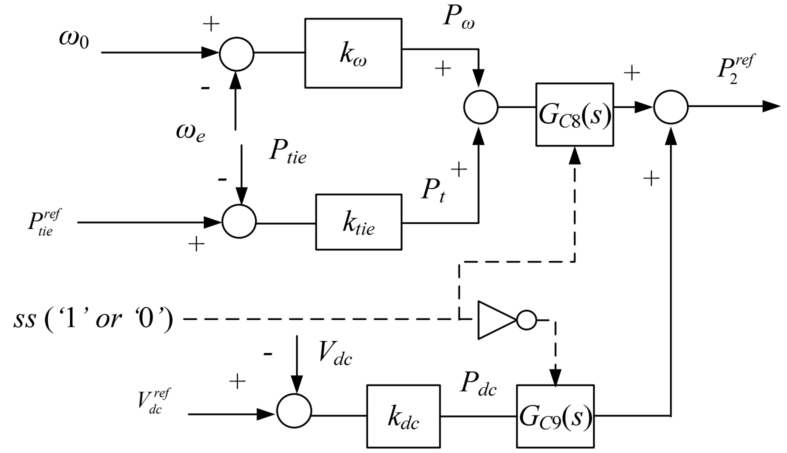

Fig. 4-16 Active power management scheme for VSC2.

The concept of the active power management scheme is illustrated in Fig. 4-16. Each mode of the operations (islanded, dispatchable grid-connected and non-dispatchable grid connected mode) is assigned to a separate loop that produces P_2^{ref} which is the sum of these three components associated with proportional-integral action for (i) frequency regulation, (ii) tie-line regulation and (iii) dc-link voltage regulation, as defined by (4.45)

$$P_2^{ref} = G_{C8}(s)\{\overbrace{k_\omega(\omega_0 - \omega_e)}^{P_\omega} + \overbrace{k_{tie}(P_{tie}^{ref} - P_{tie})}^{P_t}\}ss + G_{C9}(s)\overbrace{k_{dc}(V_{dc}^{ref} - V_{dc})}^{P_{dc}}\overline{ss}. \tag{4.45}$$

Here, P_{tie}^{ref} and P_{tie} are respectively the command and actual value of tie-line power; $G_{C8}(s)$ and $G_{C9}(s)$ are the transfer functions of the respective controllers; ss is the status signal of the DESS, having value '1' and '0' for working and non-working conditions, respectively; and $\overline{ss}$ is the complement of ss $(\overline{ss} = 1 - ss)$. The control parameters k_{ω}, k_{tie} and k_{dc} are the coefficients of frequency, tie-line power and the dc-link voltage regulation, respectively. Likewise, P_{ω}, P_t and P_{dc} are the components of P_{tie}^{ref} related to secondary frequency, tie-line and dc-link voltage regulations, respectively.

When the system is assigned to operate in the dispatchable grid-connected mode, selection of P_{tie}^{ref} is necessary. It is derived from the higher-level supervisory control of the WPSS, considering the power exchange agreement and amount of fuel reserve. With preset value of P_{tie}^{ref} and the system being connected to the grid, the stiff grid impresses the system frequency ($\omega_e = \omega_0$), so the component P_{ω} becomes zero. Assuming the DESS is servicing, ss becomes '1'. This implies that the contribution from dc-link voltage regulation part also zero (P_{dc}=0). Consequently, the PI control action is effective only to the tie-line regulation. The dispatchable mode is attractive from the utility point of view because the system is reflected as a controllable entity that encapsulates all the local fluctuations.

In case of the islanded mode, the DESS should be in operative mode and there is no power exchange with the utility grid, thereby resulting both P_t and P_{dc} equal to zero. The PI control scheme, thus, acts as the secondary frequency regulation, producing P_{tie}^{ref} as the control output. In extreme case when the DESS is not working, the dc voltage (V_{dc}) remains unregulated and the status signal of the DESS becomes '0' $(ss = 0)$. If we desire to keep V_{dc} at the designated value, the disturbance at the dc-link bus should be nullified. That means the available power from VSC1 should be supplied to the utility grid. In this case, the contribution from the secondary frequency regulation and the tie-line regulation is zero. Instead, the PI action is applied for the dc-link bus regulation to generate P_{tie}^{ref} . In short, the active power management scheme, with the aid of the DESS, provides a smooth operation during the islanded and the dispatchable grid-connected modes. For the faulted DESS case, the power management loop functions as the dc-link bus regulation, similar to a normal grid connected non-dispatchable wind turbine generator system.

The selection of the parameters k_ω and k_{tie} in the control loops is achieved by observing the trade-off between the speed and the stability of the active power management. As an illustration, we can represent the control loop in perturbed equation (when *ss*='1') as

$$\left.\begin{aligned} \tilde{P}_2^{ref} &= -(k_{8P} + \frac{k_{8I}}{s})(k_\omega \tilde{\omega}_e + k_{tie}\tilde{P}_{tie}) \\ \tilde{P}_{tie} &= T_g \, \frac{\tilde{\omega}_e}{s} \end{aligned}\right\}, \tag{4.46}$$

where "~" represents the perturbed variables, T_g is the coefficient of grid power transfer, and k_{8P} and k_{8I} are the parameters of $G_{C8}(s)$. Rearranging (4.33) and(4.46), we can derive the expression for characteristic equation as

$$s^2 + (k_\omega k_{8I} m + k_{8P} k_{8I} T_g m)s + mT_g k_{tie} k_{8I} = 0\,. \tag{4.47}$$

Knowing that the participation of k_{tie} and k_ω are respectively on the speed and damping, we select their values for desired dynamic specification.

4.4.4 Reactive power management

The concept of reactive power management is described in Fig. 4-17. The reactive power management scheme generates V_2^{ref} as the sum of droop of reactive power (Q_{tie}) and nominal value of bus #2 voltage (V_0) as

$$V_2^{ref} = V_0 + k_{qt}(Q_{tie}^{ref} - Q_{tie}), \tag{4.48}$$

where k_{qt} is a constant parameter and Q_{tie}^{ref} is the set value of tie-line reactive power. In grid-connected mode, the stiff grid dictates the PCC voltage (V_2). Therefore, the scheme is employed to regulate Q_{tie} (usually at zero), while supplying all the local reactive power demand. If the WPSS is required to supply reactive power to the grid, Q_{tie}^{ref} may be adjusted by a supervisory control technique.

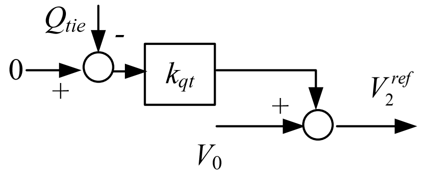

Fig. 4-17 Reactive power management scheme for VSC2.

In case of the islanded operation, Q_{tie} would be zero. So, the control scheme is guided to regulate $V_2\,(=v_{2d})$ at the nominal value (V_0). That would be achieved when all the reactive demand inside the system are met. Thus, the same *V/Q power management* scheme works in all modes without interruption or switching to different control blocks.

The overall block diagram of the control and operational schemes is represented in Fig. 4-18. It illustrates how the individual control schemes fit into the whole system. As desired, the reactive and active power control/management schemes are decoupled to each other. While *V/Q* control and *P/f* control loops are situated in the inner loop, reactive power management and active power management schemes appear at the outermost loops. The proposed scheme may be compared to the conventional governor and excitation control approaches applied in synchronous machine. It also illustrates how the different operating schemes are utilized by the VSC2 system with the aid of the DESS.

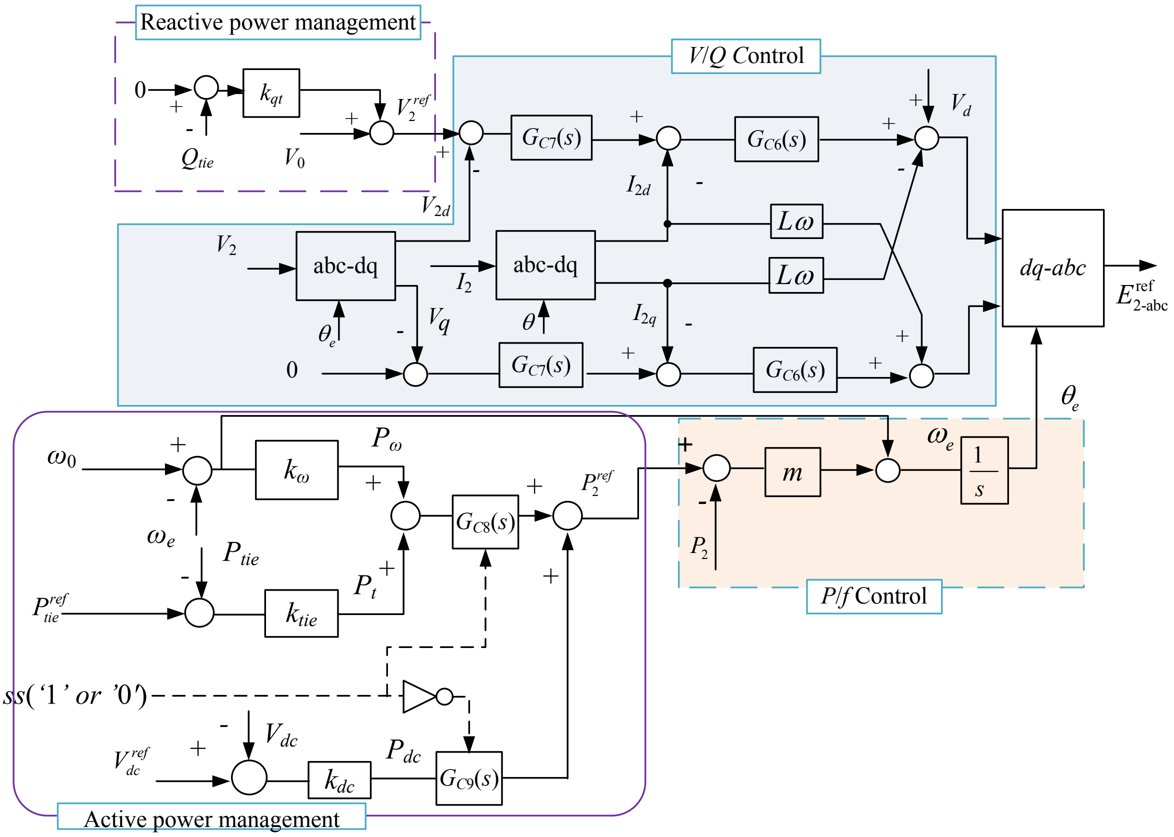

Fig. 4-18 Overall control block diagram of the line-side converter (VSC2) system. The figure shows how the individual control scheme fits into the overall control and management scheme.

4.5 Summary

In this chapter, control and operational schemes of proposed hybrid power system has been developed. The system has three subsystems, namely WTGS, DESS and VSC2. In the WTGS, control law is associated with the variable speed drive control, in which the stator flux orientation control is utilized for the inner current and the MPPT is employed for the rotor speed tracking in the outmost control loop. Further, the pitch angle control is applied to shed the power at the higher wind speed. The control strategy for the DESS is associated with dc-link voltage regulation, in which net compensating power is shared by the UC and the FC/H2/ELZ unit through the coordinated control action. Likewise, the control approaches of the line-side converter system include the active and reactive power regulation under different operating conditions, particularly the stand-alone, dispatchable grid-connected and non-dispatchable grid-connected modes. The control scheme for each subsystem is decoupled in nature because the variables of the one system appear to be disturbance input to the other one. The parameters in the controllers are designed by using linearized models and tuned by applying the IMC method. Simulated results of control schemes have also been demonstrated to validate the operating performances, such as command point tracking, disturbance rejection and wide stability margin, under the variation of plant parameters.

References

[1] D. Rivera, M. Morari and S. Skogestad, "Internal model control: PID controller design," Ind. Eng. Chem. Process Des. Dev., vol. 25 (1), pp 252–265, Jan. 1986.

[2] L. Harnefors and H. Nee, "Model-based current control of AC machines using the internal model control method," *IEEE Transactions on Industry Applications,* vol. 34(1), p. 133-141, 1998.

[3] I. G. Horn, J. R. Arulandu, J. G. Christopher, J. G. Van Antwerp and R. D. Braatz, "Improved filter design in internal model control," *Ind. Eng. Chem. Res,* vol. 35(10), pp. 3437-3441, 1996.

[4] W. Leonhard, *Control of electrical drives*: Springer Verlag, 2001.

[5] J. Hu and Y. He, "Dynamic modelling and robust current control of wind-turbine driven DFIG during external AC voltage dip," *Journal of Zhejiang University-Science A,* vol. 7(10), pp. 1757-1764, 2006.

[6] R. Pena, J.C. Clare and G.M. Asher, "Doubly fed induction generator using back-to-back PWM convertersand its application to variable-speed wind-energy generation," IEE Proceedings Electric Power Applications*,* vol. 143(3), pp. 231-241, 1996.

[7] J.G. Slootweg, H. Polinder, W.L. Kling, "Dynamic modelling of a wind turbine with doubly fed induction generator" IEEE power engineering summer meeting, vol.1, pp. 644– 649, Vancouver Canada, 2001.

[8] N. Horiuchi and T. Kawahito, "Torque and power limitations of variable speed wind turbines using pitch control and generator power control," IEEE power engineering summer meeting, vol.1, pp. 638 – 643, Vancouver Canada, 2001.

[9] A. Mirecki and F. Roboam, "Comparative Study of Maximum Power Strategy in Wind Turbines," IEEE International Symposium on Industrial Electronics, vol. 2, pp. 993-998, 2004.

[10] N. Pogaku, M. Prodanovic and T. Green, "Modeling, analysis and testing of autonomous operation of an inverter-based microgrid," *IEEE Transactions on Power Electronics*, vol. 22(2), pp. 613-625, 2007.

[11] J. A. Peças Lopes, C. L. Moreira and A. G. Madureira, "Defining control strategies for microgrids islanded operation," *IEEE Transactions on Power Systems,* vol. 21(2), 2006.

[12] A. Engler and N. Soultanis, "Droop control in LV grids," Proceeding International Conference on Future Power Systems, pp. 993 - 998, Nov. 2005.

[13] M. Tsai and W. Tsai, "Analysis and design of three-phase AC-to-DC converters with high power factor and near-optimum feedforward," *IEEE Transactions on Industrial Electronics,* vol. 46(3), pp. 535-543, Jun. 1999.

[14] A. Yazdani, "Islanded Operation of A Doubly-Fed Induction Generator (DFIG) Wind-Power System with Integrated Energy Storage," Proceeding IEEE Electrical Power Conference, pp. 153-159, Canada, Oct. 2007.

Chapter 5 Simulation Results and Discussion

The aim of the numerical simulation is to observe the system dynamics over a designated period of time that presents the detail of transient response and predicts the steady state response, with the wide variations of wind speed and load profile. To generate the time series wind data, the technique proposed in section 3.2.1 is employed, which includes four components of wind speed (average, ramp, gust and the turbulence). For the simulation purpose, a few assumptions are made:

- the startup time for fuel cell and electrolyzer are not considered,
- the electrical system is operated in 3-ϕ balanced load with no current flow through the neutral,
- switching is perfect, i.e. there is no loss during switching and the higher order harmonics are neglected.

These assumptions are justifiable for the purpose and the selected simulation time.

In order to investigate the performance, the dynamic model of the components in the proposed wind power and storage system (WPSS) is developed using MATLAB/Simulink [1]. The control schemes have been designed with linearized models, and the overall control and the large-signal component models are integrated and simulated. To test the effectiveness of the proposed operational and control schemes, the WPSS is operated in two modes, islanded and grid-connected. The particular interest is how the embedded energy storage system facilitates the wind turbine generator system (WTGS) working in an islanded mode and a dispatchable grid-connected mode, while fulfilling the operational requirements. To validate the control schemes proposed in the previous chapters, the dynamics of crucial variables from the different subsystems are observed under the impression of disturbances. Based upon the test of the controllers against the parameters uncertainty in chapter four, it is expected that the same is applied for the overall system, so the simulation is performed with nominal values of the parameters. The detailed simulation results are discussed in the following subsections.

5.1 System Startup and Operation in Islanded Mode

Before the startup process, the proposed hybrid power system (depicted in Fig. 2.6) is islanded by opening the switch B, all local loads are turned off, and the fuel cell/electrolyzer (SOFC/ELZ) unit is kept at the standby condition. The initial conditions of the state variables related to the WTGS are assumed as zero to observe the generator's startup process. In cases of the DESS and VDC2, the initial states are set to their respective nominal values. Then, the induction machine is magnetized by the stored charge in the ultracapacitor (UC) and the startup process is carried out with the prevailing wind speed of about 13 m/s. During the startup process, the UC supplies the necessary excitation power for the generator making DFIG run in the motoring mode. After speed builds up, the new power balance mechanism shifts DFIG to the generator mode, and then a sequence of events are introduced into the system as described in Table 5.1.

Table 5.1 Sequence of events in the simulation process

Time	Event
0 s	Simulation starts, generator startup
1 s	ELZ is switched ON
5 s	(25+*j*8) kVA load added
10 s	Grid connection with P_{tie}=10kW
15 s	Wind speed ramp down to 8 m/s
20 s	(10+*j*4) kVA load added
30 s	End of simulation

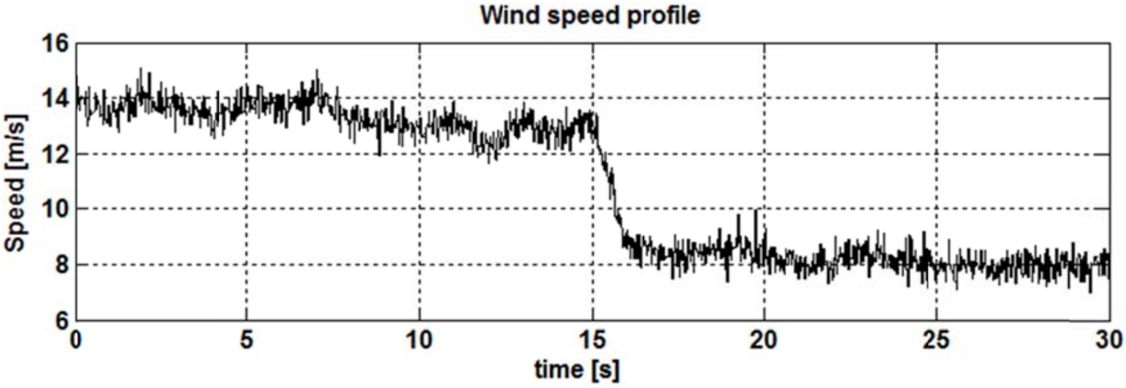

Fig. 5-1 Wind speed profile.

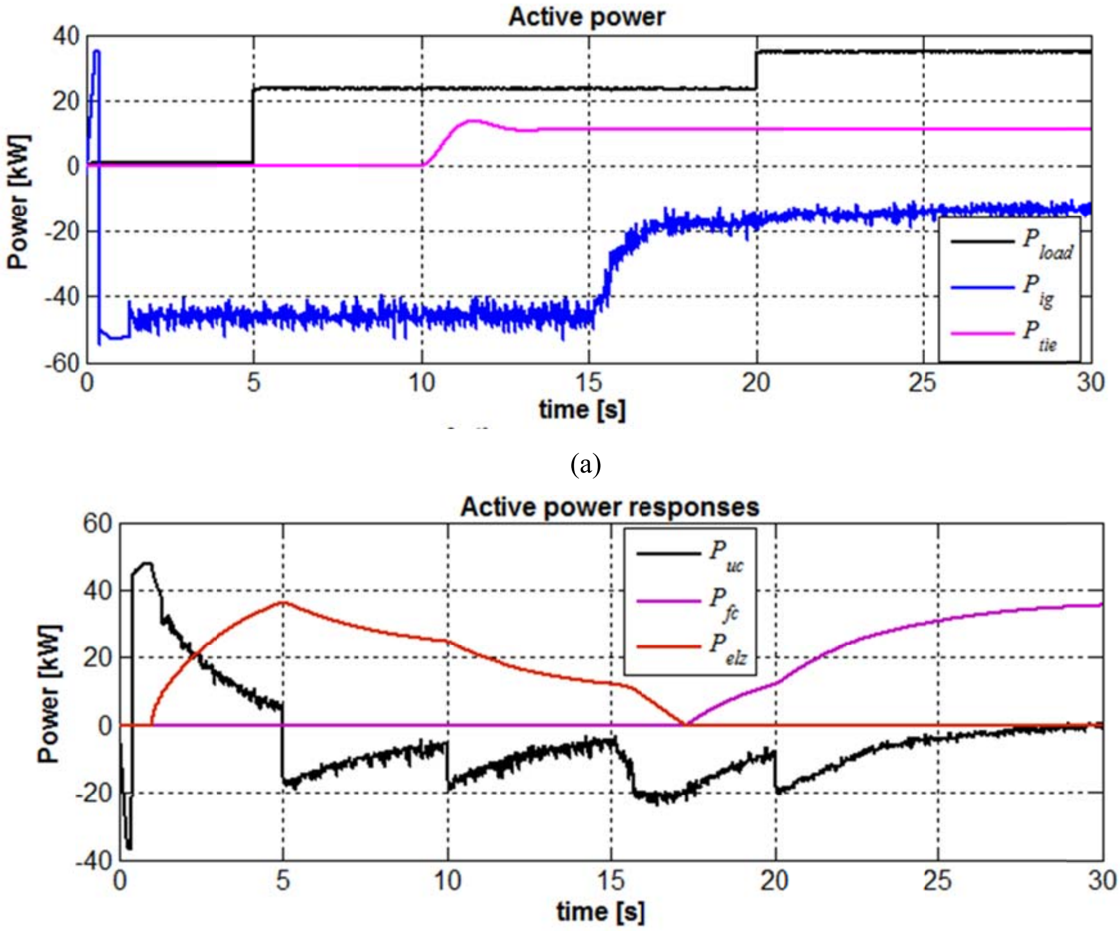

(a)

(b)

Fig. 5-2 Power flow responses of different sources.

The nature of wind speed profile subjected to the wind turbine is depicted in Fig. 5-1. Note that this profile is chosen to observe the types of speed components illustrated in section 3.2.1. Until t=15 s, the average speed of wind is 13 m/s, with the *gust part* and *turbulent* components added to it. At t=15 s, wind ramp is subjected, which causes the reduction in wind speed around 8 m/s. With no local load and the fuel-cell/electrolyzer (SOFC/ELZ) system being disconnected, the net generated power is consumed in charging the dc-link capacitor (C_{dc}) and the ultracapacitor (UC), as illustrated in Fig. 5-2 and Fig. 5-3(a). After t=1 s when the generator stabilizes at the rated speed, the control action of the isolating dc-dc converter (DC2) is activated and the surplus power is fed to the ELZ. Subsequently, H_2 is produced and pumped to the storage tank. At t= 5 s, a local load of (25+j8) kVA is introduced at the bus #2, which causes temporal decrease in the dc-link voltage (V_{dc}). The deviation in V_{dc} is detected by the DC2 controller, the controller generates phase shift angle (δ) as the controlled variable, the UC supplies the transient power, and then the fast restoration of V_{dc} takes place in sequences (see Fig. 5-3(a)). Since the generated power is greater than the load ($P_{ig}>P_{load}$), the excess power still flows through the ELZ towards the new steady state.

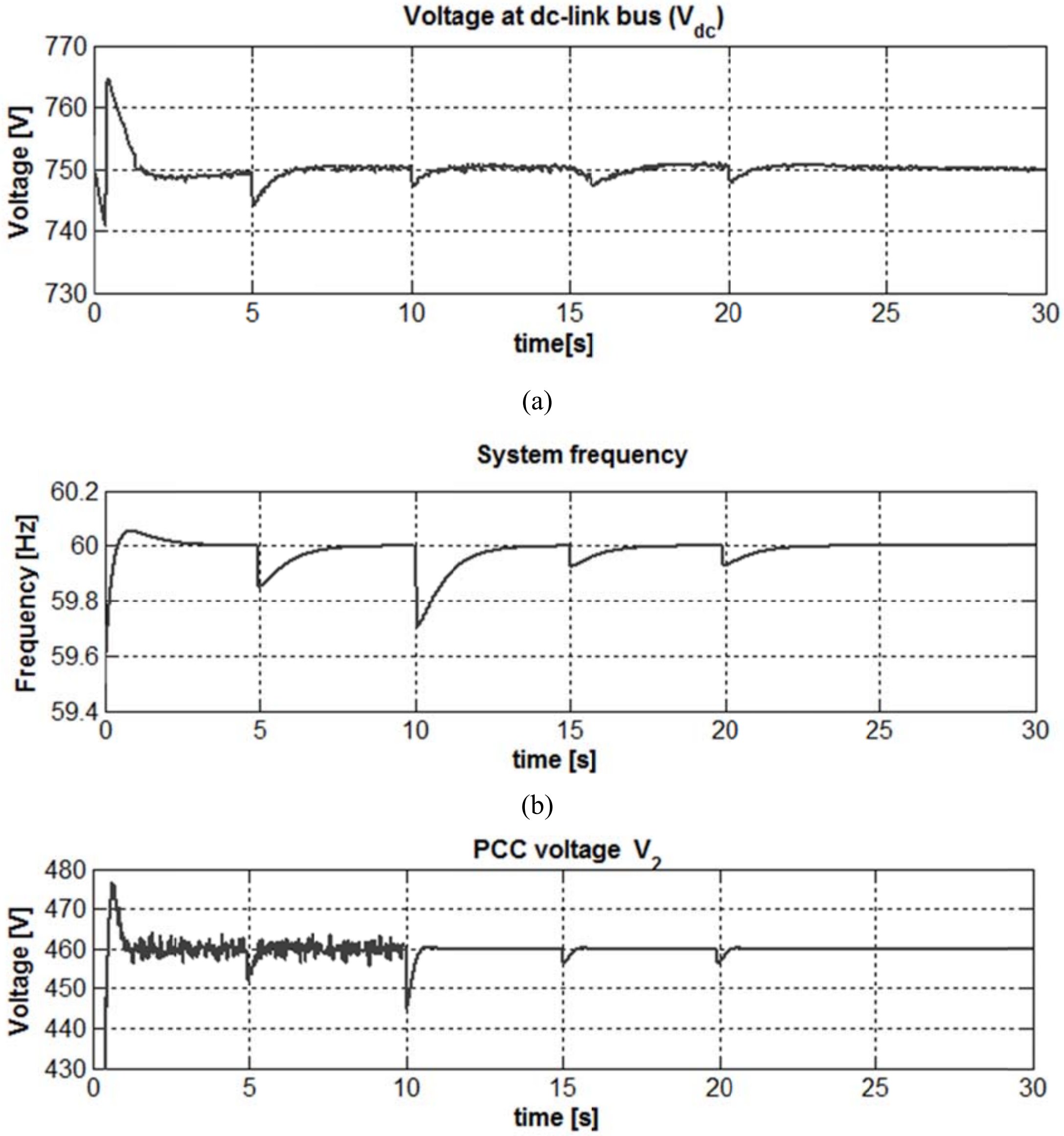

(a)

(b)

(c)

Fig. 5-3 Responses of frequency and voltages.

Fig. 5-3(b) shows how the frequency of V_2 is affected by the disturbances in the islanded mode. Because of the step load at t= 5 s, the control action of the line-side converter (VSC2) is invoked. Consequently, the inner P/f control action is activated as guided by (4.31). This phenomenon is similar to the droop controlled synchronous generator connected to the grid, which avoids the *isochronous mode* of operation. The droop mechanism also plays the important role in sharing loads when multiple inverters are operated in parallel. Because of the droop action, the inverter frequency decreases from the nominal value temporarily with the increase in load. In the islanded mode, there is neither the grid frequency to impress the system nor the tie-line flow (i.e. $P_{tie}^{ref} = P_{tie} = 0$). Therefore, the power management block in Fig. 4-15 functions as the secondary frequency regulation, nullifying the initial deviation of ω_e. Similarly, the step load causes voltage drop in bus #2 voltage (V_2), then the feedback *V/Q control* action is activated to restore V_2 to its reference value of 460 V (see Fig. 5-3 (c)). Thus, in the islanded mode, the VSC2 controller performs the designated job; the regulation of the frequency and magnitude of the terminal voltage by supplying the surplus power to the DESS. The DESS system separates the power into the transient and steady state parts, and passes them through the UC and the SOFC/ELZ respectively.

5.2 Power Dispatching with Grid

At t=10 s, the synchronization process is carried out and the WPSS is connected to the grid via the closing of switch B. Then, a tie-line command (P_{tie}^{ref}) of 10 kW is subjected to the VSC2 controller. Fig. 5-2(a) shows that the tie-line power (P_{tie}) settles at the designated value (10 kW) after a short transient guided by the active power management scheme. The subjection of the tie-line command causes decrease in V_{dc}, which is detected by the DC1 controller in the dedicated energy storage system (DESS). Since the net generated power is still greater than the sum of the load demand and the tie-line power, i.e. $P_{ig}<(P_{tie}+P_{load})$, a part of the power still flows through the ELZ and advances towards the lower steady state value. At t=15 s, the wind speed suddenly decreases to around 8 m/s (Fig. 5-1) and net active power from the generator (P_{ig}) drops to its one-third value (15 kW). This causes a drop in V_{dc}, which is responded by the DESS and supplies the charging current (I_{sto}) to the dc-link bus. Inside the DESS, the UC supplies the transient power, whereas the SOFC provides the steady state deficit because the generated power is now less than the sum of tie-line power and load demand, i.e. $P_{ig}<(P_{load}+P_{tie})$. Due to the slow dynamics of the SOFC, the current gradually rises toward the newer steady state value as guided by (4.28). Similarly, another step load of (10+j4) kVA is invoked at t=20 s. The transient is suppressed by the UC and the SOFC supplies additional steady state current to balance the increased deficit (see Fig. 5-2(b)).

Fig. 5-3(b) and (c) illustrate the responses of line-side converter (VSC2) to the aforementioned disturbances. After the connection of bus #1 with grid at t= 10 s, the grid frequency is impressed on the system. So, the power management scheme now functions as the tie-line regulation. Likewise, the grid voltage dictates bus #2 voltage (V_2), and the control action is directed to regulate Q_{tie}.

Part of the objectives and the results of power sharing scheme explained above may be compared with [3], in which a battery system applied for the power management. It has been reported that the battery system provides the dispatchable power or the load following capability in the islanded mode. However, since the dc-link voltage regulation and charge/discharge control both need to be handled by the line-side converter alone, the operational scope is quite limited. Replacing the battery system by the DESS has wider range of application with more complex configuration and control scheme. Further, the control and operational scheme introduced in this research are more compatible in hybrid configurations. It is because the control scheme aims to impress the frequency as in a conventional synchronous generator, unlike in [3] where the frequency is indirectly regulated by employing the current compensation.

Thus, in the grid connected mode, the VSC2 controller performs the duty of regulating the tie-line power (P_{tie} and Q_{tie}) by injecting the unbalance power from the DESS. Consequently, the fast transient current on the SOFC and ELZ is strategically avoided. The avoidance of transient power is very crucial to both the SOFC and ELZ operations. In case of the SOFC, it causes the fuel starvation, while for the ELZ, the fast transient may lower the operational efficiency and shortens its life [2]. Further, it is also observed that there is smooth transition from the islanded to grid-connected mode by the same control scheme.

5.3 Regulation of the Key Variables

With the nature of given wind profile in Fig 5-1, the resultant rotor speed response is illustrated in Fig. 5-4. During the time $t < 15$ s, wind speed exceeds the rated value, so the rotor speed remains at the rated value generating the rated power with the pitch control action. Fig. 5-5(a) illustrates the action of the pitch controller, in which the pitch angle varies with wind speed to adjust the wind power conversion coefficient (C_P) as shown in Fig. 5-5(b). This causes the DFIG to generate the active power to its rated value, irrespective of the wind speed. Note that higher the wind speed, higher will be the pitch angle and lower will be C_P. After $t > 15$ s, wind speed being less than the rated value, the rotor speed is regulated at its optimum value (illustrated in Fig. 5-4). During this period, the pitch angle is dropped to zero degree and C_P is kept at the maximum value to capture the maximum available power employing the MPPT technique (see Fig. 5-5(b)).

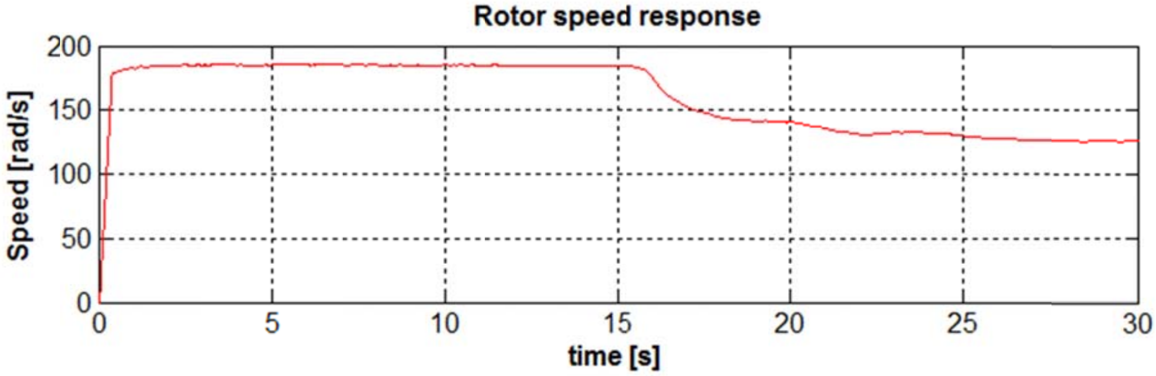

Fig. 5-4 Rotor speed response.

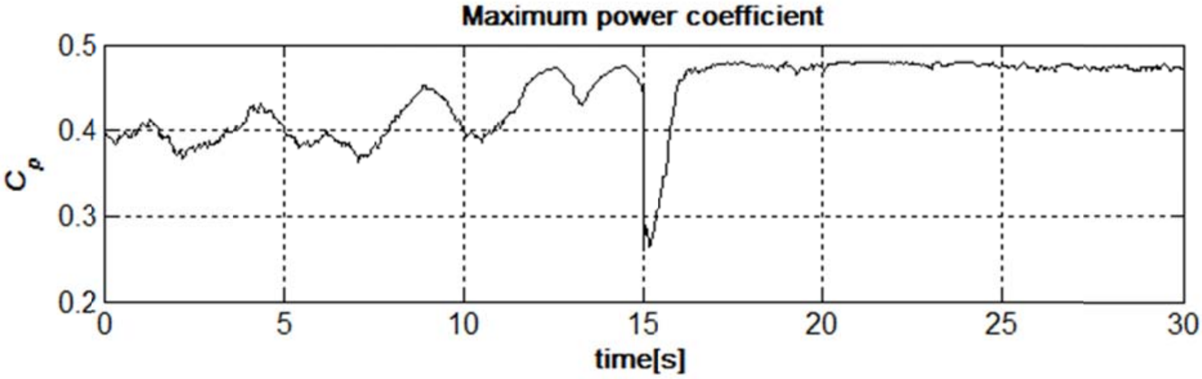

(a)

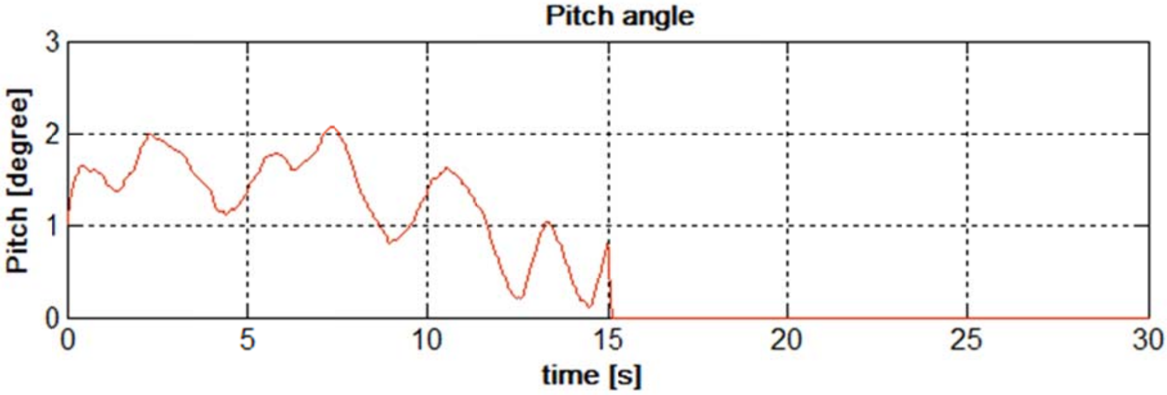

(b)

Fig. 5-5 Responses of power conversion coefficient and pitch angle.

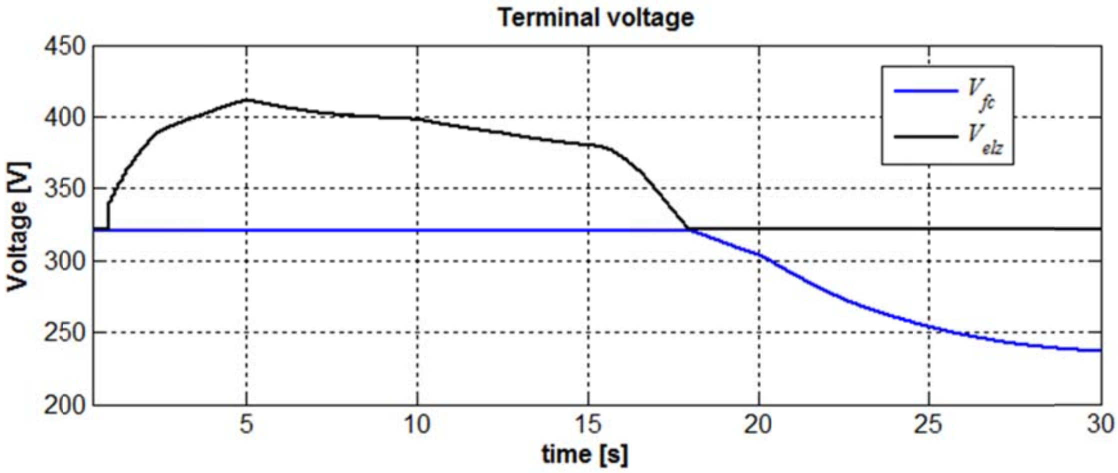

(a)

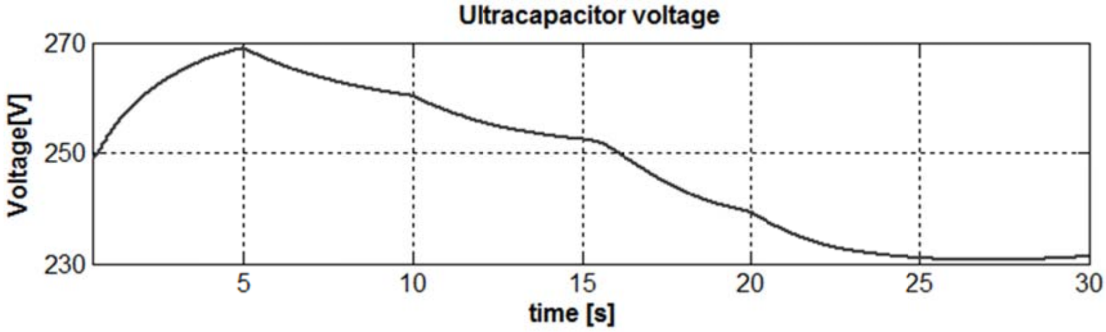

(b)

Fig. 5-6 Response of output voltages. (a) SOFC and ELZ terminal voltages, and (b) UC voltage.

With the variation of the load and generation, current from the SOFC/ELZ also varies, and their terminal voltages (V_{elz}, V_{fc}) change accordingly (see Fig. 5-6(a)). It is notable that by selecting a proper stack size for the SOFC and ELZ, the open circuit voltages are made equal (at 320 V). This leads to treat the SOFC and ELZ as a single unit having a continuous *I-V* curve. Consequently, a common control scheme on DC2 enables smooth transition between the SOFC and ELZ modes. While regulating V_{dc}, there is inevitable deviation in the UC state-of-charge (or its terminal voltage) from its rated value (see Fig. 5-6(b)), which should be restored for the proper operation. The outermost control loop of DC2 is guided to nullify the deviation and maintain the UC voltage around 250 V. Due to the large value of C_{uc}, settling time of the UC voltage control loop is quite large, and hence it is expected to settle at the rated value after some time as discussed in controller design (section 4.3.1).

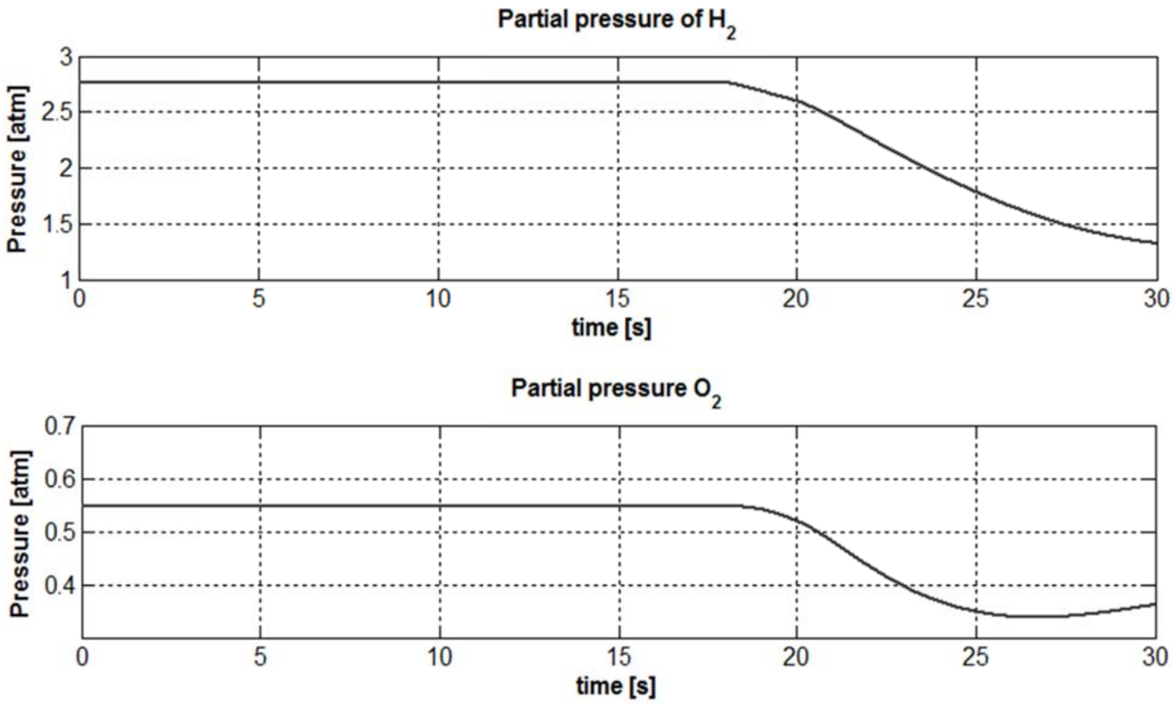

Fig. 5-7 Responses of H_2 and O_2 partial pressures in the SOFC.

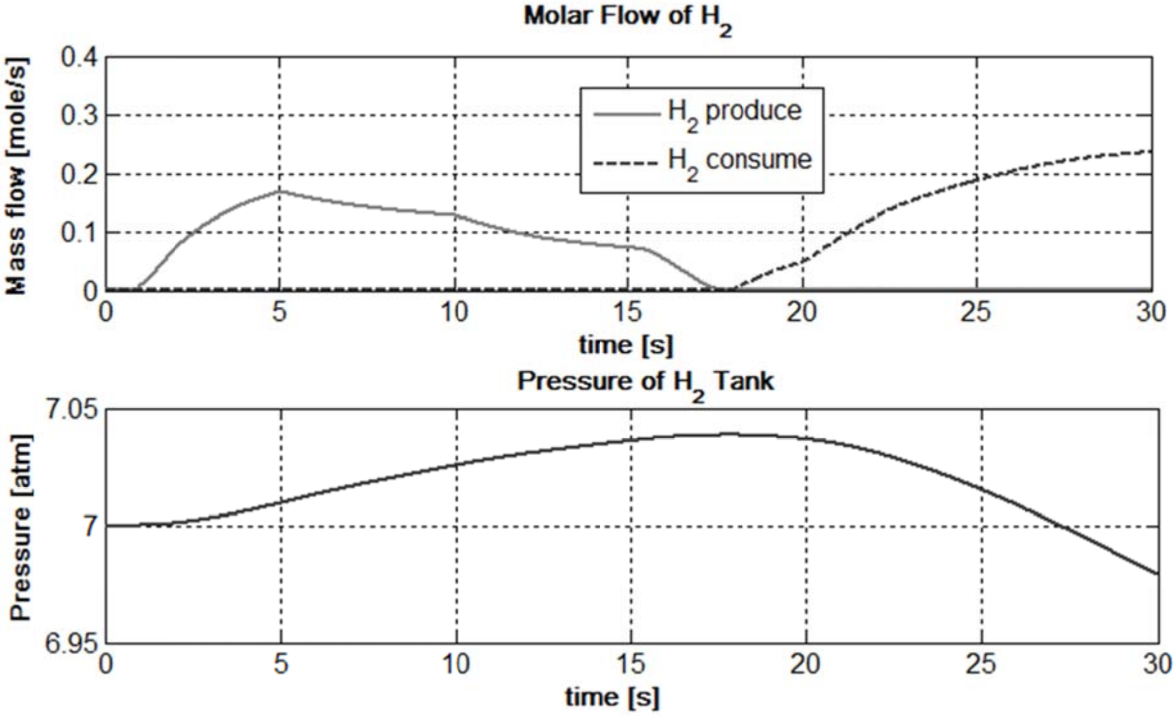

Fig. 5-8 Molar flow and H_2 pressure responses in the storage tank.

Fig. 5-7 depicts the dynamics of reactants' partial pressure. Because of the dynamics in fuel regulator and delay in pressure gain, the time constant for partial pressure dynamics is large. The pressure is not a controlled variable here, so it is required to limit the rise time and the ramp rate of the current to conform the SOFC dynamics.

The dynamics of molar production/consumption rate of H_2 in the ELZ/SOFC and the pressure of storage tank is depicted in Fig. 5-8. Initially the large surplus power is utilized to produce H_2, so the molar production resulting the rise in pressure of H_2. The rate of change of H_2 pressure is, however, smaller than the molar flows (being pressure as integration of the fuel flow). After t=18 s, the current is transferred to the SOFC by consuming the H_2 from the tank, thereby reducing pressure of the tank.

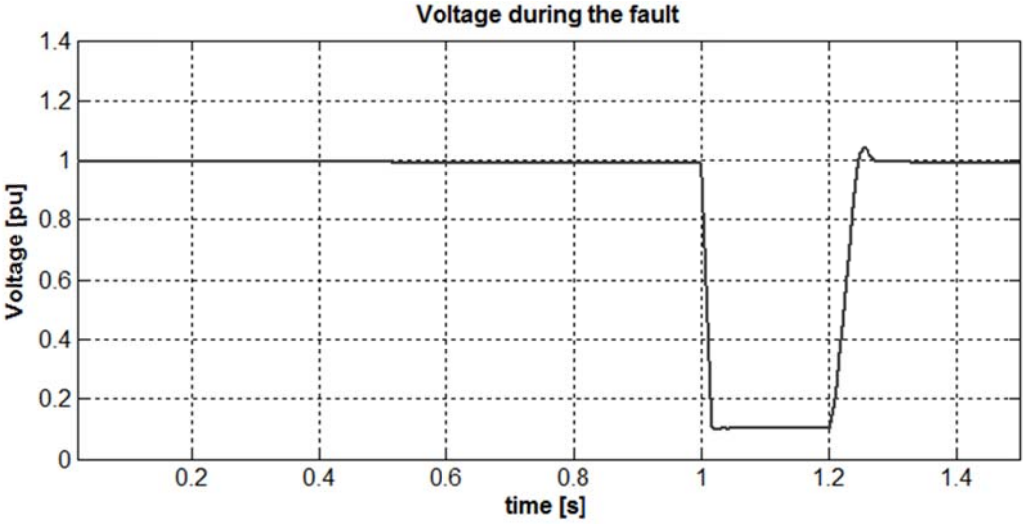

Fig. 5-9 LVRT of the proposed system.

One of the notable merits of the proposed WPSS system lies in its low voltage ride through (LVRT) capability, which is the capability to restore the voltage when the voltage in the grid is temporarily reduced due to a fault or load change in the grid. The voltage of the ac grid may be reduced in one, two or all the three phases. The severity of the voltage dip is defined by the voltage level during the dip (may go down to zero) and the duration of the dip. In the new grid integration codes, it is required to stay connected during the fault (low voltage periods) and support the grid with reactive power to restore the voltage level during the post fault condition [4],[5]. Fig. 5-9 shows the LVRT capability of the proposed hybrid system. At t=1 s a 3φ to ground fault is invoked, which persists until 1.2 s, and then it is cleared. As shown, the voltage restores at its rated value because the storage system effectively injects the desired reactive power during the post fault period (t>1.2 s).

Some of the operation scheme of the DESS explained in this section may be compared with the results reported in [6], [2]. In [6], the FC/ELZ/UC are used as the storage system but has a different system topology, in which the FC and ELZ are both linked to the regulated dc-bus via a separate dc-dc converter for each. Moreover, the power sharing scheme among the FC, ELZ and UC is not compatible with the dynamics of the FC, because the situation of fuel starvation is not considered clearly. For example, the FC (ELZ) has to provide transient part too, even if the UC voltage (V_{uc}) is below (above) the working range. In case of [2], the FC/UC are used as the storage system to manage the fluctuation, and the FC dynamics is considered in power sharing. However, this configuration is not applicable if a power generator source (like photovoltaic or wind power) is connected at the dc-link bus, because it cannot handle the power surplus. Further, the configuration needs the UC of higher voltage rating (thereby necessitating more cells in the stack), and a separated converter may be needed if the ELZ is adopted.

These results show that the subsystems have depicted successful performance of meeting the requirements. As desired, the WPSS provides the solution of short to long-term power management in the islanded and grid-connected modes, and demonstrates an evolution in terms of the power and energy management with reference to the previous works (citations [22]-[28] of chapter one). The WTGS captures optimum power from wind and transfer it to the dc and ac buses, the DESS serves as the dedicated energy balance for wider time-scale, and the line-side converter system regulates the frequency, power and voltage seamlessly in the various operating circumstances, validating the applicability of the scheme. In the proposed scheme, the wind power is taken as the disturbance input, in which the disturbances are subjected to the ac bus and the dc bus. The energy storage system and the line-side converter are jointly employed to reject the disturbances, in the form of load or intermittent power, at the dc and ac buses. Thus, this concept is equally applicable to the other configurations; such as full-scale power electronics converter based WTGS, fixed-speed WTGS and photo voltaic based microgrid. Further, the control and operational approaches can also be utilized in the system having different ratings of generators/loads because the control and operation laws were deducted in per unit base. The major limitation, however, to implement the scheme in a real system is the cost-effectiveness of the proposed storage technologies. With dynamic research and advancement in this field, it is expected that the economy would be favorable in the future.

Reference

[1] Mathworks-MATLAB and Simulink for technical computing (Sep. 2009), available online: http://www.mathworks.com.

[2] P. Thounthong, S. Raël, and B. Davat, "Control strategy of fuel cell and supercapacitors association for a distributed generation system”, *IEEE Transactions on Industrial Electronics,* vol. 54(6), pp. 3225 - 3233, Dec. 2007.

[3] A. Yazdani, "Islanded operation of a doubly-fed induction generator (DFIG) wind-power system with integrated energy storage," IEEE Electrical Power Conference, pp. 153-159, Canada, Oct. 2007.

[4] FERC LVRT standards, Available at: http://www.ferc.gov/industries/electric/indus-act/gi/wind/appendix-G-lgia.doc

[5] C. Jauch, J. Matevosyan, T. Ackermann and S. Bolik , "International comparison of requirements for connection of wind turbines to power systems," Wind energy, vol. 8, pp. 295-306, 2005.

[6] O.C. Onar, M. Uzunoglu and M.S. Alam, "Modeling, control and simulation of an autonomous wind turbine/photovoltaic/fuel cell/ultracapacitor," *Journal of Power Sources,* vol. 185(2), pp. 1273-1283, Dec. 2008.

Chapter 6 Power Sharing Scheme with Multiple VSCs

6.1 Introduction

In the previous chapters, the proposed autonomous system had a single inverter system connected to the grid or point of common coupling (PCC) bus. Therefore, the inverter is solely responsible for the control of power flow and the terminal voltage. However, in a microgrid, there is a possibility of having many inverters connected in parallel and linked with the utility grid. In such cases, it is always desired to share the reactive and/or active power among the inverters, if possible, without using the control information among them. The real and reactive power controls should be independent with each other, and the inverters should share common real and reactive load in proportion to a pre-determined ratio, regardless of plant parameters.

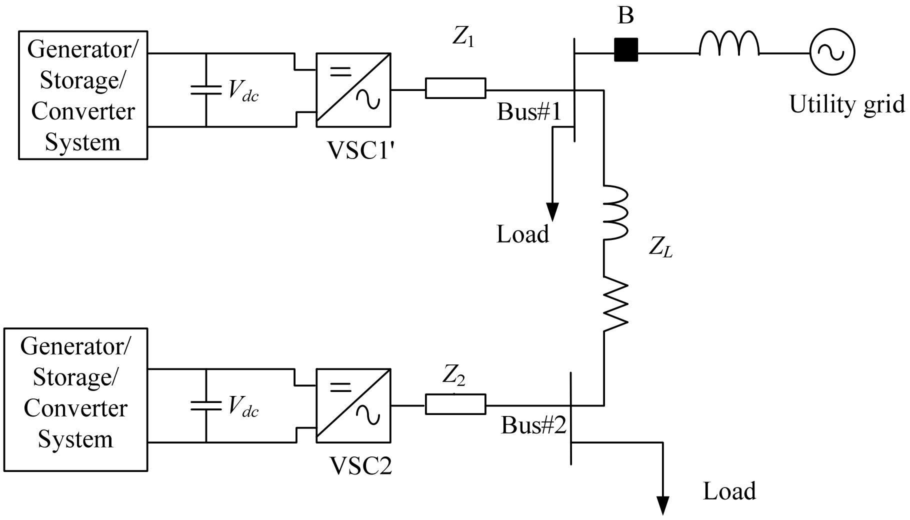

Fig. 6-1 Single line diagram of microgrid with multiple voltage source converters.

Fig. 6-1 shows the configuration of such microgrid, in which an additional controllable power source is connected to bus#1 via VSC1’. Note that the configuation now possesses two controllable power sources, unlike in Fig. 2.6(a) where VSC2 was the only one disspatchable source. In this configuration, the dc voltage regulation is delegated to their respective energy storage system. So, from the inverters' perspective, the dc power/storage system can be replaced by a constant dc source for the time period of interest. These voltage source converters (VSCs) are expected to share the load and tie-line power (P_{tie}), if desired, according to their rating. There are various approaches to design the scheme. The important classes of autonomous load-sharing techniques that have been proposed to date are: (i) the frequency and voltage droop technique [1],[2], termed as conventional droop scheme, (ii) *P-Q* sharing using communication between inverters [3], (iii) the signal injection technique [4], and (iv) the adaptive impedance method [5]. Although the active power sharing is satisfactory with these schemes, neither of them could satisfactorily address the reactive power sharing in a distribution network with a high *R*/*X* value. Utilizing the insights gained from a detailed study of conventional droop techniques, this section first investigates the applicability of conventional droop schemes in *P-Q* sharing with respect to varying *R*/*X*, and proposes a new reactive power sharing scheme by including an idea of virtual impedance. The new scheme ensures that the inverters on a distributed power network share a common load regardless of the line impedance. Here, the VSCs are operating in an islanded mode to share the load at the different buses. If the utility grid is to be connected, the power exchange between the microgrid and the utility grid can be determined by the appropriate management schemes; such as the tie-line regulation, as discussed in the section 4.4 of the previous chapter.

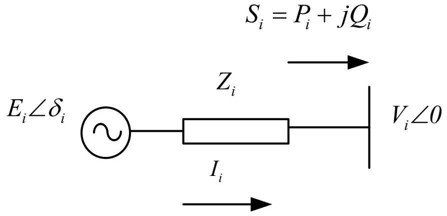

Fig. 6-2 Volltage source connected to the local bus.

6.2 Applicability of Droop Regulation

The idea behind the conventional droop control is that the generators themselves can set their instantaneous *P-Q* flow based upon the decoupled relationship between the active power and the reacitive power, respectively with the frequency and voltage magnitude, so that the power demand within a system can be shared among the generators in pre-specified manner. However in low-voltage (LV) and medium-voltage (MV) microgrids, the line connection being highly resistive, the decoupling is not possible, and hence the wireless droop scheme is quite difficult. To get the clear picture of coupling nature of network variables, consider a system as in Fig. 6-1, in which the active and reactive power supplied by the i^{th} voltage source to the PCC bus can be represented by

$$\left.\begin{aligned} P_i &= \left(\frac{E_iV_i}{Z_i}\cos\delta_i - \frac{V_i^2}{Z_i}\right)\cos\theta_i + \frac{E_iV_i}{Z_i}\sin\theta_i\sin\delta_i \\ Q_i &= \left(\frac{E_iV_i}{Z_i}\cos\delta_i - \frac{V_i^2}{Z_i}\right)\sin\theta_i - \frac{E_iV_i}{Z_i}\cos\theta_i\sin\delta_i \end{aligned}\right\}, \tag{6.1}$$

in which the variables and the parameters are defined in Fig. 4-2. Defining the control variable as $v_i=\Delta E_i= E_i\cos\delta_i - V_i$ and $\delta_i\cong\sin\delta_i$ we have,

$$\begin{bmatrix} P_i \\ Q_i \end{bmatrix} = \frac{V_i}{Z_i}\begin{bmatrix} E_i\sin\theta_i & \cos\theta_i \\ -E_i\cos\theta_i & \sin\theta_i \end{bmatrix}\begin{bmatrix} \delta_i \\ v_i \end{bmatrix}. \tag{6.2}$$

Clearly, (6.2) depicts the fact that P_i-Q_i is decoupled with δ_i-v_i only in ideal case; namely pure resistive (θ_i=0) or pure inductive (θ_i =π/2) case. For the high X/R value, traditional droop sharing scheme can be implemented, where the active power and the reactive power are decoupled with the frequency and voltage magnitude, respectively. Conversely for a highly resistive line coupling, the droop sharing is needed to be reversed. In practice, LV lines have R/X ratio lying between 2 to 6. In such cases, neither of the above techniques fits well.

In order to find a proper control scheme, the applicability of conventional droop scheme against different values of R/X is checked first; and based upon the limitations, the proper scheme will be investigated. The frequency and the voltage droop derived from the conventional scheme for i^{th} VSC is written as [1]

$$\left.\begin{aligned} &\omega_i = \omega_0 + m_i(P_i^{ref} - P_i) \\ &V_i = V_0 - n_iQ_i \\ &\text{with, } m_i = \frac{\omega_0 - \omega_{min}}{P_i^{rated}} \\ &\qquad n_i = \frac{V_0 - V_{\min}}{Q_{max,i}} \end{aligned}\right\}. \tag{6.3}$$

Here, V_0 and ω_0 are the nominal values of voltage and frequency, respectively. Similarly, P_i^{ref}, $Q_{max,i}$, ω_{min} and V_{min} represent the rated active power, maximum reactive power, frequency at full load power and minimum load voltage of the system, respectively, of the i^{th} inverter. The coefficient m_i and n_i are the droop coeffiecients as defined by the equation. For a microgrid, m_i

and n_i are normally chosen as ± 2% and ± 5%, respectively, in per unit system [6].

The control law for the control variables (δ_i, v_i) can be written as,

$$\left.\begin{aligned} \frac{d\delta_i}{dt} &= \omega_0 + m_i(P_i^{ref} - P_i) \\ \frac{dv_i}{dt} &= (V_0 - V_i) - n_i Q_i \end{aligned}\right\}. \tag{6.4}$$

Here, V_i represents the voltage at the point of i^{th} common coupling. It has been reported that by controlling v_i, rather than E_i or V_i, the impedance mismatch of coupling reactance (Z_i) is minimized [7]. The block diagram of the droop regulation is also shown in Fig. 6-3.

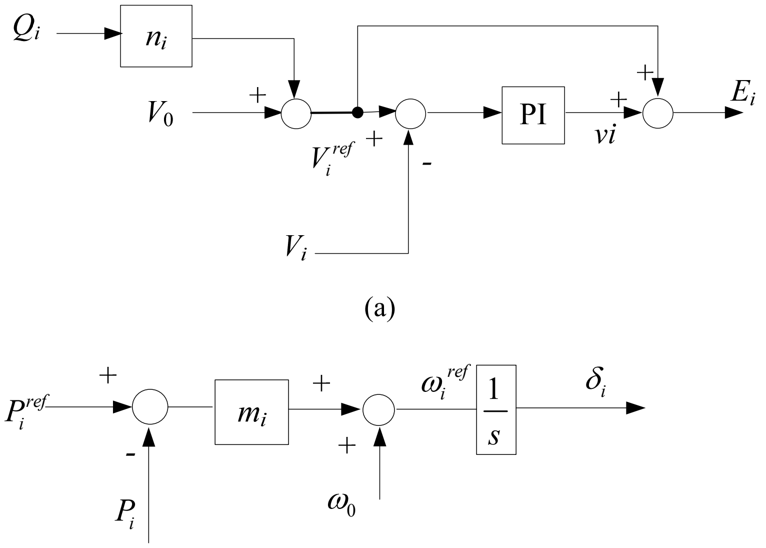

(a)

(b)

Fig. 6-3 Conventional droop schemes. (a) *V/Q* droop, (b) *P/f* droop

From (6.2) to (6.4) and performing the small signal analysis around the operating point, we have

$$\frac{d}{dt}\begin{bmatrix} \tilde{\delta}_i \\ \tilde{v}_i \end{bmatrix} = \frac{V_i}{Z_i}\begin{bmatrix} -m_i E_i \sin\theta_i & -m_i \cos\theta_i \\ n_i E_i \cos\theta_i & -n_i \sin\theta_i \end{bmatrix}\begin{bmatrix} \tilde{\delta}_i \\ \tilde{v}_i \end{bmatrix}. \tag{6.5}$$

Here, the variables with '~' represent the perturbed values, whereas the quantity with capital letter are the values at the operating point. The characteristic equation of the system represented by (6.5) can be written as

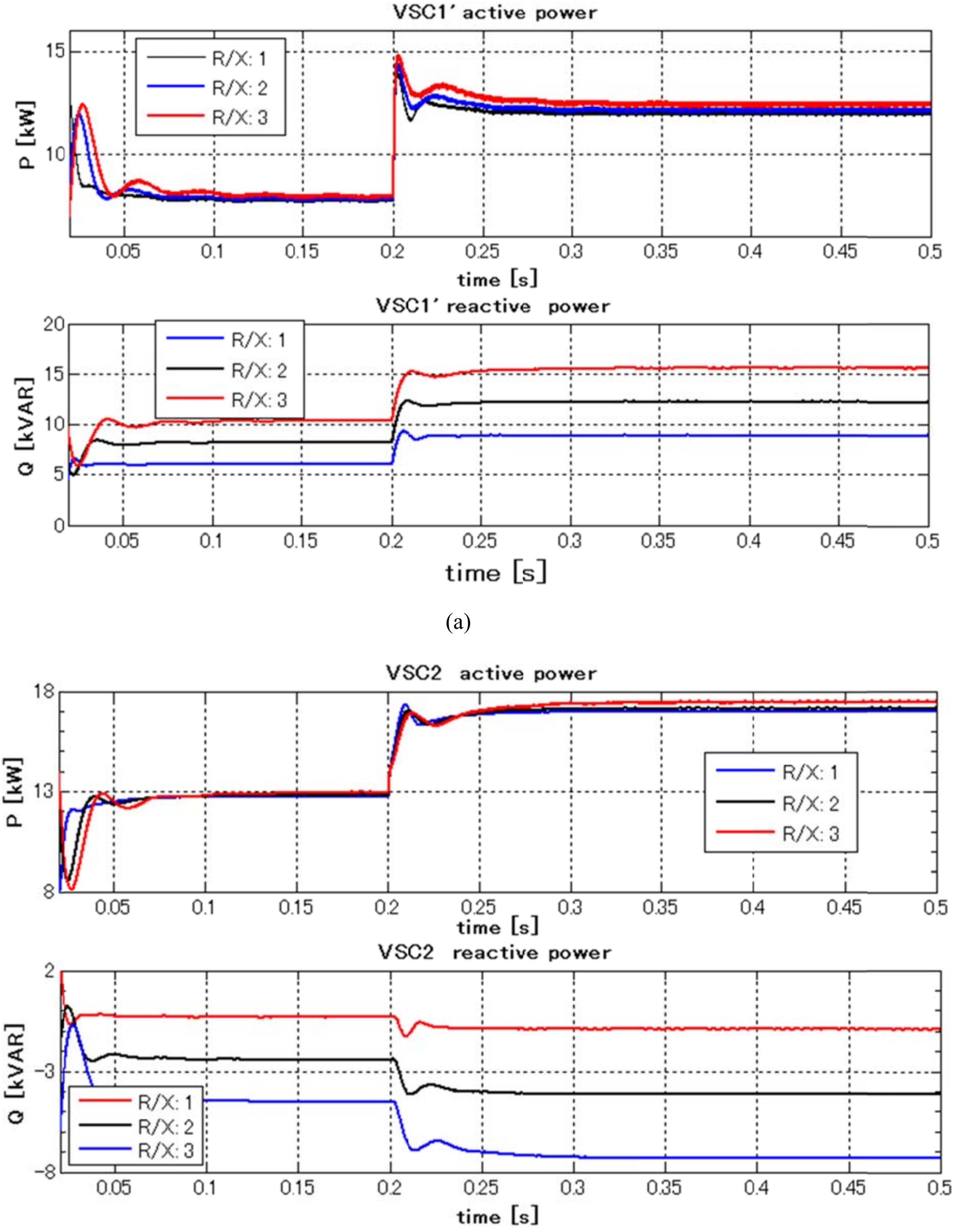

(a)

(b)

Fig. 6-4 Power flow dyanamics of VSCs. (a) VSC1' (b) VSC2.

$$\left.\begin{aligned}&s^2+B_1s+C_1=0,\\&B_1=\frac{V_i\sin\theta_i}{Z_i}(E_im_i+n_i)\ and\ C_1=\frac{E_iV_i^2}{Z_i^2}m_in_i\end{aligned}\right\}. \qquad (6.6)$$

Since $B_1, C_1 > 0$, the poles always situate at the stable plane indicating that the small signal model of the system is stable for any value of *R/X*. The choice of m_i and n_i is a trade-off between the stability and the voltage regulation.

Discussion : The above scheme is tested to the system shown in Fig. 6-1, under the MATLAB/Simulink platform [8]. The ratings of VSC1' and VSC2 are kept 20 kVA and 30 kVA respectively. The graphs in Fig. 6-4 shows the dynamics of the power flow through the VSCs, with different *R/X* values of line impedance. Initially a load of (15+*j*8) kVA was connected to the bus#1 and (5+*j*3) kVA at bus #2. At t=0.2 s another step load of (8+*j*3)kVA is introduced at the bus #1. It can be seen that *P* is apparently regulated against different *R/X* values, whereas the *Q* is heavily affected by the value. With the increasing value of *R/X*, the circulating *Q* increases, though the voltage regulation is satisfactory (Fig. 6-5). This phenomenon of circulating current due to the mismatch of connecting impedance and high resistive nature of connecting impedance are reported in [10] and [6]. The circulating reactive current is not allowed in the system as it creates an extra burden to the system. Hence, the conventional droop scheme is not applicable in the system with resistance dominated line.

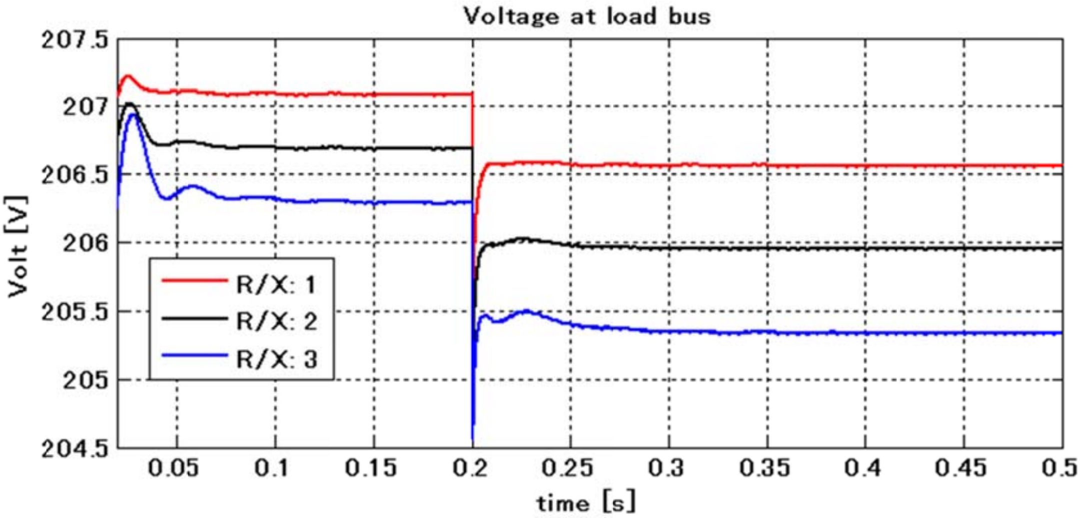

Fig. 6-5 Voltage response of the load bus.

6.3 Introduction of Virtual Impedance

While observing the power flow dynamics in Fig. 6-4, it can be noticed that the origin of the circulating reactive power is due to the mismatch of impedance between the respective inverter and the load bus. Larger the impedance, the smaller is the reactive power flow and vice-versa. Thus, the the inverters with smaller interconnecting impedance supplies the circulating reactive power to the inverter with larger interconnecting impedance.

To solve this, a large interface inductors can be included between the inverter and the PCC bus, but they are heavy and bulky. Resistive compensation can be made by adding its effect in setting the reference voltage in [6]. However, the amount of resistive part to be compensated is related to the location of load change, which being the random event, can not be predicted in multi load bus system. In [5], authors have proposed the concept of adaptive impedance which varies with the reactive power flow. However, the model is not appealing for the predominately resistive line as it compensates mainly the reactance part. Moreover, the effective impedance sought by the VSCs is susceptible with the current transient. This study tries to address these limitations by introducing the virtual impedance which varies with reactive power as

$$z_{Ei} = (z_{\mathbf{0}} + k_{1i}Q_i)\,, \tag{6.7}$$

where z_0 is the reference impedance and the k_{1i} is the constant which determines the sensitivity of Q_i over z_{Ei}. Both parameters are carefully selected depending upon the network and operational circumstances. This impedance compensates the reactive power difference due to line impedance unbalance by providing the proper reference voltage given by

$$V_i = V_o + n_i^{'}P_i - (z_{0i} + k_{1i}Q_i)I_i\,. \tag{6.8}$$

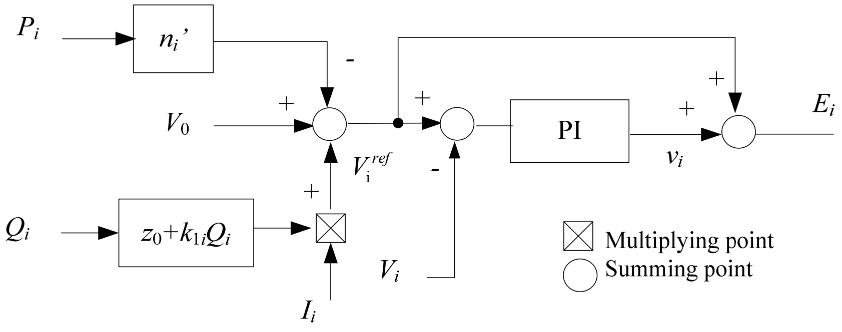

Fig. 6-6 Block diagram of proposed voltage and reactive power regulation scheme.

Here, n_i' is the constant coefficient to decouple the effect of active power on V_i.. It is worthwhile to note that the voltage regulation in (6.8) has sought two important considerations: (i) regulation of virtual impedance, (ii) decoupling of the effect of P_i over V_i. Thus, the set of differential equations to represent the P_i-Q_i regulation evolves from (6.4) to (6.9), given by

$$\left.\begin{aligned} \frac{d\delta_i}{dt} &= \omega_{\mathbf{0}} + m_i(P_i^{ref} - P_i) \\ \frac{dv_i}{dt} &= (V_{\mathbf{0}} - V_i) + n'P_i - (z_{\mathbf{0}} + k_{1i}Q_i)I_i \end{aligned}\right\} . \tag{6.9}$$

Note that, though the active power is also affected by the output impedance, it is effectively controlled by self-adjusting of the phase angle alone. The block diagram of the proposed scheme is also shown in Fig. 6-6.

6.4 Small Signal Modeling and Control Design Rules

In order to investigate the stability and the transient response of the system, a small-signal analysis is performed. The closed-loop system dynamics has been derived, taking into acccount of well known stiff load bus approximation [9]. The small-signal dynamics of the phase angle difference and the voltage difference (δ_i, v_i) are obtained by linearizing (6.2) and (6.9) at θ=45°. This is fairly reasonable for the small-signal anlysis and controller gain estimation of the considered microgrid with the power network of R/X>1. Although the complete modeling requires the several low-pass filters with signals P_i, Q_i, and I_i, the low-pass filters are excluded from the small signal analysis, without loosing the accucary of the result. It is because the filter will not cause any considerable effect on the closed loop dynamics if the corner frequency of low-pass filter is selected quite higher than the dominant poles. The modified dynamic equations in pertubed form becomes

$$\left.\begin{aligned} \frac{d\tilde{\delta}_i}{dt} &= -m_i\tilde{p}_i \\ \frac{d\tilde{v}_i}{dt} &= n_i'\tilde{p}_i - (z_0\tilde{i}_i + k_1\tilde{q}_i I_i + k_{1i}Q_i\tilde{i}_i) \end{aligned}\right\} . \tag{6.10}$$

Noting that

$$\left. I_i = \frac{S_i}{V_i} = \sqrt{(P_i^2 + Q_i^2)}\,/\,V_i, \;\; i.e. \;\; \tilde{i}_i = \frac{2}{S_i V_i}\left(P_i\tilde{p}_i + Q_i\tilde{q}_i\right)\right\},$$

and substituting the values from (6.2) to (6.10) we get,

$$\left.\begin{aligned} \frac{d\tilde{\delta}_i}{dt} &= -m_i \tilde{p}_i \\ \frac{d\tilde{v}_i}{dt} &= \zeta\, \tilde{p}_i - \kappa \tilde{q}_i \end{aligned}\right\}.$$

Simplifying, we get

$$\frac{d}{dt}\begin{bmatrix} \tilde{\delta}_i \\ \tilde{v}_i \end{bmatrix} = -\frac{V_i}{Z_i\sqrt{2}}\begin{pmatrix} m_i E_i & m_i \\ (\zeta+\kappa)E_i & \zeta-\kappa \end{pmatrix}\begin{bmatrix} \tilde{\delta}_i \\ \tilde{v}_i \end{bmatrix},. \tag{6.11}$$

where

$$\zeta = \left\{ n_i' - \frac{2P_i}{S_i V_i}(z_0 + k_{1_i} Q_i) \right\}$$

$$\kappa = \frac{1}{V_i}\left\{ (z_0 + k_{1i} Q_i)\frac{2Q_i}{S_i} + k_{1_i} S_i \right\}.$$

Thus, the characteristic equation of the system becomes,

$$s^2 + B_2 s + C_2 = 0\,, \tag{6.12}$$

with

$$\left.\begin{aligned} B_2 &= \frac{V_i}{Z_i\sqrt{2}}\left\{ m_i E_i - n_i' + \frac{k_1 S_i}{V_i} + 2\left(\frac{P_i + Q_i}{S_i}\right)\left(z_0 + k_{1i} Q_i\right) \right\} \\ C_2 &= \frac{V_i\, m_i E_i}{Z_1^2}\left\{ (z_0 + k_{1i} Q_i)\frac{2Q_i}{S_i} + k_{1i} S_i \right\} \end{aligned}\right\}.$$

The small signal stability of the system is ensured if B_2, $C_2 > 0$. For a VSC, the value of n' is comparable to $m\cos\theta$, implying that $m_i E_i > n_i'$. For the lagging reactive power, Q_i is positive implying that the stability can be achieved for any value of the parameter. But, when the inverter is supplying the leading reactive power, Q_i becomes negative. In that case, the stability is granted if

$$\left.\begin{aligned} & z_0 + k_{1i} Q_{maxi} \geq 0 \\ & or, z_0 \geq k_{1i}\left| Q_{max,i} \right| \end{aligned}\right\}. \tag{6.13}$$

In this case, $Q_{max,i}$ is the maximum leading reactive power supplied by the inverter. That would make $C_2 > 0$ because $2Q_i < k_{1i} S_i^2$ for any operating conditions. Thus, it can be concluded that the small signal stability is confirmed when (6.13) is satisfied.

6.5 Simulation Results

The proposed scheme is tested on the MATLAB/Simulink model of the microgrid shown in Fig. 6-1. The loads are assumed to be three phase balanced. The main aim of the scheme is to regulate the reactive power, against the different values of *R/X*, as the conventional scheme is only able to regulate the active power. It should be noted that the rating of inverters are chosen to be same (20 kVA each), which is not necessary in general (the rating of inverters only need to alter the values of m_i, n_i). Fig. 6-7 shows the power flow dynamics through the VSCs when the line impedance is changed. Initially the load of (20+*j*8) kVA at the bus #1 and (5+*j*3) kVA bus #2 are shared by the VSCs. At t=0.2 s, another load of (5+*j*3) kVA is connected to bus #1, which is followed by the injection of another load of (5+*j*3) kVA at bus #2 at t=0.35 s. It can be seen that the active power and reactive power are shared between the inverter, proportional to their ratings, in all conditions, irrespective of the different *R*/*X* value of the line impedance.

Similarly, the voltage dynamics curve shown in Fig. 6-8. indicates that load voltage regulation is not affected by the *R*/*X* value due to the elimination of the circulating reactive power. The deviation in the load voltage is regulated to the desired value by the secondary voltgae control. Another notable merit of the scheme is that the reactive load sharing by the VSCs can be made flexible. For example, it is not likely that the VSCs which are separated far apart share the common reactive load equally, irrespective of the load location. It is expected that the VSC near the load should share more reactive load than that of VSC situated in farther distance, so that the line loss can be reduced (this concept is, however, not effective for the active power sharing as there are many constraint in doing so). The proposed scheme can provide this option by the choice of the of z_0 and k_{1i}. Fig. 6-9 shows how the individual VSC responds with the load change in the nearest load bus. For the ease in analysis purpose, the equal ratings of VSCs are selected again. Initially, when both buses were equally loaded, the power sharing between the VSCs was equal. When a load of (5+*j*3) kVA is applied to bus #1, VSC1' shares more reactive power than VSC2. Again when another load of (5+*j*3) kVA is connected to bus #2, VSC2 shares more reactive power than VSC1'. Thus, the converter situated nearer to the load can be commanded to share more reactive load until they are overloaded. Active power sharing remain, however, unaffected by the choice of k_1 and z_0, as required.

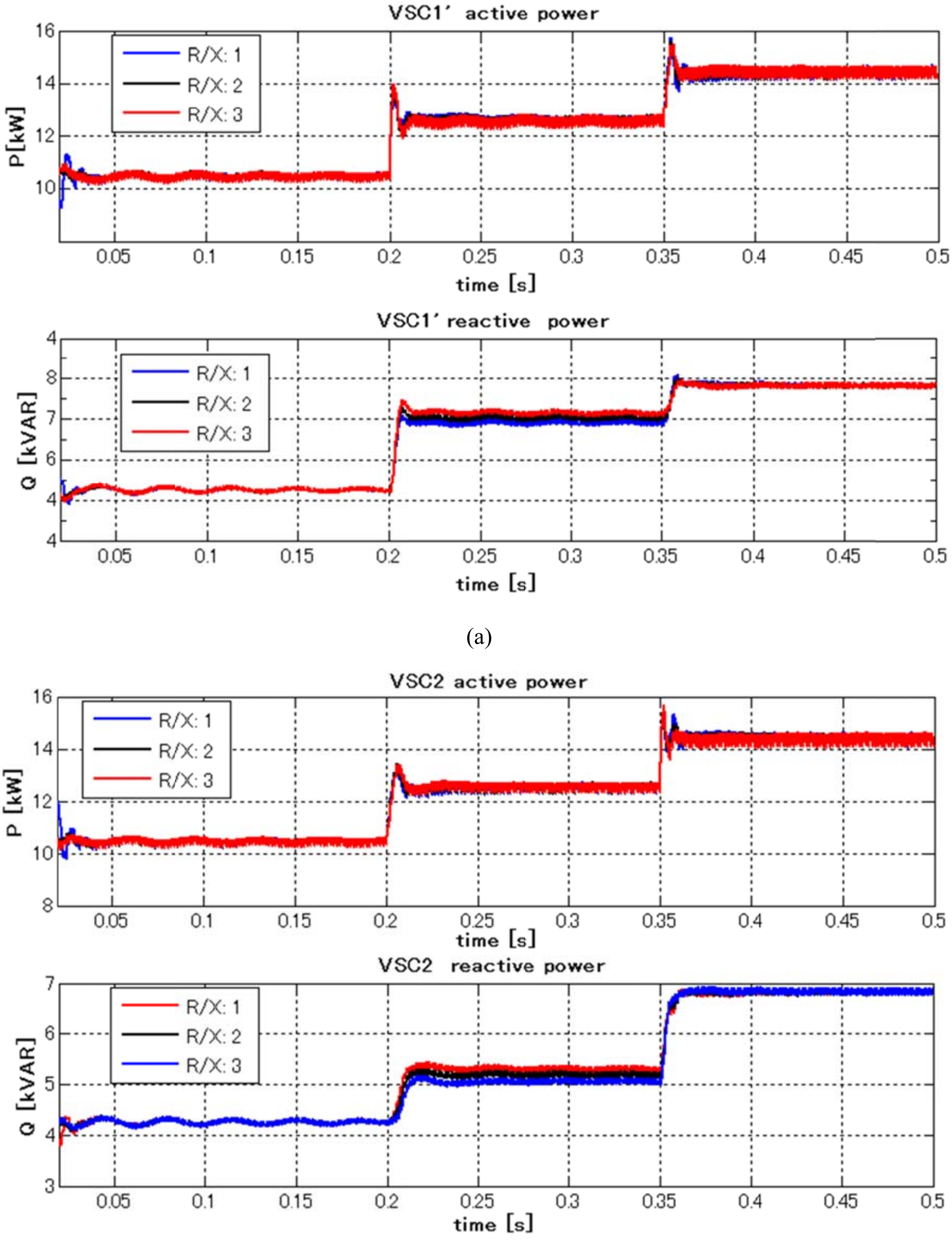

(a)

(b)

Fig. 6-7 Power flow dynamics of proposed scheme. (a) VSC1', and (b)VSC2.

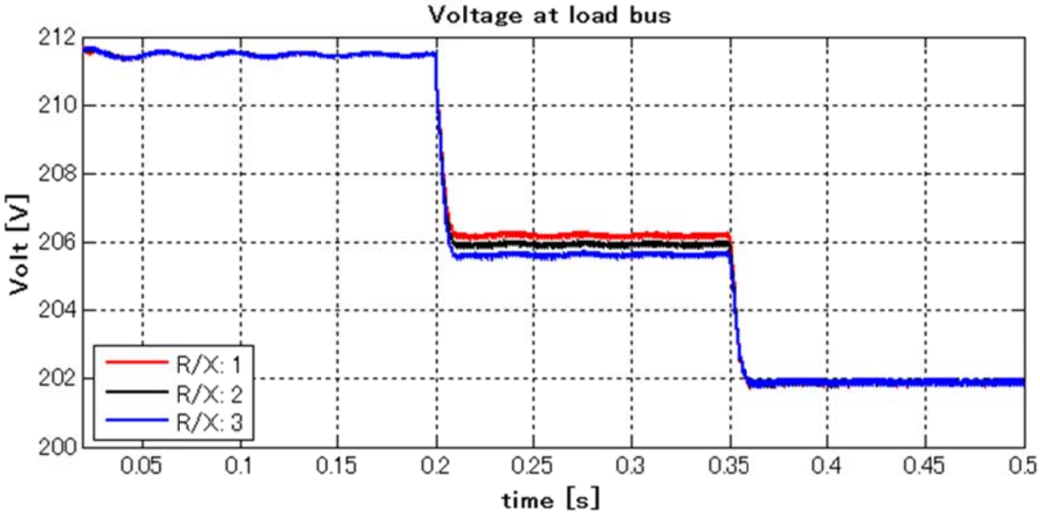

Fig. 6-8 Voltage dynamics of proposed scheme.

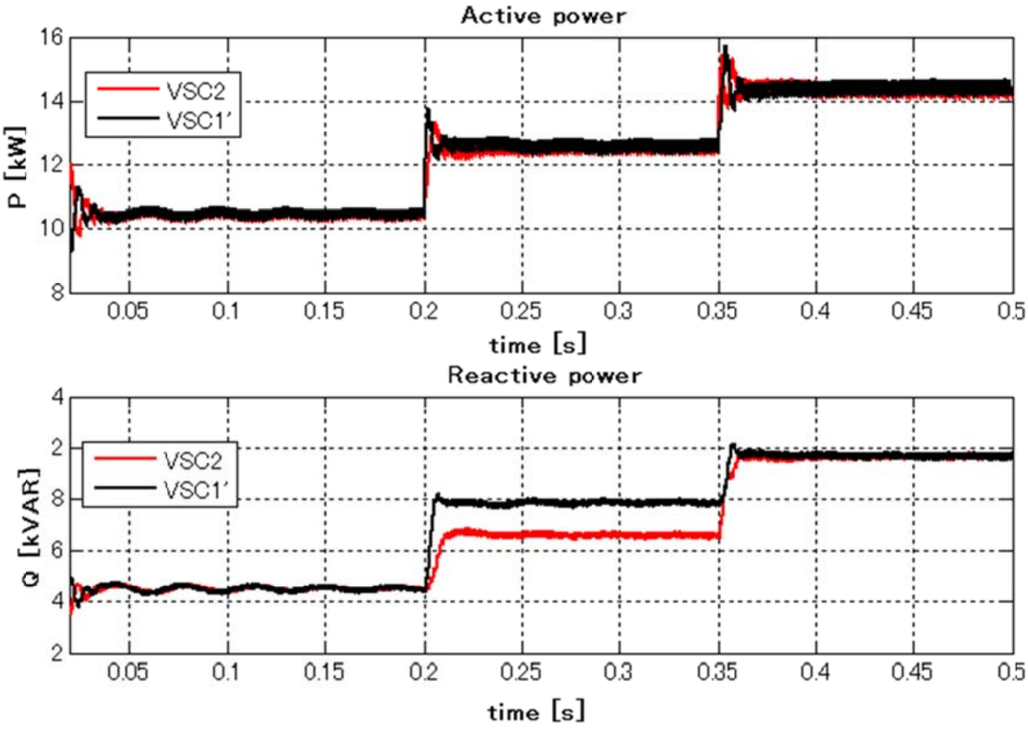

Fig. 6-9 Active and reactive power sharing.

Part of the above result may be compared with the study reported in [5], where the adaptive droop concept is proposed to decouple the mismatch of coupling impedance in power sharing without communication lines. In the cited report, the main focus was on the inductive mismatch which is compensated by the adaptive inductance applied to a single phase system. This study, however, focuses on overall impedance to be applied on three-phase system, which demonstrates a more comprehensive reactive power scheme. For example, the converter situated nearer to the load can be commanded to share more reactive load. Although the study was made for two inverter system, it can be applied to the microgrid system with any number of inverter connected to the dedicated energy storage. The scheme also works with inverter connecting the non-dispatcheble DGs, in which case reactive power can be shared as proposed above. The active power, in such case, is kept unregulated (in fact captured maximum available power as expalined in previous chapters) and the grid frequency is imposed to the system by a *phase locked loop*. Thus, we can operate both type of inverter connected systems, connected to the energy storage devices and intermittent renewable DGs, to form an autonomous distribution network.

6.6 Summary

In this chapter a modified power-sharing scheme applicable for parallel operating VSCs in a distribution microgrid has been proposed. The scheme was based on the droop regulation, which did not necessitate the communication channel among the VSCs. In contrast to conventional droop schemes, which are only applicable to line with $X>>R$, it can provide proper power sharing in distribution microgrid (where $R/X>2$ in general). Based on the fact that line parameter (R/X) negligibly affects the active power sharing and highly affects the reactive power sharing, the scheme introduces virtual impedance in the *Q-V droop* keeping the *P-f droop* unchanged. This allows the sharing of active and reactive power without sacrificing frequency/amplitude regulation in the steady-state. Another notable merit of the scheme is that it provides the flexible reactive power sharing among the VSCs so that the VSCs near the load can share more var if required.

Reference

[1] R. Lasseter and P. Paigi, "Microgrid: A conceptual solution," IEEE 35th Annual Power Electronics Specialists Conference, vol. 6, pp. 4285-4290, 2004.

[2] J. A. Peças Lopes, C. L. Moreira, and A. G. Madureira, "Defining control strategies for microgrids islanded operation," *IEEE Transactions on Power Systems*, vol. 21(2), pp. 916-924, 2006.

[3] M.N. Marwali, J. Jung and A. Keyhani, "Control of distributed generation systems-Part II: Load sharing control," *IEEE Transactions on Power Electronics*, vol. 19(6), pp. 1551-1561, 2004.

[4] A. Tuladhar, H. Jin, T. Unger and K. Mauch, "Control of parallel inverters in distributed AC power systems with consideration of line impedance effect," *IEEE Transactions on Industry Applications*, vol. 36(1), pp. 131-138, 2002.

[5] J. Guerrero, J. Matas, L. Vicuña, M. Castilla and J. Miret, "Wireless control strategy for parallel operation of distributed-generation inverters," *IEEE Transactions on Industrial Electronics*, vol. 53(5), pp. 1461-1470, 2006.

[6] A. Engler, "Applicability of droops in low voltage grids," *International Journal of Distributed Energy Resources*, vol. 1(1), pp. 3-15, Sep. 2005.

[7] C. Sao and P. Lehn, "Autonomous load sharing of voltage source converters," *IEEE Transactions on Power Delivery*, vol. 20(2), pp. 1009-1016, 2005.

[8] Mathworks-MATLAB and Simulink for technical computing (Sep. 2009), available online: http://www.mathworks.com.

[9] E. Coelho, P. Cortizo and P. Garcia, "Small-signal stability for parallel-connected inverters in stand-alone AC supply systems," *IEEE Transactions on Industry Applications*, vol. 38(2), pp. 533-542, 2002.

[10] L. Chen, X. Xiao, C. Gong and Y. Yan, "Circulating current's characteristics analysis and the control strategy of parallel system based on double close loop controlled VSI, " Proc. IEEE PESC, pp. 4791–4797, 2004.

Chapter 7 Conclusion and the Future Course

This dissertation has developed the operational and control schemes for the doubly-fed induction generator based wind turbine generation system incorporating a dedicated energy storage mix. The storage mix has consisted of a solid oxide fuel cell, an electrolyzer and an ultracapacitor, in which the fuel cell and the eletrolyzer are configured in a way to utilize minimum power electronic converters. The main focuses of the dissertation were on the control and operational aspects of the dedicated energy storage system (DESS) and the grid or line-side converter, so that all the subsystems would fit for overall power management approach.

In order to investigate the performance, the system configuration and the control scheme have been presented with the linearized models of various subsystems. Based on the dynamic component models, a simulation model for the proposed wind power and storage system (WPSS) has been developed using MATLAB/Simulink. The detailed operation strategy has been presented for coordinating the power flows among the different energy sources. Simulation studies have been carried out to verify the system performance under different operating scenarios. The results show that the overall power management strategy is effective, and the power flow among the different energy sources and the load demand is balanced successfully. The conclusions of the research work reported in this dissertation are summarized below.

Chapter two presented the layout and the unit sizing of the hybrid WPSS by investigating the candidate distributed energy resources. We identified the suitable interconnecting topology in the form of mix coupling (ac and dc coupling), so that less number of power electronic converters could be used. An important feature of integrating topology was to accommodate the fuel cell and the electrolyzer into a single dc-dc converter. Consequently, the WPSS was configured as an autonomous local power network or microgrid, which was capable to operate in the islanded and dispatchable grid-connected modes.

Chapter three investigated the prevailing dynamic models of the individual components. We explored the proper mathematical models relevant to the scope of the research. To reduce the degree of complexity and manage the computational time, few simplifications were made in the mathematical model–such as lumping of the turbine and the generator body, one dimensional treatment of the fuel cell excluding the thermal dynamic and average modeling of switching elements–without jeopardizing the accuracy of the results. Based on the numerical computation, major components were tested and compared with similar models developed by the earlier researchers.

In chapter four, the control and operational schemes of the WPSS were developed based on the mathematical models developed in chapter three. While designing the control parameters, the models are linearized around their operating points, wherever applicable. The designated control schemes for the subsystems were: regulating rotor speed to capture optimum power from wind, employing the DESS to inject two time-scale currents from the storage devices, and enabling the line-side converter to operate WPSS in different operating modes seamlessly. One of the important features of the control approach is that the three controllers (the wind turbine generator system controller, the DESS controller and the line-side converter controller) were decoupled. It means that each subsystem utilizes own terminal signals as the feedback, treating signals from the other subsystems as the disturbance inputs. This avoids the influence of mismatching and delay caused from the outside. Further, the tests of controllers against the parameters variations demonstrated their robustness in tracking the command inputs and rejecting disturbance inputs with a wide stability margin.

Chapter five presented the numerical simulation of the overall system. The simulation results depicted that the subsystems operated in accordance with the theoretical model developed in chapter four. The dedicated energy storage system demonstrated the coordinated control scheme, in which the compensating power (to balance the supply and the demand) has been shared between the fuel cell/electrolyzer and the ultracapacitor. The fuel cell/electrolyzer subunit of the DESS provides the steady-state balance and the ultracapacitor acts as a buffer for the transient power. Utilizing H_2 as the storage medium, the fuel cell and the ultracapacitor were operated to supply the designated power during the wind power deficit, whereas the electrolyzer and the ultracapacitor would came into effect during the power surplus. The crucial part of the controller design was to consider the slow dynamics of the reactants' partial pressure and the fuel regulation parts, so that the fast transients would not pass through the fuel cell/electrolyzer and cause the fuel starvation. Facilitated by functionalities of the DESS, the operational scheme of the line-side converter enabled the WPSS to operate as a dispatchable unit and a self-sustainable unit in the grid-connected and the islanded modes, respectively. In the absence of the storage system, the WPSS could also be operated in the non-dispatchable grid-connected mode similar to the conventional grid-connected wind turbine generator system. The scheme also provided seamless transition among the different modes without necessitating an additional controller for each mode.

Chapter six sought the improved power sharing schemes in the case when there are multiple inverters operated in parallel. The proposed scheme enabled to share reactive power effectively among the inverters in the distribution network having high resistance to inductance ratio.

In this study, the wind power is taken as the disturbance input, in which the disturbances are subjected to the ac and dc buses. The energy storage system and the line-side converter were jointly employed to reject the disturbance, in the form of load or intermittent power, at the dc and the ac buses. Thus, this concept is equally applicable to the other topologies, such as full-scale power electronic converter based wind turbines, fixed-speed wind turbines and the photo voltaic power based microgrid.

Based upon the above findings, the prospective research may be suggested toward the different directions. One important part of future study is in the validation of proposed schemes to the real system. The analysis in the dissertation was the theoretical one, which was tested through the numerical model. Therefore, it is necessary to confirm the obtained results experimentally so that they could be applied in the practical situations. Another direction of the future study is on the unit sizing. While designing the proposed scheme, the unit sizing was based on the technical viewpoint of fulfilling the operating requirements. To decide the proper size of the components, it is advisable to take account of several operating constraints and objective functions. So, the resulting size would be the solution of multi-objective optimization. Likewise, the main operating schemes of the proposed hybrid microgrid were focused on the primary and secondary levels control, such as the islanded mode or the dispatchable grid-connected mode. In this system, a tertiary level or supervisory control can be implemented, which takes care of the online electricity tariff, weather forecast and the state of the energy storage to employ the demand response phenomena. Such a comprehensive and autonomous local network structure can provide a substantial contribution in realizing the future “smarter” power network.

Appendix

Table A.1 Comparison of storage technologies [Barton *et al.*, “Energy storage and its use with intermittent renewable energy,” *IEEE Trans. Energy Convers.*, vol. 19(2), pp. 441–8, Jun. 2004].

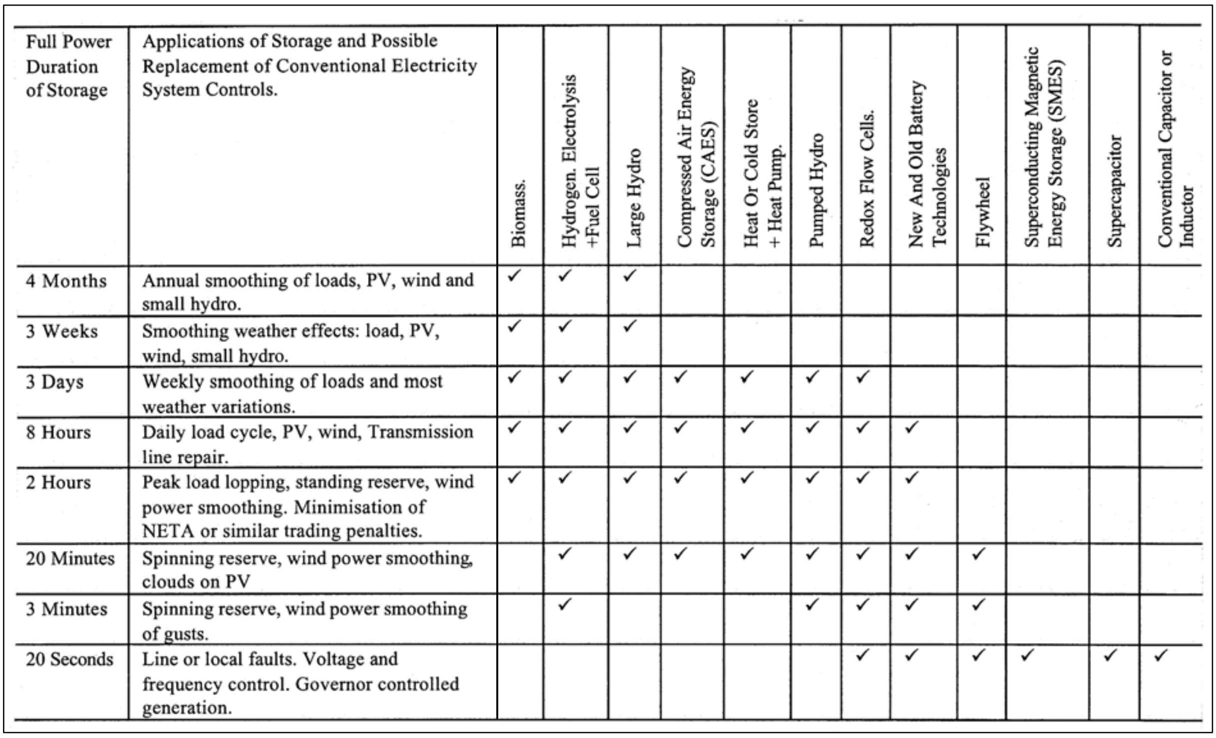

Full Power Duration of Storage	Applications of Storage and Possible Replacement of Conventional Electricity System Controls.	Biomass.	Hydrogen. Electrolysis +Fuel Cell	Large Hydro	Compressed Air Energy Storage (CAES)	Heat Or Cold Store + Heat Pump.	Pumped Hydro	Redox Flow Cells.	New And Old Battery Technologies	Flywheel	Superconducting Magnetic Energy Storage (SMES)	Supercapacitor	Conventional Capacitor or Inductor
4 Months	Annual smoothing of loads, PV, wind and small hydro.	✓	✓	✓									
3 Weeks	Smoothing weather effects: load, PV, wind, small hydro.	✓	✓	✓									
3 Days	Weekly smoothing of loads and most weather variations.	✓	✓	✓	✓	✓	✓	✓					
8 Hours	Daily load cycle, PV, wind, Transmission line repair.	✓	✓	✓	✓	✓	✓	✓	✓				
2 Hours	Peak load lopping, standing reserve, wind power smoothing. Minimisation of NETA or similar trading penalties.	✓	✓	✓	✓	✓	✓	✓	✓				
20 Minutes	Spinning reserve, wind power smoothing, clouds on PV		✓	✓	✓	✓	✓	✓	✓	✓			
3 Minutes	Spinning reserve, wind power smoothing of gusts.		✓				✓	✓	✓	✓			
20 Seconds	Line or local faults. Voltage and frequency control. Governor controlled generation.							✓	✓	✓	✓	✓	✓

The Parameters Used in the Study

Table A.2 Electrical network parameters

Parameter	value	unit
V_{dc}	750	V
V_2	460	V
ω_0	377	rad/s

Table A.3 Wind turbine parameters (Ref. [4], [5] of chapter 3)

Parameter	value	unit
P_{WT}^{rated}	40	kW
k_{opt}	0.0075	W/(rad/s)^3
$v_{w,cutin}$	4	m/s
$v_{w,cutout}$	25	m/s
ρ	1.205	kg/m^3
$C_{P\text{-}max}$	0.47	

v_w^{rated}	12	m/s
c_i (i=1,2..8)	0.73, 151, 0.58, 0.002, 2.14, 13.2, 18.4, -0.02, -0.003	
r_T	15	m

Table A.4 Induction generator parameters

Parameter	value	unit
Rated Power (S^{rated})	50	kVA
Rated line voltage (V_s)	460	V
L_{ls}	0.057	pu
r_s	0.0175	pu
L_{lr}	0.057	pu
r_r	0.01029	pu
L_m	2.019	pu
J_m	0.2	pu
D_m	0.05	pu
n_p	2	

Table A.5 Parameters for Phoebus alkaline electrolyzer (Ref. [22] of chapter 3)

Parameter	value	unit
A_{elz}	0.1	m^2
f_1	250	
f_2	0.96	
N_{elz}	270	
P_{elz}^{rated}	50	kW
r_1	8.05×10^{-5}	Ωm^2
r_2	2.5×10^{-7}	Ωm^2 °C
u_0	1.21	Volt
u_1	0.185	V
T_{elz}	80	°C
t_1	-1.002	$A^{-1}m^2$
t_2	8.424	$A^{-1}m^2$ °C
t_3	247.3	$A^{-1}m^2$ $°C^2$
z	2	

Table A.6 Parameters for SOFC (Ref. [18] of chapter 3)

Parameter	value	unit
A_{elecyt}	200×10^{-4}	m^2
A_{interc}	45×10^{-4}	m^2
$E_{0,cell}$	1.18	V
F	96484.6	C/mol
I_{limit}	160	A
N_{cell}	95	
P_a	3	atm
P_c	3	atm
P_{fc}^{rated}	5	kW
R	8.314	J $mol^{-1}K^{-1}$

μ_f	0.85	
T_{fc}	1173	K
V_a	61.7×10^{-6}	m^3
V_c	99.02×10^{-6}	m^3
k_E	3.78×10^{-4}	
z	2	
κ_0	0.15	V
a_c	53.5041	
b_c	65000	
α_{elecyt}	4.0866×10^{-4}	
β_{elecyt}	6900	
δ_{elecyt}	40×10^{-6}	
α_{interc}	0.0175	
β_{interc}	3126.7	
δ_{interc}	40×10^{-6}	

Table A.7 Parameters for the ultracapacitor (Ref. [28] of chapter 3)

Parameter	value	unit
C	110	F
$I_{leakage}$	1.5	mA
I_{max}	30	A
R_{sr}	5.5	mΩ
V_{max}	16.2	V
UC stack		
C_{uc}	32	F
N_{sr}	17	
N_{pl}	5	
P^{rated}	40	kW

Table A.8 Parameters for WTGS controller

Parameter	value	unit
ψ_s^{rated}	1.5	Weber
$G_{C1}(s)$	$0.1582+9.102/s$	
α_{1c}	0.01	
α_{2c}	0.7	
γ_{2c}	1.35	
$G_{C2}(s)$	$1.3786+1.0204/s$	
$T_{i,pit}$	0.5	s
$T_{d,pit}$	0.8	s

Table A.9 Parameters for the fuel cell side dc-dc converter (DC1) controller

Parameter	value	unit
V_{fc}^{ref}	275	V
D_2, D_3	0.6	

I_{dc1}^{rated}	100	A
L_i	1	mF
R_i	0.1	mΩ
T_d	5	s
$G_{C3}(s)$	$0.00256+0.00535/s$	
$G_{C4}(s)$	$10+0.0084/s+0.036s/(s+0.36)$	
V_{uc}^{ref}	250	V

Table A.10 Parameters for isolating DC2 controller

Parameter	value	unit
V_{dc}^{ref}	750	V
$G_{C5}(s)$	$1.98745+14.037/s$	
L_t	0.1	mH
f_{sw}	2	kHz
C_{dc}	5	mF

Table A.11 Parameters for line-side converter controller

Parameter	value	unit
V_0	460	V
L_f	0.2	mH
L'	0.248	mH
R_f	0.0063	Ω
R'	0.01	Ω
$G_{C6}(s)$	$0.08+2.5264/s$	
$G_{C7}(s)$	$40/s(0.0025s+1)/(0.248s+0.01)$	
k_{qt}	0.1	
k_{ω}	0.5	
k_{dc}	0.11	
m	20	
$G_{C8}(s)$	$0.1+1.23/s$	
$G_{C9}(s)$	$0.1+1.23/s$	

Table A.12 Parameters for multiple voltage source converter system controller

Parameter	value	unit
k_{11}	10^{-5}	
k_{12}	10^{-5}	
m_1	$\pi/20\times10^{-3}$	
m_2	$\pi/30\times10^{-3}$	
n_1	0.2×10^{-3}	
n_2	0.3×10^{-3}	
z_{01}	0.02	Ω
z_{02}	0.02	Ω

List of Symbols

Wind data

A_g	Amplitude of the wind speed gust
A_{rm}	Amplitude of the wind speed ramp
A_w	Rotor sweep area by wind
c	Scale parameter for wind speed
f_w	Frequency of wind speed
h	Tower height
k	Shape parameter for wind speed
l	Turbulence length
P_{Dt}	Power spectral density of wind speed
P_{wind}	Power from wind
T_{eg}	End time of wind speed gust
T_{er}	End time of wind speed ramp
T_{sg}	Starting time of wind speed gust
T_{sr}	Starting time of wind speed ramp
v_w	Wind speed
v_{wa}	Average wind speed
v_{wg}	Gust component of wind speed
v_{wm}	Wind speed corresponding to maximum energy capture
v_{wr}	Ramp component of wind speed
v_{wt}	Turbulence component of wind speed
W_{max}	Maximum energy produced at v_{wm}
ε	Roughness length
ρ	Density of air

Wind turbine

c_i	Parameters for the wind turbine (i=1,2..8)
C_P	Wind power conversion coefficient
$C_{P\text{-}max}$	Maximum value of C_P
P_{WT}	Mechanical power at the turbine shaft
r_T	Rotor radius
T_m	Mechanical torque at the turbine shaft
β	Pitch angle
λ_{tip}	Tip speed ratio
λ_{tip}^{opt}	Optimum tip speed ratio
ω_r	Rotor speed

ω_r^{opt}	Optimum rotor speed

Doubly-fed induction generator system (IG, VSC1, VSC2 and dc-link bus)

C_{dc}	Capacitance of the dc-link terminal
D_m	Equivalent frictional coefficient
$\mathbf{d}_1$	Duty cycle space vector of rotor-side converter (VSC1)
$\mathbf{d}_2$	Duty cycle space vector of line-side converter (VSC2)
E_2	Terminal rms voltage of line-side converter (VSC2)
$\mathbf{e}_2$	Terminal voltage space vector of line-side converter (VSC2)
I_2	rms current of bus #2
$\mathbf{i}_2$	Current space vector of bus #2
$\mathbf{i}_{\mathrm{mo}}$	Magnetizing current state vector
$\mathbf{i}_{\mathrm{r}}$	Rotor current space vector
$\mathbf{i}_{\mathrm{s}}$	Stator current space vector
$I_{2,dc}$	Net dc current drawn from the line-side converter
$I_{r,dc}$	Net dc current injected from the rotor-side converter
I_{sto}	Net dc current injected from the storage system
J_m	Equivalent moment of inertia
L_f	Inductance of coupling inductor
L_{ls}	Stator leakage inductance
L_{lr}	Rotor leakage inductance
L_m	Mutual inductance
L_r	Rotor self-inductance
L_s	Stator self-inductance
L_{th}	Thevenin inductance
n_p	Number of pole pair
P_{ig}	Net active power from the doubly-fed induction generator
P_r	Active power drawn from the rotor circuit of the doubly-fed induction generator
P_s	Active power drawn from the stator circuit of the doubly-fed induction generator
Q_{ig}	Net reactive power from the doubly-fed induction generator
Q_s	Reactive power from drawn from the stator terminal
R_{dc}	Parallel resistance of the dc-link capacitor
R_f	Resistance of the coupling resistor
R_{th}	Thevenin resistance
r_r	Rotor resistance
r_s	Stator resistance
s_l	Slip of induction generator
T_{em}	Electromagnetic torque
T_m	Mechanical torque at the shaft
V_2	Voltage of bus #2 in rms
V_{dc}	dc-link voltage

$\mathbf{v}_1$	Voltage space vector of bus #1
$\mathbf{v}_2$	Voltage space vector of bus #2
$\mathbf{v}_r$	Rotor voltage space vector
$\mathbf{v}_s$	Stator voltage space vector
$\boldsymbol{\psi}_s$	Stator flux space vector
$\boldsymbol{\psi}_r$	Rotor flux space vector
ω_e	Angular frequency of stator voltage

Fuel cell

a_c, b_c	Empirical parameters for activation voltage drop
C_{fc}	Double layer capacitance
E_{cell}	Nernst voltage
$E_{0,cell}$	Gibbs potential
F	Faraday constant
i_0	Exchange current density
I_{fc}	Fuel cell current
I_{limit}	Limiting current density
k_E	Emprical constant
M_a	Molar value at anode
M_c	Molar value at cathode
M_x	Molar flow of species x (x = H_2, O_2 or H_2O)
N_{cell}	Number of cell in the stack
P_{fc}	Power from the SOFC
p_x	Partial pressure of species x (x = H_2, O_2 or H_2O)
R	Universal gas constant
$R_{ohm,cell}$	equivalent resistances representing ohmic voltage drop
$R_{act,cell}$	equivalent resistances representing activation voltage drop
$R_{conc,cell}$	equivalent resistances representing concentration voltage drop
r_{H_2O}	hydrogen-oxygen flow ratio
T_d	Time constant for fuel regulation
T_{fc}	Fuel cell temperature
U_a, U_c	Volume of anode and cathode part
μ_f	Fuel utilization ratio
$V_{act0,cell}$	Activation voltage drop affected by the temperature
$V_{act1,cell}$	Activation voltage drop affected by the temperature and current
$V_{act,cell}$	Fuel cell activation potential
$V_{con,cell}$	Fuel cell concentration potential
V_{fc}	Fuel cell terminal voltage
$V_{ohm,cell}$	Ohmic potential drop

α_i, b_i, δ_i	Parameters for resistive voltage drop in the electrolyte of the solid oxide fuel cell (i=electrolyte, interconnection)
z	Number of electron participating in the chemical reaction
κ_0	Constant term of activation voltage drop
κ_1	Temperature coefficient the activation voltage drop

Electrolyzer and hydrogen production

A_{elz}	Electrodes' surface area
I_{elz}	Electrolyzer current
J_{elz}	Electrolyzer current density
$M_{H2,out}$	Hydrogen outflow rate
$M_{H2,pro}$	Hydrogen production rate
N_{elz}	Number of cell in a stack
$p_{elz,H2}$	Hydrogen pressure of at cathode
r_i	Parameters of ohmic resistance (i=1,2)
T_{elz}	Temperature of the electrolyzer
t_i	Parameter of overvoltage (i=1,2,3)
u_0	Thermodynamic cell voltage
u_1	Parameter of overvoltage
u_{cell}	Terminal voltage across one electrolyzer
V_{elz}	Net terminal voltage across the electrolyzer stack
U_{elz}	Volume of the cathode

Compressor and H_2 storage

P_{comp}	Compressor power
p_{elz,H_2}	Hydrogen pressure of at cathode
p_{tank}	Pressure of storage tank
T_{tank}	Temperature of storage tank
U_{tank}	Volume of storage tank
w	Polytropic work
α_{com}	Compression efficiency
ν	Polytropic coefficient

Ultracapacitor and dc-dc converters

C_{uc}	Capacitance of the ultracapacitor
d_i	Duty cycle for i^{th} switch in the converter fuel cell side dc-dc converter (i=1,2,3)
E_{uc}	Energy available from the ultracapacitor
f_{sw}	Switching frequency of isolating dc-dc converter (DC2)

I_{dc1}	Output current from the fuel cell side dc-dc converter (DC1)
I_{dstb}	Net disturbance current imposed to the dedicated energy storage system
I_i	Input current injected to the isolating dc-dc converter (DC2)
I_{sto}	Net current injected from the dedicated energy storage system (DESS)
L_i	Output inductance of the fuel cell side dc-dc converter (DC1)
L_t	Inductance of isolating transformer
R_i	Output resistance of the fuel cell side dc-dc converter
R_{sr}	Equivalent series resistance of the ultracapacitor
R_{pl}	Equivalent parallel resistance of the ultracapacitor
V_f	Final voltage for the ultracapacitor
V_i	Initial voltage for the ultracapacitor
V_{uc}	Voltage across the ultracapacitor terminal
δ	Phase shift in the isolating dc-dc converter (DC2)

Control and operational scheme

$C(s)$	Transfer function of internal model controller
d	Disturbance signal
$G(s)$	Plant transfer function
$G_{Ci}(s)$	Transfer function of ith PID controller, (i=1,2..9)
$G_{CP}(s)$	Transfer function of pitch control
$G_d(s)$	Disturbance transfer function
$F(s)$	Transfer function equivalent proportional-integral-derivative controller
I_{dstb}	Total disturbance current to the dedicated energy storage system
k_{iP}, k_{iI}	Coefficient of proportional and integral control of converter $G_{Ci}(s)$ (i=1,2..8)
k_{dc}	Parameter for dc voltage control
k_M	Parameter for the first order plant
k_{pwmi}	Pulse width modulation gain
k_{tie}	Parameter for tie-line active power control
k_{qt}	Parameter for tie-line reactive power control
$L(s)$	Filter transfer function
m	Droop coefficient
n	Integer quantity
P_2	Active power flow through the line-side voltage source converter (VSC2)
P_{tie}	Tie-line active power flow
Q_{tie}	Tie-line reactive power flow
r	Command input signal
ss	Status signal
T_g	Coefficient of grid power transfer
u	Manipulating variable
y	Output signal
α	Filter parameter for the internal model control
α_{1c}	Parameters of internal model control for $G_{C1}(s)$
α_{2c}	Parameter of the internal model control for $G_{C2}(s)$

α_{6c}	Parameter of the internal model control for $G_{C6}(s)$
θ_f	Angle of rotating stator flux
τ_p	Time constant of the first order plant
τ_{tg}	Time constant of turbine generator lump system
τ_{pit}	Time constant of pitch angle control loop
γ	Parameter for the improved internal model control
γ_{2c}	Parameter of the internal model control for $G_{C2}(s)$
ω_r^{opt}	Optimum rotor angular velocity
ω_0	Nominal value of ac angular frequency
ω_s	Slip speed

Microgrid with multiple VSCs

δ_i	Phase difference of phase between the i^{th} inverter terminal and i^{th} PCC voltage
e_i	Difference of magnitudes between i^{th} inverter terminal and i^{th} PCC voltage
E_i	Voltage of i^{th} inverter terminal
I_i	rms value of the current injected from the i^{th} inverter
m_i	*P/f* droop of i^{th} inverter
n_i	*Q/V* droop of i^{th} inverter
P_i	Active power flow from i^{th} inverter terminal
Q_i	Reactive power flow from i^{th} inverter terminal
$Q_{max,i}$	Maximum reactive power supplied by the ith inverter.
S_i	Apparent power flow from i^{th} inverter terminal
V_i	Voltage of ith PCC bus
Z_{Ei}	Virtual output impedance of i^{th} inverter
Z_i	Impedance of i^{th} coupling inductor

Subscripts

r	Quantity related to the rotor circuit of the doubly-fed induction generator
s	Quantity related to the stator circuit of the doubly-fed induction generator
d	*d* axis quantity of the doubly-fed induction generator
q	*q* axis quantity of the doubly-fed induction generator
dc	Quantities related to the dc-link bus
elz	Quantities related to the electrolyzer
fc	Quantities related to solid oxide fuel cell
uc	Quantities related to ultracapacitor

Superscripts

opt	Optimum value of the quantity
ref	Reference value of the quantity
rated	Rated value of the quantity
in	Inflow rate of the quantity
out	Out flow rate of the quantity

List of Acronyms

AE	Alkaline electrolyzer
DESS	Dedicated energy storage system
DFIG	Double fed induction generator
DER	Distributed energy resource
DG	Distributed generators
ELZ	Electrolyzer
ESS	Energy storage system
DC1	Electrolyzer and fuel cell and side dc-dc converter
DC2	dc-link bus side isolating dc-dc converter
DESS	Dedicated energy storage system
FC	Fuel cell
FES	Flywheel energy storage system
IG	Induction generator
IMC	Internal model controller
LVRT	Low voltage ride through
LPN	Local power network
LV	Low voltage
MIMO	Multiple input multiple output
MPPT	Maximum power point tracking
MV	Medium voltage
PCC	Point of common coupling
PE	Power electronics
PEC	Power electronic converter
PI	Proportional-integral control
PID	Proportional-integral-derivative control
PV	Photo voltaic
PWM	Pulse width modulation
SISO	Single input single output
SMES	Superconducting magnetic energy storage
SOFC	Solid oxide fuel cell
TSR	Tip speed ratio
UC	Ultracapacitor
VSC	Voltage source converter
VSC1	Rotor-side converter
VSC2	Line-side converter

WPSS	Wind power and storage system
WT	Wind turbine
WTGS	Wind turbine generator system